F C Ciências
ULisboa

Detection and limits of detection of minor chemical species in Solar System's atmospheres

João André Baêta Dias

Mestrado em Física
Especialização em Cosmologia e Astrofísica

Dissertação orientada por:
Dr.Pedro Mota Machado

2021

Resumo

O estudo de espécies químicas minoritárias em atmosferas do tipo terrestre fornece informação sobre a química, a dinâmica e a evolução das atmosferas com o tempo (Encrenaz [15]).

O dióxido de enxofre (SO_2) e a água (H_2O) contribuem para a formação da espessa camada de nuvens de ácido sulfúrico que cobre o planeta Vénus. Presentemente, não se sabe ainda qual é a fonte de abastecimento de dióxido de enxofre existente na atmosfera. Sabemos que a sua abundância varia no espaço e no tempo com um fator que varia entre 5 e 10 (Encrenaz et al. [17]). Desta forma, é importante medir o perfil de composição vertical desta espécie e sua variabilidade na atmosfera (Vandaele et al. [68]).

A fosfina (PH_3) e o metano (CH_4) são espécies minoritárias que são potenciais bioassinaturas, quer isto dizer que a deteção destas espécies pode identificar a existência de vida no presente ou no passado num planeta. Em detalhe, as espécies mencionadas são exemplos de bioassinaturas gasosas, isto é, espécies que são um produto direto ou indireto do metabolismo de organismos (Schwieterman et al. [59], Sousa-Silva et al. [61]). Na Terra, sabemos que a fosfina apenas é produzida por processos biológicos ou por processos antropogénicos, embora em Júpiter e Saturno já se tenha detetado fosfina. Contudo, a fosfina nos gigantes gasosos forma-se naturalmente em condições de alta temperatura e pressão (T $\sim$ 1000 K, P $\sim$ 1kbar) (Irwin [32]), que não se encontram em Vénus. Torna-se, portanto, fundamental procurar e estudar estas espécies em corpos do Sistemas Solar como forma de preparação para a sua procura nas atmosferas dos exoplanetas.

Greaves et al. [29] reportou a deteção da presença de fosfina na atmosfera de Vénus, em particular no topo das nuvens, estimando uma abundância de cerca de 20 ppb, através de observações no submilímetro da transição dos 1.123 mm, com o radio-observatório ALMA (Atacama Large Milimeter Array) e o telescópio JCMT (James Clerk Maxwell Telescope). Encrenaz et al. [20] constringiu um limite superior para a abundância de fosfina em Vénus de 5 ppb, através de observações no IR do instrumento TEXES (Texas Echelon Cross Echelle Spectrograph), por volta dos 951-956 cm^{-1}. A abundância de fosfina proposta por ambos estes estudos é muito elevada comparada com aquela estimada por modelos atuais, que consideram reações foto-químicas e de estado-estacionário na atmosfera, superfície, nuvens e sub-superfície. Fontes a partir de volcanismo, relâmpagos e meteoritos foram descartadas. A abundância estimada por modelos é quatro ordens de grandeza inferior àquela proposta pelas observações acima. Desta forma, uma futura confirmação da deteção de fosfina em Vénus pode ser indicativo de processos geoquímicos desconhecidos em atuação ou de uma presença biológica em Venus (Greaves et al. [29]).

Giuranna et al. [26] reportou a história confirmação independente da deteção de metano em Marte, através de observações por volta dos 3018 cm^{-1} (3.31 μm), correspondente a uma abundância estimada de 15.5 ppb, usando o instrumento PFS (Planetary Fourier Spectrometer) a bordo da missão Mars Express (MEx). O local onde a deteção foi feita foi na região da cratera Gale, contudo ainda não se conhece qual o processo físico de produção do metano e qual a sua origem. Tanto uma reação geoquímica como origem biológica são possibilidades a considerar com atenção (Giuranna et al. [26]). Os instrumentos NOMAD SO (Nadir and Occultation for Mars Discovery) e ACS (Atmospheric Chemistry Suite) na missão ExoMars procuraram detetar linhas de absorção de metano cobrindo um vasto intervalo de latitudes e longitudes, por volta dos 3029 cm^{-1} (3.30 μm) e dos 3049 cm^{-1} (3.28 μm). Contudo a procura teve um resultado negativo.

De modo a desvendar a origem e evolução das atmosferas planetárias é feito o estudo dos rácios isotópicos nas atmosferas planetárias, isto é, o rácio de abundâncias entre isópotos leves e pesados de um mesmo elemento. Em particular, o rácio da abundância do deutério para a abundância da água, o D/H, e o estudo da sua variabilidade temporal e espacial é importante para estudar a perda de atmosfera com

o tempo e a evolução da abundância de água nas atmosferas de planetas do tipo telúrico (de Bergh [6], Encrenaz et al. [19]). Vénus tem um D/H $\sim$ 157-240 D/H (Terra) (Fedorova et al. [21]), mais elevado comparando com o mesmo rácio para a Terra e para Marte. Duas razões possíveis avançadas para explicar esta diferença são o fluxo no UV superior que chega ao topo da atmosfera de Vénus em comparação com aquele que chega ao topo da atmosfera da Terra e a elevada temperatura que se encontra na superfície de Vénus. Estes dois fatores contribuem para a perda de átomos de hidrogénio na alta atmosfera em maior quantidade do que os de deutério, devido à massa inferior do primeiro em comparação com a do segundo, resultando num aumento geral do D/H (Donahue and Hodges [11]).

Usando o PSG (Planetary Spectrum Generator) (Villanueva et al. [69]), uma ferramenta de transferência radiativa disponível online, comparei simulações de espetros planetários com observações, com o objetivo de identificar e constringir a abundância de espécies químicas minoritárias nas atmosferas de Vénus, Marte e Júpiter.

Em Vénus, foi feita a deteção de linhas de absorção de dióxido de enxofre e a sua abundância foi estimada em cerca de 120 ppb, através da comparação das simulações com observações no IR do espectrógrafo TEXES no IRTF (Infrared Telescope Facility), por volta dos 7.4 μm (Encrenaz et al. [17]). Este valor é semelhante àquele obtido por Encrenaz et al. [19], cerca de 50-100 ppb. A fosfina não foi detetada na comparação das simulações com observações do TEXES (Encrenaz et al. [20]), por volta dos 10.5 μm, resultado este idêntico ao de Encrenaz et al. [16]. Esta não-deteção está associada à presença de uma banda telúrica de absorção de água, presente na mesma zona do espetro onde seria de esperar vermos uma linha de absorção de fosfina, por volta dos 955.26 cm^{-1}. Esta não-deteção não implica que não existe fosfina em Vénus, mas implica que de modo a confirmarmos a sua presença em Vénus mais observações dedicadas terão de ser feitas, em especial no IR onde a fosfina tem várias bandas de absorção.

Em Marte, reproduzi com sucesso a deteção positiva e a deteção negativa do metano efetuadas pelo instrumento PFS da MEx (Giuranna et al. [26]) e pelo instrumento NOMAD SO da ExoMars (Webster et al. [72]), respetivamente, feitas por volta dos 3.3 μm. Estes dois resultados parecem contraditórios, contudo há que considerar a existência de uma possível variabilidade temporal e espacial da abundância do metano na atmosfera de Marte, possivelmente resultante da dinâmica e química dessa mesma atmosfera, que está a ser estudada neste momento.

Em Júpiter, reanalisei observações do ISO (Infrared Space Observatory) (Encrenaz et al. [16]), por volta dos 7-12 μm, comparando com simulações. Detetei a presença de uma banda de emissão de metano e de bandas de absorção de metano deuterado (CH_3D), da fosfina e do amoníaco (NH_3). Fiz uma primeira estimativa da abundância destas espécies minoritárias na atmosfera de Júpiter. As abundâncias estimadas para o metano e o metano deuterado foram, respetivamente, $(2.8-3.0) \times 10^{-3}$ e $1.23-1.37 \times 10^{-7}$.

Por fim, uma determinação do D/H em Vénus, Marte e Júpiter foi obtida, através de uma comparação entre simulações e observações no IR feitas pelo CHFT (Canada-Hawai-France Telescope) (de Bergh et al. [7]), pelo observatório SOFIA (Stratospheric Observatory for Infrared Astronomy) (Encrenaz et al. [18]) e pelo observatório ISO (Encrenaz et al. [16], Lellouch et al. [40]), respetivamente.

Em Marte, o valor obtido foi D/H $\sim$ 5.9 D/H (Terra), e é semelhante ao valor obtido por Encrenaz et al. [18], D/H $\sim$ 3.4-4.8 D/H (Terra). Em Vénus e Júpiter, as estimativas obtidas foram D/H $\sim$ 107 D/H (Terra) e D/H (H_2) $\sim$ $(1.8-2.4) \times 10^{-5}$, respetivamente. Estes valores são compatíveis com D/H = 80-160 D/H (Terra), obtido por de Bergh et al. [7], e com D/H (H_2) = $(1.9-2.6) \times 10^{-5}$, obtido por Lellouch et al. [40], respetivamente.

Em suma, o PSG provou ser uma ferramenta eficaz para a procura de espécies químicas minoritárias em vários planetas do Sistema Solar, bem como espécies com interesse astrobiológico como o metano e a fosfina.

Abstract

The study of minor chemical species in terrestrial planets atmospheres can teach us about the chemistry, dynamics and evolution of the atmospheres through time (Encrenaz [15]).

The detection of phosphine or methane in terrestrial planets is a potential biosignature, such that it can pinpoint the presence of life on a planet, if detected in chemical disequilibrium amounts (Schwieterman et al. [59], Sousa-Silva et al. [61]). Therefore, the search for these elements on the Solar System is an important step to later apply the same techniques to exoplanetary atmospheres.

To study atmospheric depletion and the evolution of water abundance on the atmospheres of terrestrial planets, the estimation of the D/H ratio and its spatial and temporal variability is used (de Bergh [6],Encrenaz et al. [20]).

This thesis reports on the use of a tool called the Planetary Spectrum Generator (PSG) (Villanueva et al. [69]), a radiative transfer suite, with the goal of simulating observations of Venus, Mars and Jupiter searching for minor chemical species.

For Venus, sulphur dioxide absorption lines were detected and its abundance constrained, by comparing simulations with observations by the Texas Echelon Cross Echelle Spectrograph (TEXES), around 7.4 μm (Encrenaz et al. [17]). Phosphine was not detected in the comparison between simulation and TEXES IR observations, around 10.5 μm (Encrenaz et al. [19]). For Mars, both a positive and a negative detection of methane were reproduced, by simulating IR observations by, respectively, the Mars Express (MEx) (Giuranna et al. [26]) and ExoMars missions (Webster et al. [72]), around 3.3 μm.

For Jupiter, the detection of ammonia, phosphine, deuterated methane and methane was done as well as a first constraint on the abundance of these species, by comparing simulations with IR observations by the Infrared Space Observatory (ISO), around 7-12 μm (Encrenaz et al. [16]).

On Venus and Mars, an estimate of the deuterium to hydrogen ratio (D/H) was obtained, by comparing simulations with observations by the Canada-Hawai-France Telescope (CFHT) (de Bergh et al. [7]), around 2.34-2.43 μm, and by the Echelon Cross Echelle Spectrograph (EXES) (Encrenaz et al. [18]), around 7.19-7.23 μm, respectively.

Keywords Venus, Mars, Jupiter, Planetary Spectrum Generator, sulphur dioxide, phosphine, methane, high-resolution spectroscopy, minor chemical species, D/H ratio, astrobiology

Acknowledgments

Last but not the least, I want to thank my supervisor, Dr. Pedro Machado, for constantly reminding of the beauty of Planetary Sciences, for believing in my work and for opening so many doors for me in the future. I learned what it means to be a scientist and the importance of collaboration within and between research groups.

Contents

List of Tables

List of Figures

Chapter 1

Introduction

1.1 Venus

Venus is know by some as the evil-twin of Earth, since although its has a similar mass and density, it is very different from Earth. The mass of Venus is about 80 % of Earth´s mass and its mean density is about 5.3 g/cm^3, compared with 5.5 g/cm^3 for Earth. Its atmosphere is mainly composed of carbon dioxide (96.5 %) and nitrogen (3.5 %), with small amounts of H_2O, SO_2, CO and other minor species (see Table 1.1). Due to an extreme greenhouse effect, its mean surface temperature rounds 740 K (3 times the calculated sub-stellar equilibrium temperature), outstanding a pressure of near 92 bars. Venus is closer to the Sun that Earth, about 30 % closer to the sun in average. The closer distance to the Sun may explain the large differences between the atmospheres of Earth and Venus.

Venus rotates counterclockwise, unlike Earth and Mars, the other terrestrial planets. The atmosphere is observed to be in superrotation, meaning it rotates much faster than the solid globe, taking about 4.4 days to rotate while the globe takes 243 days. The physical mechanism that generates this effect is still not well understood. Its atmospheric dynamics are driven by solar thermal heating and its very low rotation rate. Venus has fast horizontal winds parallel to the equator, reaching about 100 ms^{-1}. The meridional winds are slower.

The atmosphere is very heavy (about twice the mass of Earth's) and covers the planet completely with a thick layer of sulphuric acid clouds mixed with aerosols of unknown composition, between 48 km and 70 km of altitude. About 75 % of the solar light that reaches Venus is reflected back by these clouds. The cloud coverage on Venus can reach about 100 % while on Earth in average is 40 %. The clouds on Venus are important for the calculation of the albedo, the thermal structure and atmospheric balance.

Different layers of the atmosphere are sounded according to different wavelengths of observation, and demonstrate that Venus has a very rich and dynamic atmosphere (see Fig. 1.1). The upper atmosphere, above the cloud tops, is sounded in the visible and in the ultraviolet, for example. IR wavelengths sound the middle and lower atmosphere of Venus.
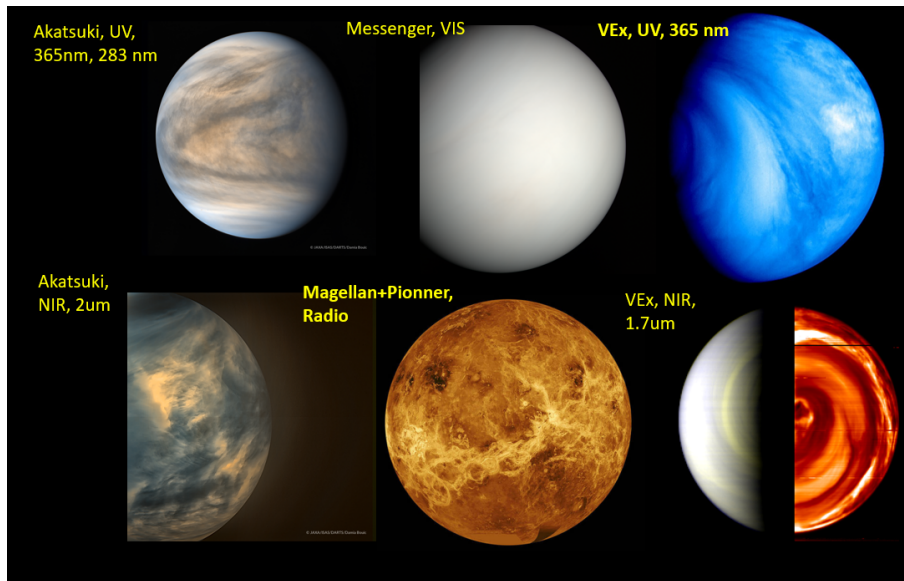
Figure 1.1: Venus observed at different wavelengths. **Top row:** From left to right: Akatsuki, UV, 365 nm, 283 nm; Messenger, Visible; Venus Express (VEx), UV, 365 nm; **Bottom row:** From left to right: Akatsuki, NIR, 2 μm; Magellan+Pioneer, Radio; VEx, NIR, 1.7 μm. Different layers of the atmosphere are sounded according to different wavelengths of observation. The upper atmosphere, above the cloud tops, is sounded in the visible and in the ultraviolet, for example. IR wavelengths sound the middle and lower atmosphere of Venus.

1.1.1 Atmosphere Composition

It is thought that initially the atmospheres of Venus and Earth had the same amount of carbon dioxide. However, on Earth most have been buried on the crust or dissolved in the oceans. On Venus, most of it is still present in the atmosphere (Machado [42]).

Reactions between H_2O and SO_3 (product of oxidation of SO_2) produce H_2SO_4 at around 62-68 km altitude (about 160 mbar). The sulphur dioxide is important in the surface/atmosphere coupling. SO_2 is consumed in the reactive process of sulphuric acid formation. The abundance of SO_2 in the lower atmosphere is much higher than the value predicted by surface-atmosphere balance (180 ppm compared with 20 ppm at cloud top). CO_2 and H_2O are photolysed in the upper atmosphere. The photolysis of CO_2 leads to the formation of CO. A replenishment source for CO_2, H_2O and SO_2 must exist. The obvious candidate is volcanism, but further evidence is necessary to confirm this. OCS is another trace gas and plays a role in the sulphur cycle (see Fig.1.5), having a molar mixing ratio of about one third of that of SO_2. Hydrogen sulfide (H_2S) is found in trace amounts, in the order of a few ppm.

The study of atmospheric trace species in the lower atmosphere has been done both by ground-based observations and space-based, in the NIR night-side spectral "windows", around 2.3-2.47 μm and 1.73-1.76 μm. The ground-based observations have done studies of the composition of the troposphere, regarding species such as CO, CO_2, OCS, H_2O, HDO, HCl and HF (Bézard et al. [5], de Bergh et al. [7], de Bergh et al. [8], Pollack et al. [55]; CO, OCS: Marcq et al. [43], Marcq et al. [44]. For the mesosphere, study of HDO, OCS, SO_2 have been done (Krasnopolsky [36], Krasnopolsky [37], Encrenaz et al. [17]). Space-based observations, by the Venus Express mission were also proficuous in studying the tropospheric composition for species such as CO, OCS, H_2O and SO_2. For the mesosphere, several studies regarding CO, H_2O, HDO and SO_2 have been made (see review by Titov et al. [66] and Fig. 1.2). More recently, an ozone layer was detected by Montmessin et al. [47], based on SPICAV solar occultation measurements.
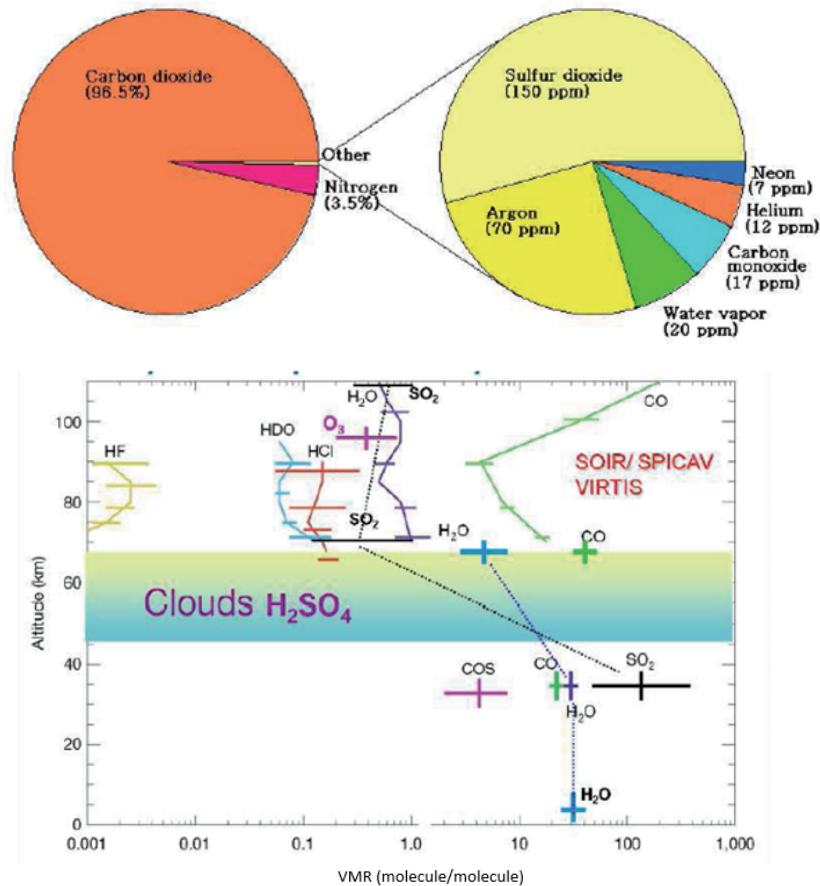
Figure 1.2: Composition of Venus's atmosphere. **Top:** Relative composition of Venus's atmosphere (figure: NASA website). **Bottom:** Vertical composition profiles of the minor species in Venus's atmosphere resulting from studies of the Venus Express mission, in the UV and IR. Volume mixing ratio (molecule/molecule) (x-axis) as a function of altitude (km) (y-axis) (credits: ESA'S Venus Express mission)

1.1.2 The Quest for Phosphine on Venus - Observations by TEXES

The search for life elsewhere in the Universe studies the possibility of detecting biosignatures in exoplanets's atmospheres as a way to identify the presence of life. These are molecules which can be produced by life. For example, phosphine, methane and oxygen are produced by organisms on Earth and perhaps they are also produced by living organisms in other exoplanets similar to Earth.

It was proposed that phosphine detected in a rocky-exoplanet atmosphere is a potential sign of life (Sousa-Silva et al. [61]). On Earth, PH_3 has a global abundance at the level of ppt, although it can reach levels of ppb or ppm in certain regions of the globe. Its origin on Earth is associated with anthropogenic activity or microbial presence. However, phosphine can also be produced in the reducing atmospheres of Jupiter and Saturn, in the deep atmosphere where temperature and pressure are high enough, with T $\sim$ 1000 K and p $\sim$ 1kbar (Irwin [32]).

The search for phosphine both on Venus, and its study on Jupiter and Saturn, is an important step to latter apply the same techniques for terrestrial exoplanets.

Greaves et al. [29] reported the presence of phosphine on Venus's atmosphere, through the detection of a phosphine rotational transition at 1.123 mm, using both ALMA and JCMT observations in the sub-millimeter (See Fig. 1.3). They inferred an upper limit of 20 ppb for the abundance of phosphine on the atmosphere of Venus. They studied, in detail, photochemical pathways and steady-state chemistry production routes in the atmosphere, surface, clouds and subsurface. Lightning, volcanic processes and

meteoritic origin were discarded as possible sources of phosphine at the proposed detection abundance. The photochemical pathways produce phosphine in an abundance four orders of magnitude smaller than the abundance detected in the observations. This suggests unknown photochemistry or geochemistry, or even a biological origin. Nevertheless, it is important to notice that microorganisms on Earth can live in environments with up to 5 % of acid, such that the existence of microorganisms in the cloud top of Venus, which has up to 90 % of acid, is practically excluded (Seager et al. [60]).

Encrenaz et al. [20], through observations in the infrared using TEXES (See Fig. 1.4), at 951-956 cm^{-1} (10.46 μm-10.52 μm), did not detect phosphine absorption lines, but instead proposed an upper limit of 5 ppb for its abundance, four times lower than the value obtained by Greaves et al. [29]. A possible reason for this discrepancy may be the different altitudes sounded, with a variation of abundance with altitude (Encrenaz et al. [20]).
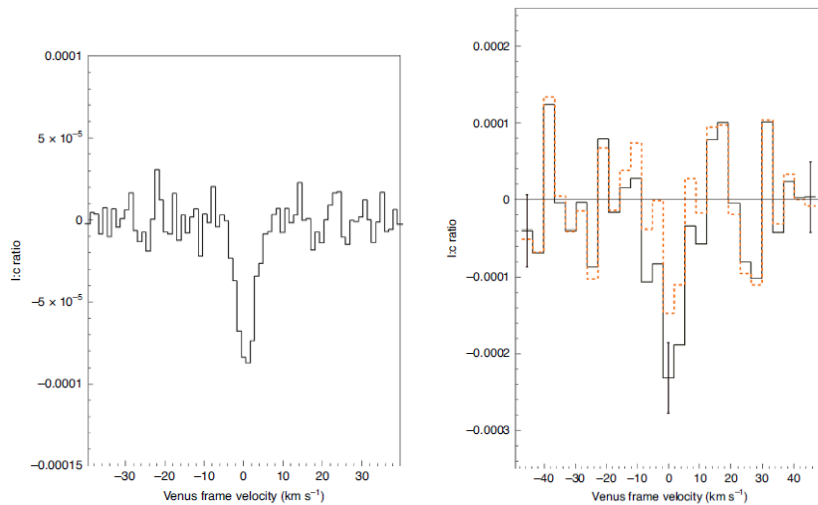
Figure 1.3: Reported detection of phosphine on ALMA and JCMT observations. The figures show the line-to-continuum ratio against Doppler-shifted velocity referenced to the PH_3 wavelength. **Left**: Reported detection of the PH_3 1-0 absorption line in the ALMA observations. Spectrum integrated for the whole planet. **Right** Reported detection of PH_3 1-0 absorption line in the JCMT observations. (images credits: Greaves et al. [29])
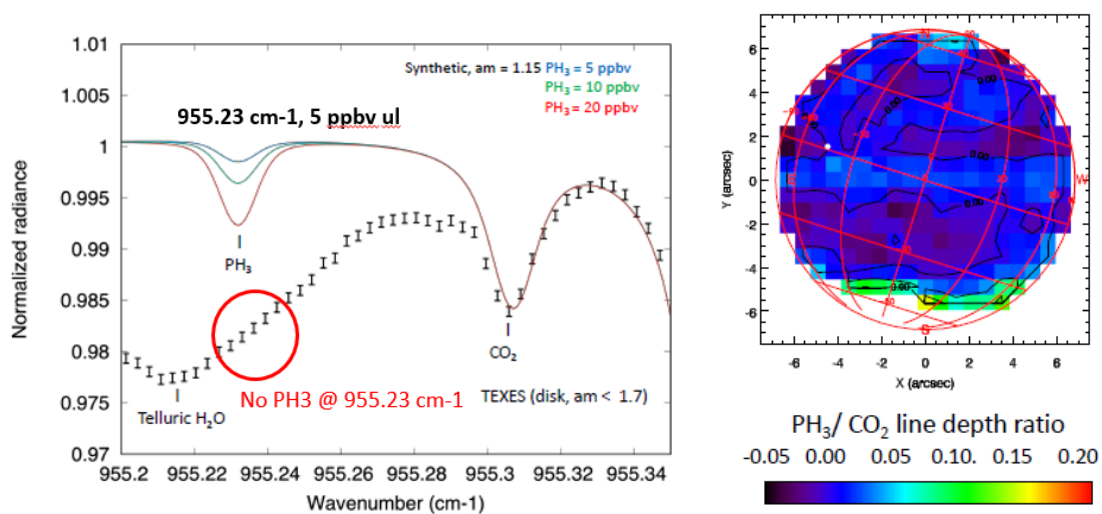
Figure 1.4: Left: Disk-integrated spectrum of Venus between 955.2 cm^{-1} and 955.4 cm^{-1}. A CO_2 line is detected on Venus, at around 955.31 cm^{-1} and telluric water absorption dominates the spectrum, at 955.2-955.28 cm^{-1}, precluding the detection of the phosphine absorption line, which should be detectable within the ref circle.**Right:** Map of the PH_3/CO_2 line depth ratio across the Venusian disk. (images credits: Encrenaz et al. [20])

1.1.3 The Importance of Sulphur Dioxide - Observations by TEXES

The sulphur chemical cycle is fundamental to the atmospheric chemistry of Venus (Zhang et al. [76]). Four sulphur species have been identified: SO_2, SO, OCS and H_2SO_4 (vapor and aerosols).
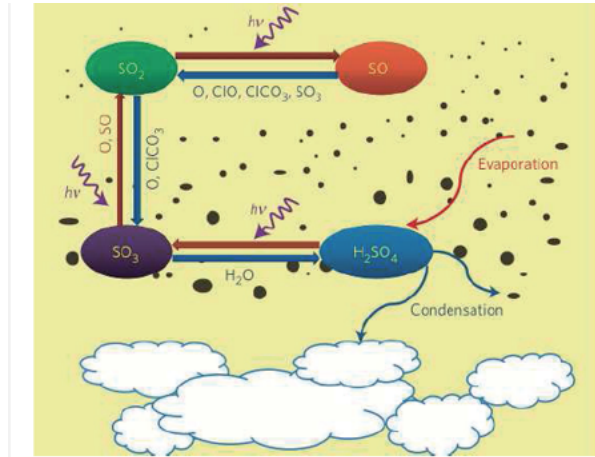
Figure 1.5: A representation of the sulphur cycle on Venus. (credits: Zhang et al. [75])

H_2O and SO_2 have abundances of 30 ppm and 100-150 ppm bellow the clouds, respectively (Bézard and Bergh [4]). They are transported upward in the atmosphere to the main cloud deck (40-70 km) by Hadley convection. Above the cloud top, located around 65-70 km, both species are subject to photodissociation due to solar UV radiation. To form the sulphuric acid clouds, SO_2 first reacts with oxygen atoms, forming SO_3 and later with H_2O:

$$CO_2 + SO_2 + h\nu -> CO + SO_3$$
$$SO_3 + H_2O -> H_2SO_4$$

$$(1.1)$$
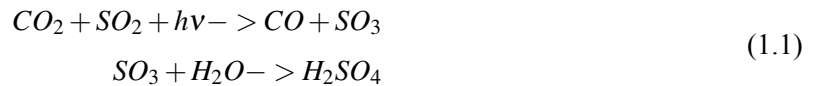
Above the cloud deck, the abundance of SO_2 is about 10-100 ppb (Zasova et al. [73]), as measured by Venera-15 and Pioneer. More recent results indicate an abundance of 100-1000 ppb, from SPICAV instrument on Venus Express (Marcq et al. [45]).

The abundance of SO_2 has both a short-time and long-term variability. The short-term variability (see Fig. 1.6) has a timescale of days and is characterized by variability with a factor of 5 to 10. The long-term variability can be characterized by variations up to a factor of 5 in 10-15 years (Encrenaz et al. [19])

Observations of the lower mesosphere have been done with TEXES, at the Infrared Telescope Facility (IRTF), around 7.4 μm, by Encrenaz et al. [17], corresponding to an altitude of $z \sim 65 km$ (See Fig. 1.6). These observations show a spatio-temporal variation of sulphur dioxide. This gas is most concentrated in patches and varies within a timescale of days.
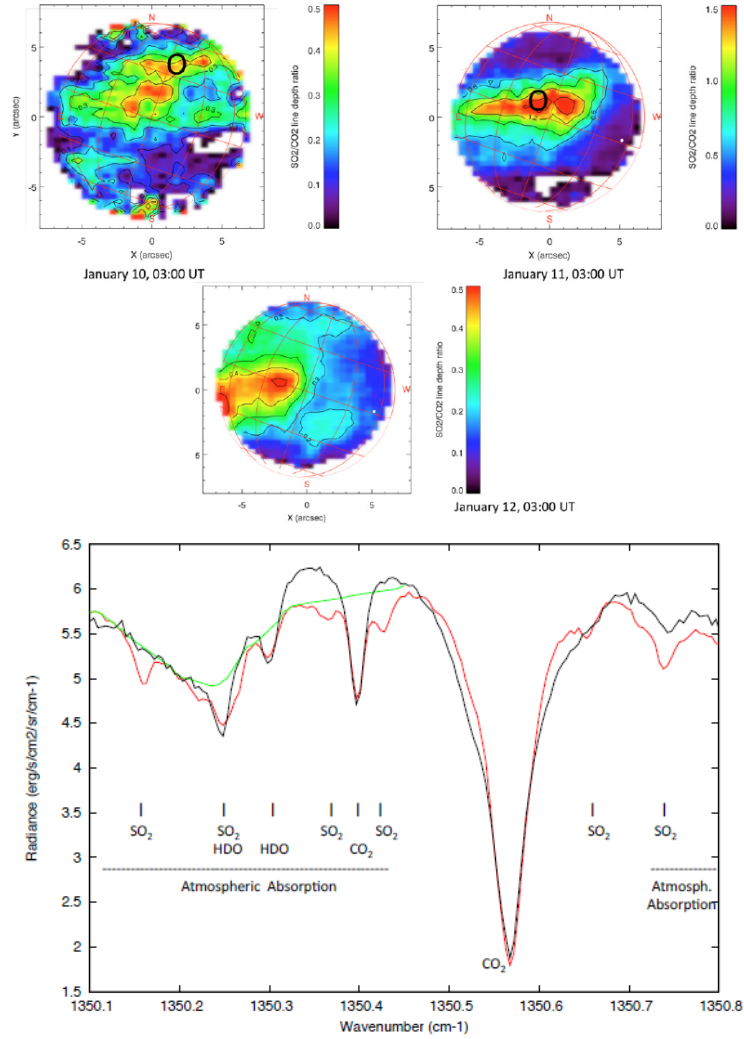
Figure 1.6: Mapping of SO_2 on Venus - Observations by TEXES. **Top:** Map of the line depth ratio of SO_2/CO_2 and its variability in time. From left to right: January 10, January 11, January 12 (2012). Values of the line depth ratio have a range of 0.0-0.5, for January 10 and 12, and 0.0-1.5, for January 11. **Bottom:** TEXES observations of Venus, around 1350.1-1350.8 cm^{-1} (7.4 μm). Red: spectrum corresponding the an area of the disk with maximum SO_2 abundance. Black: spectrum corresponding to an area of the disk with maximum CO_2. Green: modelled telluric absorption. (image credits: Encrenaz et al. [17]

1.1.4 Atmospheric Origin and Evolution

Three important factors that might have been important in the different evolutionary paths between Venus and Earth are the following: (1) the subduction of volatiles (through surface-atmosphere inter-actions, in particular CO_2); (2) the atmospheric depletion efficiency (due to high temperature and no presence of an internal magnetic field on Venus) and the different incident solar fluxes (Taylor et al. [63]).

The overall abundances of carbon and nitrogen on Venus are similar to Earth's, however there is significant lack of water compared to Earth's (see Table 1.1).

There is evidence this lack of water is due to continuous exospheric hydrogen escape and probably Venus lost most of its water supply 800 My ago (Donahue and Hodges [11], Kasting [34]). Determining the present rate of escape of H atoms and well as constrain the initial abundance of water on Venus is important in understand the evolution of its atmosphere and climate, since the water abundance is deeply connected with the temperature profile, due to the important role played in the formation of the clouds
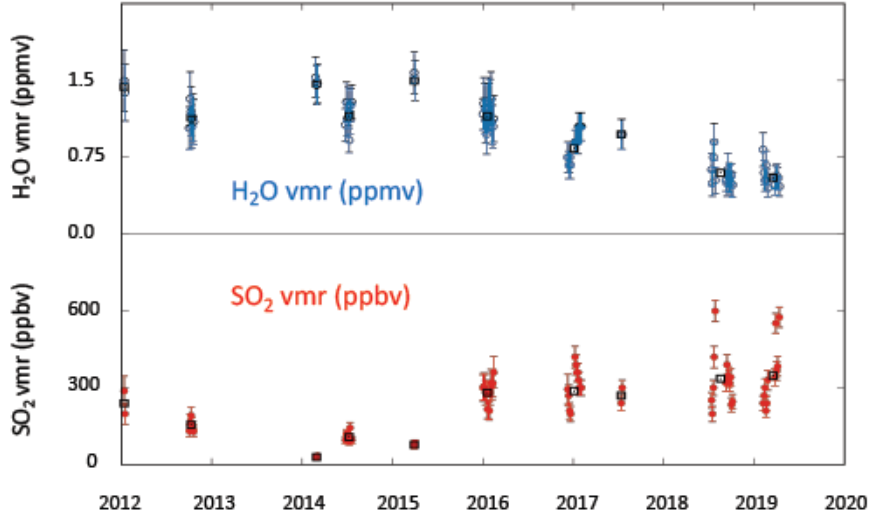
Figure 1.7: Summary of the results of TEXES observations, in the IR, between 2012 and 2020, of the variability of the volume mixing ratio of SO_2 and H_2O. (image credits: Encrenaz et al. [19])

Species	Earth	Venus
N_2	0.7808	0.035
O_2	0.2095	0-20 ppm
O_3	10 ppm	0.1-1 ppm (1)
CO_2	385 ppm (var)	0.965
PH_3	ppb-ppm (var) (2)	<5 ppb (3)
CH_4	3 ppm (var)	–
H_2O	<0.03 (var)(cond)	50 ppm
Ar	0.009	70 ppm
CO	0.2 ppm	50 ppm
SO_2	<2 ppb	60 ppm
HCl	–	0.5 ppm
HF	–	5 ppb
COS	–	250 ppb
He	5 ppb	12 ppm
Ne	18 ppm	7 ppm
Kr	1ppm	0.2ppm
Xe	0.09 ppm	< 0.1 ppm

Table 1.1: Composition of Venus's atmosphere compared with Earth's. Numbers in volume mixing ratio (mol/mol). Adapted from Sánchez-Lavega [58] and completed for the case of PH_3 and O3. (1) - Montmessin et al. [47]; (2) - Sousa-Silva et al. [61]; (3) - Encrenaz et al. [20]

and consequent albedo variation contribution to a possible early-based greenhouse effect (Kasting [34]).

Some planet formation scenarios for planets close to their star indicate the most of the water might be expelled in the first 100 Myr of their history (Hamano et al. [30]). Earth might also have lost most of its water by the same mechanism (Stuart et al. [62]). Therefore, to regain water, with an ocean with several meters deep, Venus would require substantial water delivery from exogenous sources (E.A. et al. [13]). High-resolution radar and global near-infrared mapping will help constrain ancient and current levels of geological activity. In-situ measurements of rare gases and their isotopes and stable isotopes ratios, as well as the D/H ratio will inform us about the ancient Venus climate and its evolution (Glaze et al. [27]).

At present, the D/H ratio on Venus has been constrained both in the lower atmosphere and upper atmosphere, with a great contribution from the european Venus Express mission (2006-2014). The D/H ratio is a tracer of escape processes and provides clues into the history of water on Venus. This mission improved our knowledge of the vertical profiles of the trace gases in Venus atmosphere, which are important in order to constrain models of atmospheric chemistry in the atmosphere and photochemistry. Moreover, the abundance of hydrogen-bearing species is important to the study of the escape of hydrogen and the evolution of the atmosphere. Measurements from the SOIR (Solar Occultation in the IR) instrument onboard Venus Express seem to indicate that the differential escape of H to D is happening at present, which could explain the high D/H ratio measured on Venus. The ratio of the escape rates of hydrogen and oxygen is a fundamental parameter to determine the dryness and oxidation state of the venusian atmosphere. The total ratio of loss is about 2:1, as measured by the VEx ASPERA-4 (Analyser of Space Plasma and Energetic Atoms) instrument, meaning that two atoms of hydrogen escape for one oxygen atom at present, providing evidence for atmospheric escape happening at present from H_2O (Titov et al. [66])
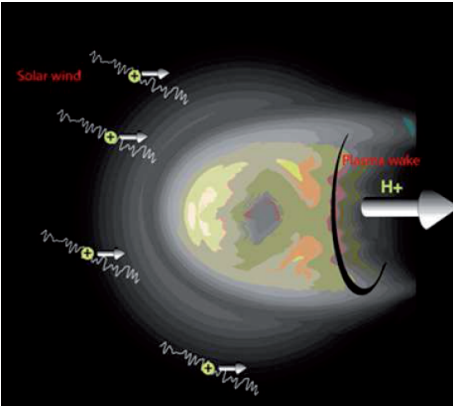
Figure 1.8: Atmospheric Escape Venus. The interaction of the Solar wind with the upper atmosphere of Venus generates an induced magnetic field. This interaction leads to exospheric escape of hydrogen and oxygen ions. (image credits: ESA's website)
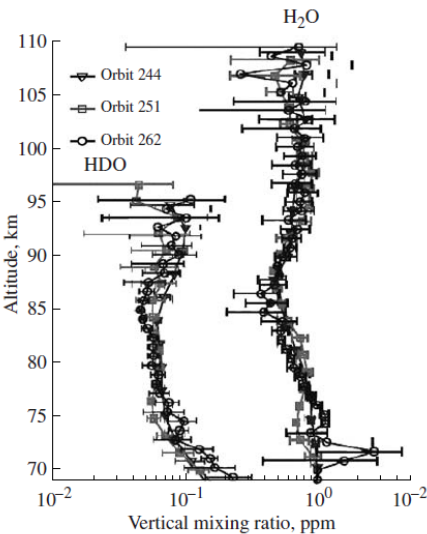
Figure 1.9: Vertical profiles of HDO and H_2O profiles in the upper atmosphere of Venus as measured by the SOIR instrument onboard Venus Express. (image credits: Titov et al. [66])

1.1.5 Determination of the D/H ratio - Observations by SOIR and CHFT

At the troposphere, D/H $\sim$ 157 D/H (Earth) (Donahue and Russel [12]). In SOIR measurements, D/H $\sim$ 240 D/H (Earth) (Fedorova et al. [21]) at the upper atmosphere. D/H ratios are commonly quoted relative to the Vienna Standard Mean Ocean Water (VSMOW; D/H (Earth) = 1.56 $\times 10^{-4}$).

The HDO and H_2O vertical distribution on Venus were measured in Venus's mesosphere by SOIR onboard Venus Express, using the solar occultation technique in the IR (Fedorova et al. [21]), at 2.61 μm (3830 cm^{-1}) (H_2O) and 3.58 μm (2715 cm^{-1}) (HDO). The resulting HDO and H_2O profiles are shown in Fig. 1.9.

Ground-based observations of Venus night-side by the Canada-Hawai-France-Telescope (3.6 m) on Mauna Kea, at 2.34-2.43 μm (4115-4273 cm^{-1}), with a resolution of 0.23 cm^{-1}, searched for HDO and H_2O lines to estimate the D/H ratio present in the lower atmosphere (de Bergh et al. [7]). The value obtained was D/H = 80-160 D/H (Earth). These wavelengths sound altitudes between 32 and 42 km (de Bergh et al. [7]).
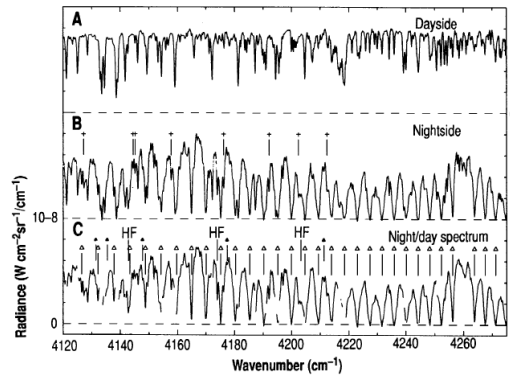
Figure 1.10: Ground-based observations of Venus in the night-side, in the NIR, at 4115-4273 cm^{-1}. Both day-side and night-side radiance spectra were recorded (A and B, respectively). The night-side spectrum was corrected for reflected sunlight contamination, by dividing the night-side spectra by the day-side (C). The spectrum is dominated by 12CO absorption lines (signalized by triangles). (image credits: de Bergh et al. [7])
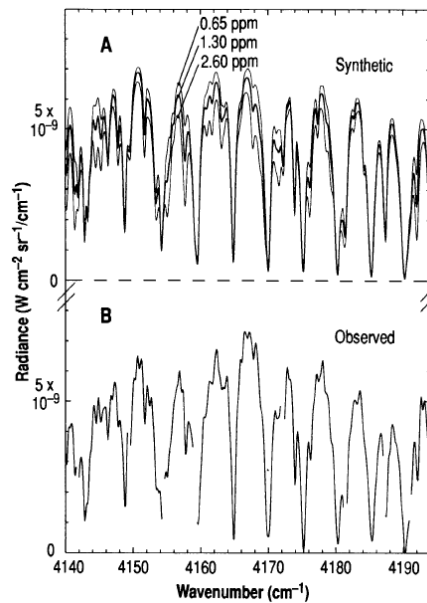
Figure 1.11: Ground-based observations of Venus in the night-side - Zoom around 4140-4190 cm^{-1}. The spectrum is dominated by CO absorption lines. The other weaker lines are due to, mainly, HDO. However, there is also a smaller contribution from H_2O absorption. (images credits: de Bergh et al. [7])

1.2   Mars

Mars has a mass that is about 15 % that of Earth and a density of 3.93 g/cm^3 (compared with 5.51 g/cm^3 for Earth). Contrary to Venus, Mars has a surface where the rovers can land and explore the landscape, making this planet the most likely for humankind to colonize in the future.

Additionally, the day and year in Mars are very similar to Earth's. The day has 24h 37m and the year 687 days. The axial tilt is also close to Earth's, with a value of 25.2º, giving rise to seasons like on Earth.

The atmosphere of Mars, is mainly composed of CO_2 (95 %), N_2 (2.7 %) and Ar (1.6 %), between other minor species such as H_2O, CO and Ne (see Table 1.5). However, its atmosphere is extremely thin, with a surface pressure 100 times less than Earth´s (about 7 mbar). As a consequence of the thin atmosphere, the temperature at the surface can vary between 130 K and 308 K with a mean value of 210 K.
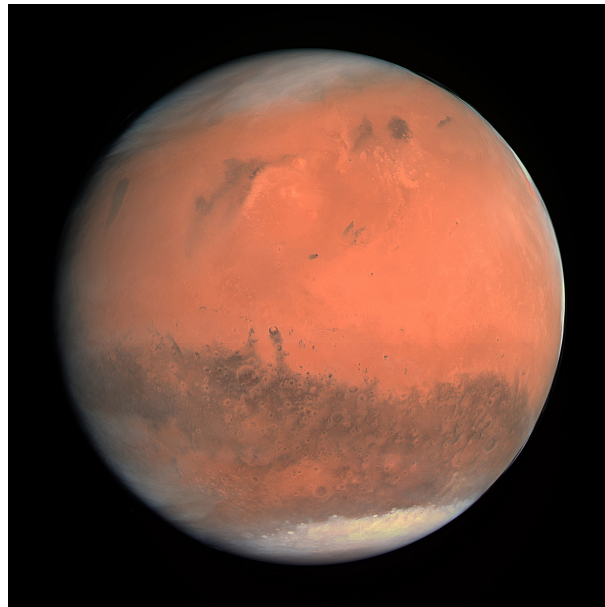
Figure 1.12: Mars as seen by the OSIRIS instrument onboard the european Rosetta mission. (image credits: ESA's Rosetta mission)

The surface has channels that are evidence for the past or present flow of liquid water on the surface. Recently, evidence for the existence of a huge subterranean water lake was claimed, with about 19 km in size, beneath the martian south pole (Orosei et al. [51]). There is also evidence for the existence of a large ocean in the past in one of the planet's hemispheres (Dibiase et al. [10]).

The red planet is therefore one the most important targets of astrobiological interest in the Solar System, since where there is water there are habitability conditions (Vago et al. [67]).

1.2.1   The Quest for Methane on Mars - Mars Express and ExoMars Observations

The first report on the detection of methane on Mars came out in 2004 by Krasnopolsky et al. [39]. A spectrum of Mars was recorded at the P-branch of the strongest CH_4 band at 3.3 μm with a resolving power of R=180000, using the Fourier Transform Spectrometer at the Canada-France-Hawai Telescope (CFHT). An estimated amount of 10 ppb was retrieved for methane. Krasnopolsky et al. [39] argued that methane production by hydrothermal, magmatic, cometary or interplanetary origin cannot account for the measured abundance. Therefore, they proposed the possibility of a biogenic origin. Later on in 2009, a set of measurements of three ground-based high-dispersion infrared spectrometers (CSHELL/IRTF,

Species	Earth	Mars
N_2	0.7808	0.027
O_2	0.2095	0.13 ppm
CO_2	385 ppm (var)	0.953 (cond)
CH_4	3 ppm (var)	33 ppb (var)
H_2O	<0.03 (var)(cond)	0-300ppm (cond)
Ar	0.009	0.016
CO	0.2 ppm	700 ppm
O_3	10 ppm	0.01 ppm
NO	<0.01 ppm	3 ppm
H_2	0.5 ppm	10 ppm
Ne	18 ppm	2.5 ppm
Kr	1 ppm	0.3 ppm
Xe	0.09 ppm	0.08 ppm

Table 1.2: Composition of Mars's atmosphere compared with Earth's. Numbers in volume mixing ratio (mol/mol). var- variable in space and time; cond- condensable. Adapted from Sánchez-Lavega [58]

NIRSPEC/KECK-2), reported variations of the methane abundance with latitude, longitude and season and a maximum peak abundance of 45 ± 10 ppb of methane measured (Mumma et al. [50]).

There are reports of both positive and negative detections of methane on Mars. The discrepancy between these has generated much debate.

The first independent confirmation of a positive detection of methane on Mars was performed by spot-tracking nadir observations of Gale Crater by the Planetary Fourier Spectrometer (PFS) instrument on Mars Express (MEx), taken in the IR (3.3 μm), on June 2013 (Giuranna et al. [26]). This mode allows the acquisition of several hundred spectra within a very short time (tens of minutes), increasing the SNR of the observations. Through the use of improved observational geometry and data treatment and analysis, a methane absorption line at around 3018 cm^{-1} was detected, corresponding to an estimated abundance of 15.5 ppb. This detection was done one day after the in-situ detection of methane by Curiosity (Webster et al. [72]), also near Gale Crater. This study suggests methane is released by the surface, in regions where faults meet shallow ice formations, and this release is characterized by being short and small (Giuranna et al. [26]).

A recent example of a negative detection of methane on Mars follows from highly sensitive measurements of the martian atmosphere by the ExoMars Trace Gas Orbiter (TGO) NOMAD (Nadir and Occultation for MArs Discovery) and ACS (Atmospheric Chemistry Suite) instruments, from April-August 2018 (Korablev et al. [35]), in solar occultation geometry. These observations are best suited for detection of minor atmospheric species due to two main factors: (1) the Sun's brightness increases the SNR of the spectra and (2) ten times longer atmospheric optical path in relation to nadir geometry (looking to the surface). The spectral range of the instruments covers the 3.3 μm spectral range, where the strongest fundamental absorption bands of methane are located. Observations were performed before the great dust storm of August 2018 by the ACS instrument and during by the NOMAD instrument. For a combination of different latitudes of measurements in both hemispheres, in general for high latitudes (most is above -40º latitude and above 40º latitude), methane was not detected. Instead, an upper limit for its abundance was derived to be about 0.05 ppbv, near 100 times lower than previous detections (Mumma et al. [50],

Webster et al. [72]). The optimal altitude to search for methane is located around 5-25 km, according to Korablev et al. [35], corresponding to an equilibrium between two effects: (1) the increase of sensitivity when the line of sight of the instrument samples closer to the surface; (2) the decrease of sensitivity closer to the surface due to the presence of dust and clouds. The authors claim that a possible explanation for the mismatch between this study and the one from Giuranna et al. [26] is the existence of an unknown process that rapidly removes methane from the lower atmosphere before it spreads globally on Mars.
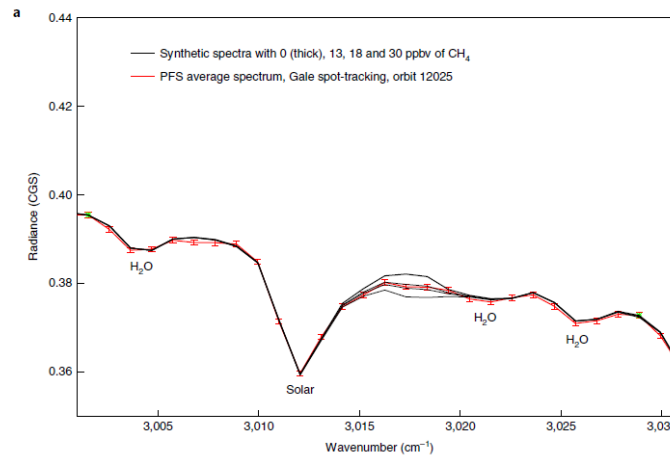
Figure 1.13: Positive detection of methane by the MEx mission. Measured integrated radiance spectrum, in cgs units (erg s-1 cm-2 sr-1 (cm-1)-1), taken by the PFS instrument on MEx, showing a methane absorption line at around 3018 cm^{-1}, by summing hundreds of spectra. (image credits: Giuranna et al. [26])

1.2.2 Atmospheric Origin and Evolution

Evidence points to an early Mars that was both warmer and wetter than the present day planet. Two possible explanations for the evolution of the martian atmosphere include: (1) substantial reservoirs of water in the form of subsurface ground ice, polar caps and hydrated mineral deposits; (2) lost of most of the atmosphere to outer space, through the escape of water, carbon monoxide and volatiles ([1]).

In 2005, the OMEGA (Observatoire pour la Minéralogie, l'Eau, les Glaces et l'Activité) instrument onboard Mars Express discovered, for the first time, hydrated minerals in the surface of Mars, indicating that in the past the planet sustained stable liquid water on the surface for a long period of time. Two types of hydrated minerals were discovered, mainly on one hemisphere of the planet: phyllosilicates and hydrated sulfates. Both minerals result from the chemical alteration of rocks by water but form by different processes. In conclusion, the evidence points out to two different climatic episodes in the history of Mars: a moist environment where phillosilicates formed followed by a more acidic environment when the sulphates formed (Poulet et al. [56]).

Through time, most of the atmospheric CO_2 condensed. This effect, together with the fact that CO_2 is a good Rayleigh scatterer (tending to increase the albedo), can explain why Mars went colder. Therefore, one hypothesis to explain how early Mars might have remained warm might be related to the fact that maybe the planet was covered in CO_2 clouds, with particles sizes in the order of the mid-IR, such that backscattered light from the surface (thermal-IR) would have outweighed the effect of the reflection of incoming sunlight back to space (VIS/near-IR). Some models indicate that methane could have heated early Mars. (Sanchez-Lavega [58])

The isotopic ratios of $^{13}C/^{12}C$, $^{15}N/^{14}N$, $^{18}O/^{16}O$ and $^{38}Ar/^{36}Ar$ on Mars have higher values that on Earth, indicating that up to 50-90 % of the initial CO_2, N_2 and Argon were lost to space (Sanchez-
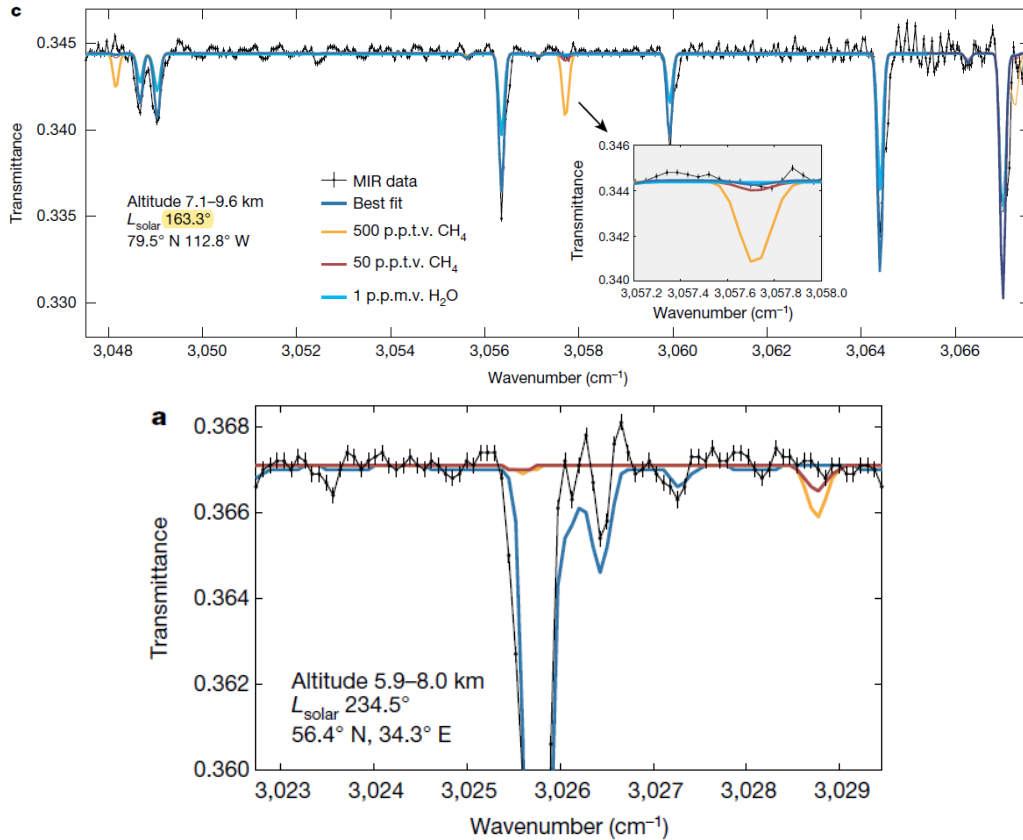
Figure 1.14: Negative detection of methane by the ExoMars mission. **Top:** : Transmittance spectrum taken by the ExoMars TGO ACS instrument before the dust storm. Absorption lines of methane should be present at around 3048 cm^{-1} and 3068 cm^{-1}, as predicted by simulations (yellow line). **Bottom:** Transmittance spectrum measured by the ExoMars TGO NOMAD SO instrument onboard MEx during the dust storm. Data - Black; Blue - synthetic model with 1 ppm of H_2O and no methane; Yellow - Synthetic model with 0.5 ppb of methane; Red - synthetic model with 0.05 ppb of methane (image credits: Korablev et al. [35])

Lavega [58]). This seems to contradict results from the ASPERA-3 intrument onboard Mars Express, that indicate that in the past 3.9 Gyr no more that 10 mbar of atmosphere were lost through ion escape (Ramstad et al. [57]). Several processes can explain the atmospheric depletion such as impact-driven erosion, hydrodynamical and non-thermal escape processes, and surface adsorption and weathering of the CO_2, accumulating in the surface.(Sanchez-Lavega [58])

Stable isotope ratios of C, O and H have been measured in situ by the TLS instrument on Curiosity, around 2.78 μm. The D/H and $^{18}O/^{16}O$ ratios were measured in water, while $^{13}C/^{12}C$ and $^{18}O/^{16}O$ were measured in CO_2. The comparison between these ratios and the ones derived from meteorites suggest that martian reservoirs of CO_2 and H_2O were already established 4 Gyr ago. However, atmospheric loss may still be ongoing today.

Analyses of meteorites, namely SNC-class meteorites (shergottite, nakhlite and chassigny), with different D/H ratios suggest two evolutionary periods in the history of Mars: one first period, early in Mars history, when a significant loss of atmosphere occurred, before 3.9 Gyr followed by a second period with moderate loss of atmosphere that continues until today (Webster et al. [71]). The D/H ratios obtained from meteorites comes from analysis of the water content of secondary alteration minerals. The investigation of the absolute escape rates of H and O was investigated by the ASPERA-3 instrument onboard Mars Express. It concluded that the solar wind interaction with the upper atmosphere contributes to atmospheric depletion, which is active today. The solar winds energises and ionises the molecules in the

Isotopic ratios	Earth	Mars
D/H	1.5×10^{-4}	8×10^{-4}
$^{12}C/^{13}C$	89	90
$^{14}N/^{15}N$	272	170
$^{16}O/^{18}O$	489	515
$^{36}Ar/^{38}Ar$	5.3	5.5

Table 1.3: Isotopic ratios on Earth and Mars. The values are averages. D/H (solar) = $2-70 \times 10^{-5}$; D/H (comets) = 3×10^{-4}. $^{14}N/^{15}N$ (solar)=357; $^{12}C/^{13}C$ (solar)=84; $^{36}Ar/^{38}Ar$ (solar)=5.77. Adapted from Sánchez-Lavega [58]

upper atmosphere, that by exchanging charge become neutral and escape.

The ion escape rate depends on the solar wind flux and ultraviolet flux. In the end, the estimated escape rate of H and O ions is insufficient to explain the large amount of water and atmosphere lost in the past 3.5 Gyr.

The total amount of water contained in the planet's south pole today is enough to cover the entire globe with a water layer of 11 m. These results are important to constrain the atmospheric evolution of Mars (Plaut et al. [54]).

1.2.3 Determination of the D/H ratio - Observations by ExoMars and SOFIA

The D/H ratio can be affected by climatological processes, since the condensation/sublimation points of water and HDO are different and depend on local temperature, saturation levels and aerosol column abundances. This can produce a seasonal, temporal and spatial variation of the D/H ratio on the atmosphere. as reported in the southern summer hemisphere (Montmessin et al. [48]).

ExoMars solar occultation observations, by the NOMAD SO instrument, centred at 3.6 μm (2730 cm^{-1}) (HDO) and at 3.3 μm (3025 cm^{-1}) (H_2O), show that the water vapor abundance in the middle atmosphere (40-100 km) increases up to 2 orders of magnitude during a Global Dust Storm (GDS), reaching altitudes of 100 km (Villanueva et al. [70]). In this study, HDO was be mapped up to 50 km and H_2O up to 100 km . Global Circulation Models explain this considering that the storm-induced higher atmospheric temperatures, up to 30 K, act to reduce ice cloud formation and therefore allowing water to move upward in the atmosphere. Water also reaches similar altitudes during the southern summer solstice. However, close to the equinoxes, the water abundance decreases. The D/H ratio measured is near 6 at the low atmosphere. It decreases with altitude, to fractionation processes and is low (2-4) close to equinox at high/low latitudes. The observed variations of the D/H ratio across seasons and altitude can be atributed to Rayleigh fractionation and cloud formation.

Three processes can contribute to the escape of water on Mars, the Global Dust Storms, Regional Dust Storms and the summer seasons, through photolysis of water in the upper atmosphere.

The current rate of escape of H and O ions have been measured. However, that is not the case for C, N and Ar lighter isotopes, whose escape rates were estimated by models and extrapolated to the past 3.9 Gyr. Ion loss, through H+ and O+ cannot account for the atmospheric mass loss, however the isotopic ratios point out to massive lost of C, N, O and Ar in the first 600 Myr of Mars history, followed by moderate loss (Jakosky et al. [33]).

The measurement of the D/H ratio on Mars can provide valuable information. We can determine both a global and a local value for the D/H ratio, which hold the key to different questions (Encrenaz et al. [18]). The global value, i.e., integrated in latitude, longitude and season, may be compared with the D/H

ratio measured in clays at the martian surface, reporting to the early Mars. This value will then be useful in the study of the abundance of water on Mars through time. The variation of this value is determined by fractionation processes, through different escape rates associated with the deuterium and hydrogen atoms (Owen et al. [52]). The hydrogen atoms escape more easily than the deuterium atoms, since the former are lighter. The local value, varying with altitude, season and location can constrain the present sources and sinks of water in the surface and atmosphere (Encrenaz et al. [18]). To perform studies of the D/H ratio on Mars, space-based instruments and orbiting probes are used, avoiding the effect of the terrestrial absorption. One such instrument is the Echelon Cross Echelle Spectrograph (EXES) onboard the Statospheric Observatory for Infrared Astronomy (SOFIA). In Encrenaz et al. [18], EXES was used to observe H_2O, HDO and CO_2 transitions at 1383-1391 cm^{-1} (7.19-7.23 μm), for April 2017 and March 2016 observations (see Fig. 1.15, Fig. 1.16) The mixing ratios of H_2O and HDO relative to CO_2 can be related with the ratio of the depth of the HDO and H_2O lines to the CO_2 lines. This method is valid provided the lines of the two minor species are weak, with depths weaker than about 10 %, and that the two species are homogeneously mixed.

The disk-integrated D/H ratio measured was 3.4-4.8 $\times$ D/H(Earth), for the March 2016 observations, and 3.9-5.2 $\times$ D/H (Earth), for April 2014 observations.
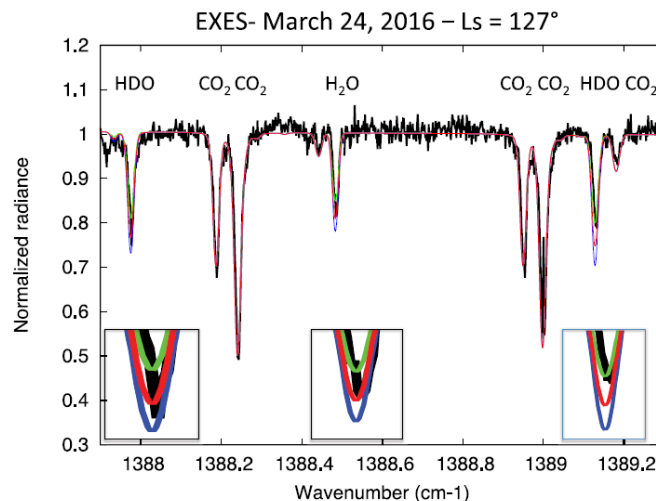
Figure 1.15: Determination of the D/H ratio on Mars - Observations by EXES, onboard SOFIA, around 1383-1391 cm^{-1}. Spectrum of the northern hemisphere of Mars at March 2016. The stronger lines are from CO_2 and there are several weaker HDO and H_2O lines. The HDO line at 1388 cm^{-1}, the HDO line at 1389.1 cm^{-1}, the H_2O line at 1388.5 cm^{-1} were modelled for different H_2O and HDO abundances to estimate the D/H ratio (image credits: Encrenaz et al. [18])

.

1.3 Jupiter

Jupiter is the the most massive planet of the Solar System, about 300 times the mass of the Earth. It has a diameter of about 10 Earth radius and a rotation period of about 10 hours. It appears as a ochre-colored oblate planet seen through a telescope. The color contrast in Jupiter is the biggest of any Solar System object. Four large moons, widely known, orbit around the planet, know as the Galilean satellites. They are, from closest to more distant to the planet, Io, Europa, Ganimedes and Calisto.

Since the formation of Jupiter, several possible processes altered its atmosphere, such as thermal escape, cometary bombardment and internal differentiation.

Jupiter is mainly composed of hydrogen (86 %) and helium (14 %), which were accreted directly
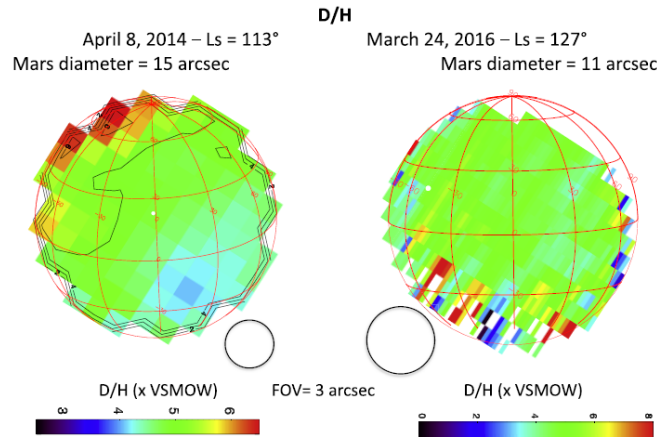
Figure 1.16: Determination of the D/H ratios on Mars - Observations by EXES, onboard SOFIA, around 1383-1391 cm^{-1}. Maps of the D/H ratios on Mars, for April 2014 and March 2016 (image credits: Encrenaz et al. [18])

.

from the solar nebula. Some minor components present in Jupiter's atmosphere are H_2O, CH_4, PH_3, NH_3, H_2S, C_2H_2, C_2H_6, among many others (see Table. 1.4).

The globe of Jupiter is divided in horizontal stripes, called zones and belts. The zones correspond to bright cloudy regions were the air is moving up and the belts correspond to cloud-free dark regions were the air is moving down (see Fig. 1.17, middle image).

The mean temperature at the equator is about 163 K and corresponds to a pressure of about 1 bar.

The atmosphere of Jupiter is divided into troposphere (tens of bars up to 100 mbar), stratosphere (100 mbar-1mbar), mesosphere (1mbar-1μbar) and thermosphere ($<$1μbar) (see Fig. 1.18). The troposphere is the region where condensate clouds form and the temperature decreases with decreasing pressure, the stratosphere is the region where the temperature increases with decreasing pressure, due to hydrocarbon and haze heating, and the mesosphere is an almost isothermal layer.

The increase of temperature with height in the stratosphere implies the presence of additional energy sources, such as (1) absorption of ultraviolet radiation from the Sun via gaseous photodissociation ; (2) absorption of light in the NIR from aerosols and (3) absorption of NIR sun-light.

Remote-sensing and in-situ observations of the vertical profiles of pressure, temperature and composition provide constraints on vertical motion, heat sources, composition and photochemistry ([32]).

The study of "disequilibrium" species provides information on vertical transport and circulation on the atmospheres of the giant planets. Those species are in "disequilibrium" due to the rapidly changing, turbulent atmosphere.

Phosphine is one such disequilibrium species present in Jupiter's atmosphere. Is predicted to be produced by equilibrium chemistry at T$\sim$1000K and P$\sim$1 kbar, i.e., in the deep layers of Jupiter's atmosphere. From there, it is transported upward, until it is destroyed in a timescale of about 100 days by UV solar radiation (Irwin [32]).

Methane photo-dissociation takes place at 0.1μbar-0.1 mbar. However, the combination of the photo-dissociation products requires pressures higher than 0.1 mbar. The main products of methane photo-dissociation by UV solar radiation are acetylene (C_2H_2), ethane (C_2H_6) and polyacetylenes (($C_2H_2)_n$).

From calculations using a simple equilibrium cloud condensation model (Atreya [2], Lewis [41]), NH_3 is predicted to form an ice cloud at $\sim$0.7 bar. The ammonia profile is expected to have two "knees", where the abundance decreases, located at the ammonium hydrosulfide cloud layer at 1-2 bars and at the ice cloud layer at 700 mbar-500 mbar. This is consistent with ground-base disk-averaged microwave

Species	Jupiter	Saturn
H_2	0.864	0.881
He	0.136	0.11-0.16
H_2O	$2 - 20 \times 10^{-9}$ (P<50 mbar)	1.7×10^{-7} (strat)
	6×10^{-4} (19 bar, cond)	
CH_4	2.1×10^{-3}	4.5×10^{-3}
NH_3	2.6×10^{-4} (cond)	5×10^{-4} (cond)
	8×10^{-4} (8 bar)	
H_2S	7.7×10^{-5} (16 bar) (reac)	(4×10^{-4}) (reac)
PH_3	6×10^{-7} (dis)	7×10^{-6} (dis)
C_2H_2	$3 - 20 \times 10^{-8}$ (phot)	2.1×10^{-8} (phot)
C_2H_6	$1 - 5 \times 10^{-6}$ (phot)	3×10^{-6}(phot)

Table 1.4: Composition of Jupiter's atmosphere. Numbers in volume mixing ratio (mol/mol). phot- photo-dissociation product; dis-disequilibrium species; cond- condensable species; reac - reactive species. Adapted from Sánchez-Lavega [58]
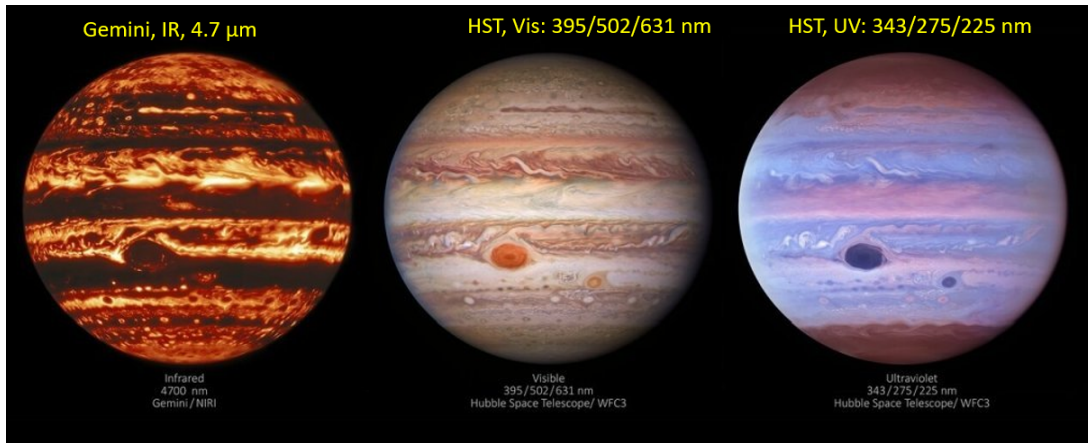
Figure 1.17: Jupiter observed at different wavelengths. **Left:** Gemini, IR, 4.7 μm; **Middle:** Hubble Space Telescope (HST), visible, 395/502/631 nm; **Right:** HST, UV, 343/275/225 nm. Different wavelengths of observation correspond to different altitudes/pressures sounded. For example, the pressure sounded for IR wavelengths is higher than the pressure sounded for visible light.

observations. However, NH_3 in found to be depleted in 5 μm hotspot areas. This is still not understood today (Irwin [32]).

The main cloud deck of Jupiter seems to be present at 1 bar, and evidence points out that it is made by haze layers composed by the photo-dissociation products of methane, ammonia and phosphine. These haze layers seem to be blended with a "contaminated" ammonia ice cloud, whose features are not detected in mid IR spectral observations (Irwin [32]).

The vertical composition profiles of Jupiter atmosphere are presented in Fig. 1.19

1.3.1 Atmospheric Origin and Evolution

The measurement of elemental abundances and isotopic ratios is fundamental for understanding the origin and evolution of the planets atmospheres.

The value of the D/H ratio of Jupiter and Saturn inform us about the conditions of formation of these planets. If these planets formed from accretion of gas from the protosolar nebula, then the D/H ratio measured should be similar to the measured solar D/H ratio (Thérèse and Dunlop [65]).
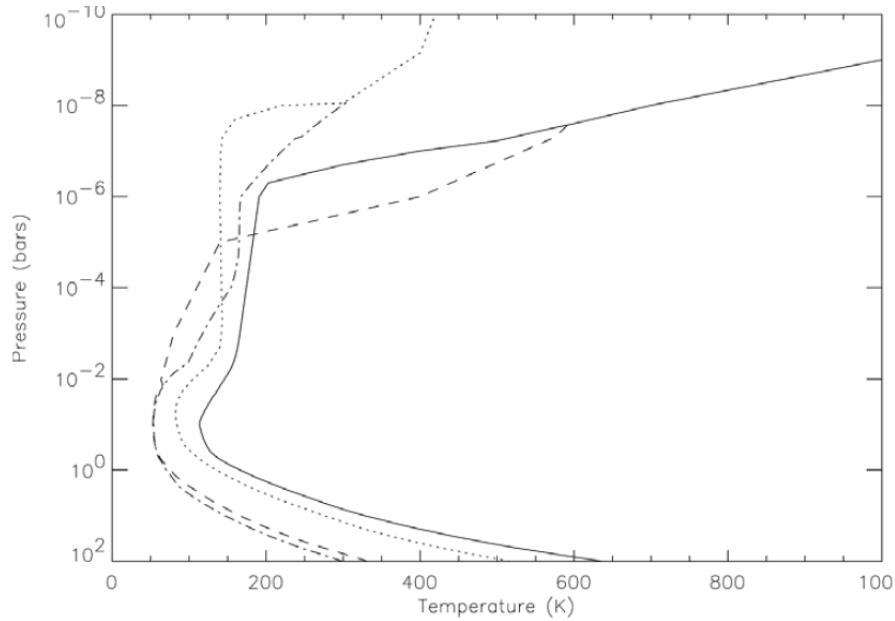
Figure 1.18: Thermal Structure of the Giants Planets. Temperature (K) in horizontal axis and pressure (bar) in vertical axis. Equatorial temperature-pressure profiles of the giant planet atmospheres; Jupiter - solid line, Saturn - dotted line, Uranus - dashed line, Neptune - dot-dashed line. (image credits: Irwin [32])
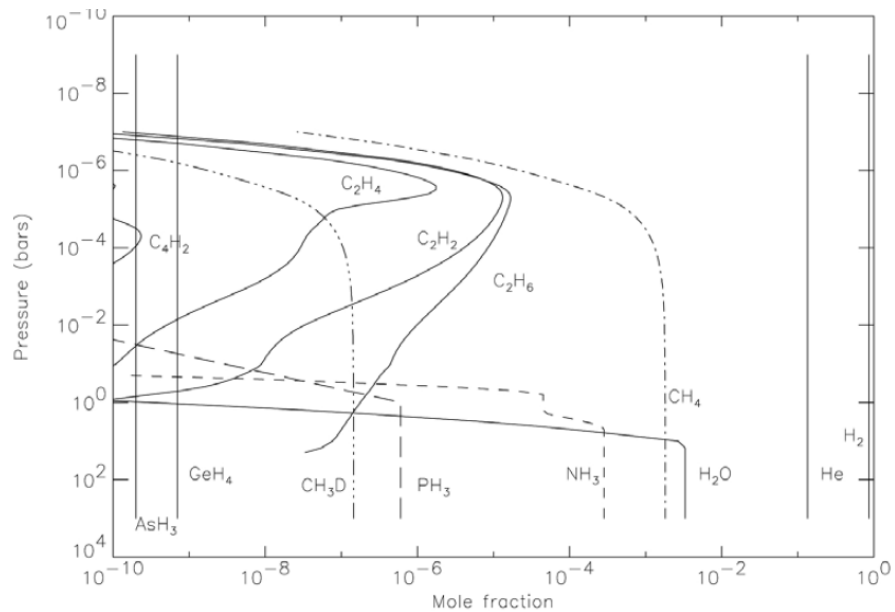
Figure 1.19: Observed and modelled profiles in the atmosphere of Jupiter. Mole fraction (mol/mol) in horizontal axis and pressure (bar) in vertical axis. (image credits: Irwin [32])

There are other elemental ratios, such as the C/H and N/H ratios important for constraining planetary formation mechanisms and distance of formation from the Sun. C/H and N/H ratios are enriched in the giant planets in relation to the solar value and decreases with increasing heliocentric distance. Other important elemental ratio is the P/H, which traces the dynamics of the atmosphere. For example, PH_3 is a disequilibrium species in Jupiter's atmosphere, such that detecting this species in the upper atmosphere indicates up-welling from the deeper layers of the atmosphere. The O/H is less than the solar ratio. Thermal emission spectra are used to determine the ratios . The values of the elemental ratios in Jupiter are represented in Fig. 1.20. (Thérèse and Dunlop [65])

According to the current model, the giant planets formed by the following process: a 10-15 earth mass
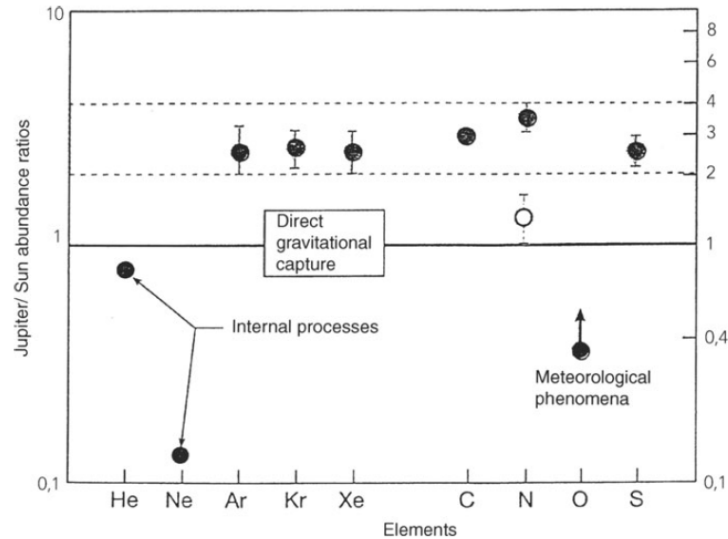
Figure 1.20: Elemental ratios in Jupiter divided by the solar elemental ratios. In general, the elemental ratios are enriched in Jupiter, by a factor between 2 and 4 in respect to the solar ratios. The O/H, He/H and Ne/H ratios are lower than solar possibly due to meteorological phenomena and internal processes, respectively. (image credits: Owen et al. [53])

core mainly made by ices accreted hydrogen and helium in the early Solar System. The temperature of this object increased with time, subliming some elements from the ices and therefore enriching the atmosphere in C, N and O in relation to hydrogen. (Thérèse and Dunlop [65])

Some isotopic species have been detected on Jupiter, like HD, CH_3D, $^{13}CH_4$, $^{15}NH_3$ as well as isotopes of H_2S and of the noble gases.

The carbon, nitrogen and oxygen isotopic ratios ($^{13}C/^{12}C$, $^{14}N/^{15}N$ and $^{16}O/^{18}O$) are important for the study of nucleosynthesis and the chemical evolution of our galaxy. ^{13}C is mainly produced in the "cold" CNO cycles in the main-sequence of stars. In the Sun, inner planets, moon and meteorites the value is constant, 89. ^{15}N formed mainly in "hot CNO cycle" in nova and supernova explosions. It is important to compare the value of $^{13}C/^{12}C$ ratio in the most primitive regions of the solar system with current values of the interstellar medium to study the chemical evolution of our galaxy. The $^{14}N/^{15}N$ ratio in Jupiter is enriched with a factor of 2 in relation to the terrestrial value.

Species	Jupiter	Solar
D/H	2.2×10^{-5}	$2 - 70 \times 10^{-5}$
$^{13}C/^{12}C$	92.6	84
$^{14}N/^{15}N$	435-450	357
$^{36}Ar/^{38}Ar$	5.6	5.77

Table 1.5: Isotopic ratios on Jupiter compared to solar ratios. Table adapted from Sánchez-Lavega [58]

1.3.2 Determination of the D/H ratio - Observations by ISO

Using the Short Wavelength Spectrometer (SWS) and the Long Wavelength Spectrometer (LWS) instruments onboard the Infrared Space Observatory (ISO) mission analysed observations of Jupiter and Saturn spectra at 2.3 μm-180 μm, with a resolving power of R=150-30000, depending on the grating mode of the spectrometer. The main conclusions of the study were: (1) detection of water vapour in the deep troposphere of Saturn; (2) the detection of new hydrocarbons in Saturn's stratosphere (CH_3C_2H,

C_4H_2, C_6H_6, CH_3); (3) the detection of water vapour and carbon dioxide in the stratospheres of Jupiter and Saturn; (4) new determination of the D/H ratio using the detection of new HD rotational lines ((Encrenaz et al. [16])).

I want to focus on the results of the analysis of the 6 μm-14 μm spectral region on Jupiter observations (see Fig. 1.21). This wavelength interval is sounding a region just bellow and above the tropopause. Therefore, the spectrum has both emission (CH_4 at 7.7 μm) and absorption lines (NH_3, CH_3D, PH_3). The continuum in this regime is due to the hydrogen-helium pressure-induced spectrum and to the NH_3 cloud. Abundances of 2.1×10^{-3} and 2.5×10^{-7} were assumed for CH_4 and CH_3D, respectively, in Encrenaz et al. [16].

Later analysis of the SWS data on ISO were performed by Fouchet [23], to determine the abundance of NH_3, and by Lellouch et al. [40], to determine the D/H (CH_4) and D/H (H_2) ratios from a fit to the methane emission band at 7.7 μm and deuterated methane absorption band at 8.6 μm (see Fig. 1.22 and Fig.1.23, respectively). Fouchet [23] obtained the NH_3 profile show in Fig. 1.24, and concluded that the spectrum at the 10 μm region is sounding the atmosphere at around 0.2-1 bar. Lellouch et al. [40] estimated the abundances of CH_4 an CH_3D as, respectively, 1.8×10^{-3} and 1.6×10^{-7}. Then, the following values were obtained: $D/H(CH_4) = (2.2 \pm 0.7) \times 10^{-5}$ and $D/H(H_2) = (2.25 \pm 0.35) \times 10^{-5}$. These values are consistent with values determined for the protosolar D/H ratio measured from the solar wind. A summary of the retrieved abundances of CH_4, CH_3D, NH_3 and PH_3 is presented in Table 1.6
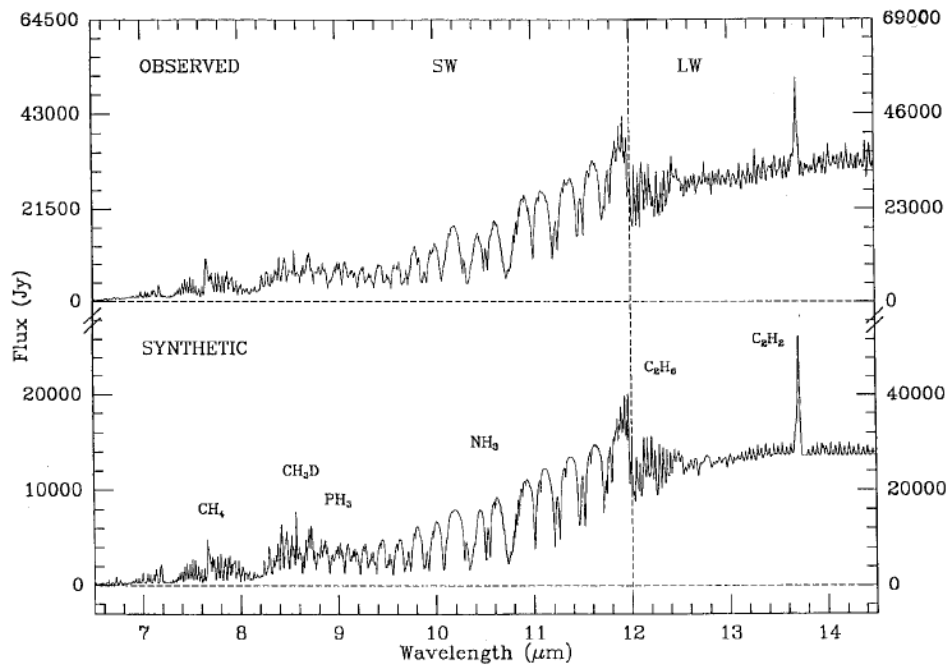
Figure 1.21: Mean Jupiter spectrum recorded by the SWS instrument on ISO, at 6 μm-14 μm. The main molecular features of the spectrum are identified .(image credits: Encrenaz et al. [16])
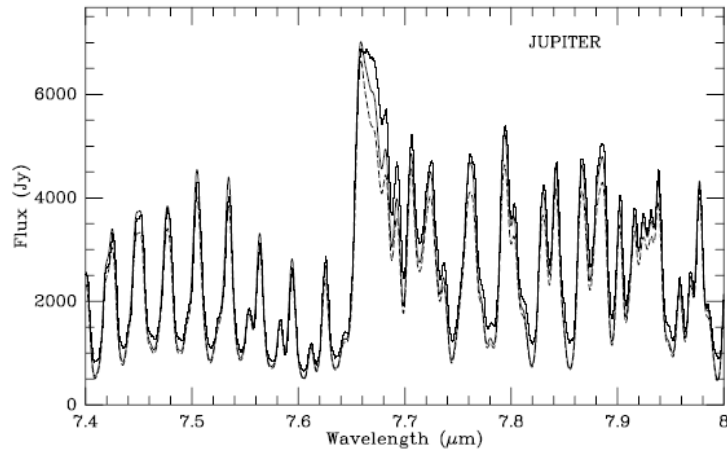
Figure 1.22: Observations by the SWS instrument, onboard ISO, of the methane emission band centered at 7.7 μm. Zoom of Fig. 1.21 around 7.4-8 μm. (image credits: Lellouch et al. [40])
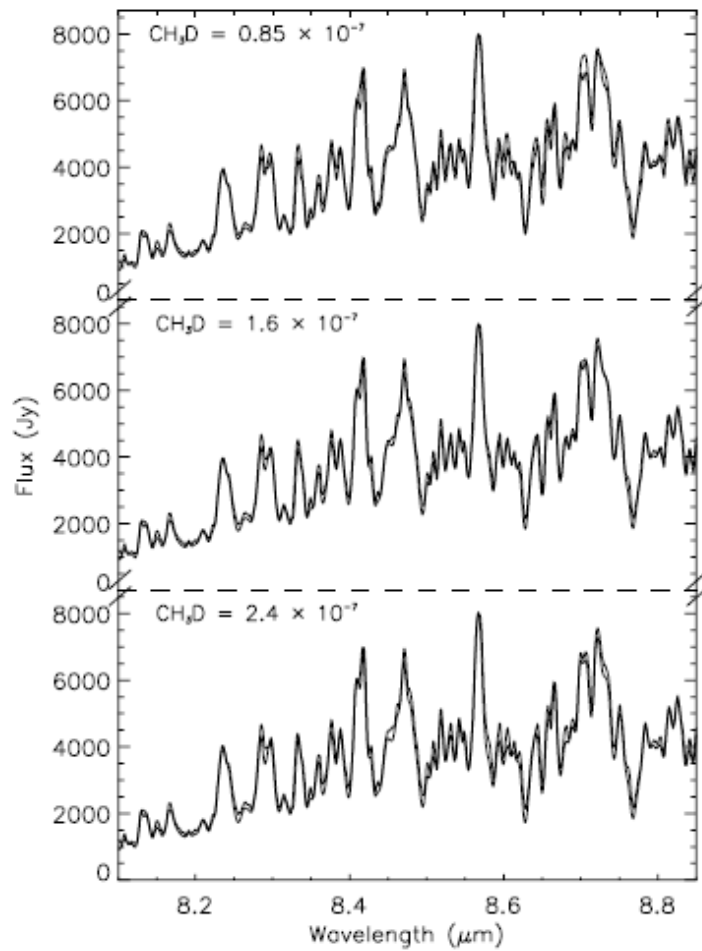
Figure 1.23: Fit of the ISO/SWS spectrum with models with three different abundances of CH_3D (0.85×10^{-7}, 1.65×10^{-7} and 2.45×10^{-7}), at 8.1-8.8 μm. The data is represented by the thick solid line and the model by the thin solid lines. (image credits: Lellouch et al. [40])
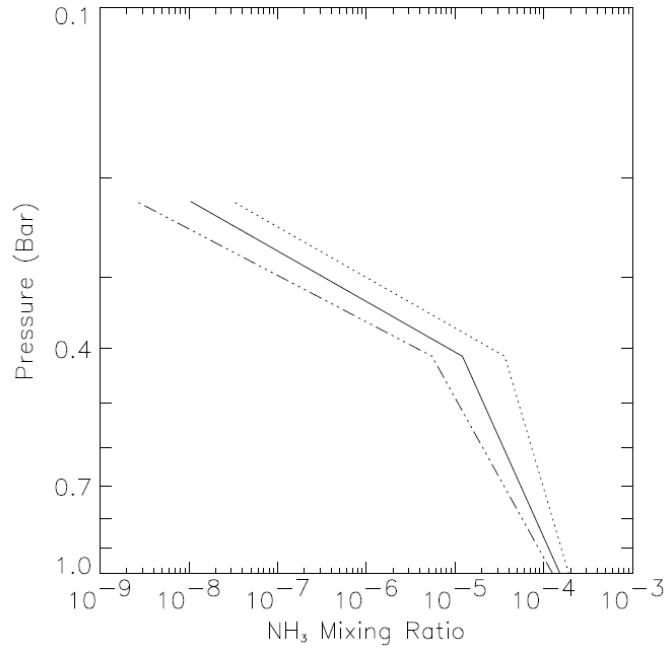
Figure 1.24: Retrieved NH_3 profile from ISO observations, for three different temperature-pressure profiles: Galileu-based profile (solid line), Galileu profile + 2K (dotted line) and Galileu profile - 2K (dashed-dotted line) (image credits: Fouchet [23])

Species	Relative Abundance (VMR)	Region	Reference
CH_4	1.8×10^{-3}	7.4-8 μm, lower stratosphere	Lellouch et al. [40]
CH_3D	1.6×10^{-7}	8.1-8.85 μm, upper troposphere	Lellouch et al. [40]
PH_3	$3 \times 10^{-7} - 7 \times 10^{-6}$	8.1-11.3 μm, upper troposphere, P=150-600 mbar	Lellouch et al. [40]
NH_3	2×10^{-5}	9.5-11.5 μm, upper troposphere, P=500 mbar	Fouchet [23]
	1×10^{-4}	P=800 mbar	

Table 1.6: Retrieved relative abundances (volume mixing ratios) of minor species from Jupiter ISO/SWS observations, derived from several studies.

Chapter 2

Methods and Tools

2.1 Planetary Spectrum Generator

The planetary Spectrum Generator (PSG) (Villanueva et al. [69]) is an online radiative transfer suite for the simulation of the spectrum of planets, exoplanets, comets and other small bodies. The synthesized spectra can cover a broad range of wavelengths, from the radio to the UV. It combines radiative transfer modelling, spectroscopic databases, for example, HITRAN (Gordon et al. [28]), GEISA (Delahaye et al. [9]) and ExoMol (Tennyson et al. [64]), and planetary ephemeris databases (Horizons System - JPL Solar System Dynamics - NASA). The computation of the high-resolution spectra uses line-by-line calculations and for moderate resolutions uses the correlated-k approach.

PSG can be used to do a fit between observations and the modelled spectrum, in order to determinate, for example, the abundance of atmospheric species, the temperature and altitude of the atmospheric level the observations are sounding, the thermal profile and the vertical abundance profile of atmospheric species. Moreover, PSG can help to plan observations, interpret ground-based and space-based data and in the calibration of instrumental effects, such as the instrument's gain issues, offset issues, fringe issues and incomplete stellar subtraction.

PSG can be used in a web-interface, but can also be installed on a personal computer, or run remotely by sending instructions to produce spectra to the online server.

The parameters of the modelled spectrum are defined on a configuration file, the main input file, that can be downloaded from the web-interface or created on the personal computer. The parameters are divided in 3 main fields: atmospheric parameters, object and geometry parameters and instrumental parameters. In the next section I will explain what is defined in each field. To see a complete description of these parameters, see Villanueva et al. [69].

The resulting output of the simulation is a spectrum (the units depend on the simulation), the transmittance of the atmospheric components included in our model atmosphere, in the selected wavelength range, and the noise components of the observations. All these outputs can be downloaded in the web-interface page or downloaded through terminal instructions to the server. An example of output is represented in Fig. 2.1

The main components of PSG are illustrated in Fig. 2.2.
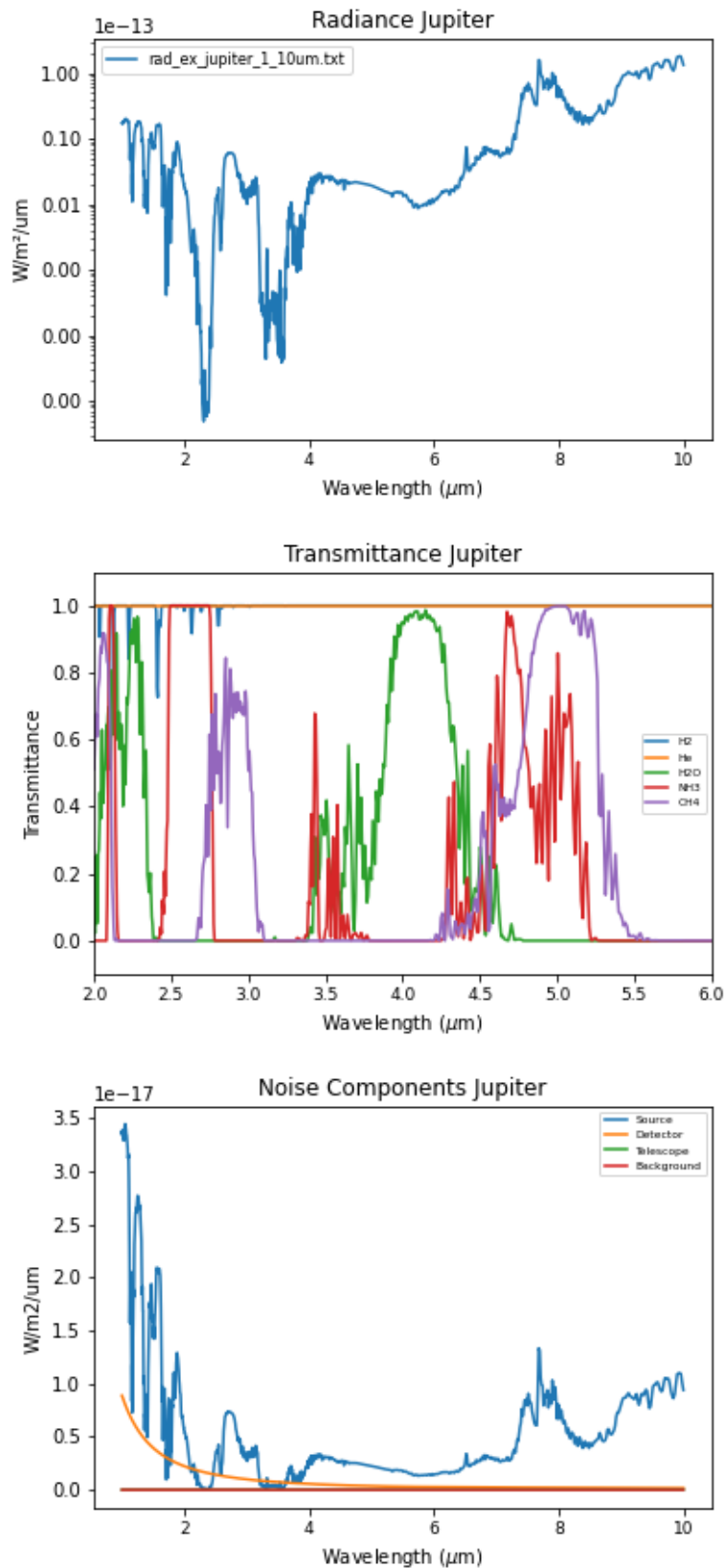
Figure 2.1: Top plot: Radiance spectrum of Jupiter between 1μm and 10μm. **Middle plot:** Transmittance of some atmospheric components of Jupiter. The lower the transmittance the higher the atmospheric absorption by the correspondent component (Blue - H2; Orange - He; Green - H2O; Red - NH3; Purple - CH4). The transmittance spectrum is very important to determine the bands of absorption/emission of the molecules. **Bottom plot:** Main noise components of the simulated spectrum. The photon noise dominates the other components (Blue- Source photon noise; Orange - detector noise; Green - Telescope noise; Red - Background noise).
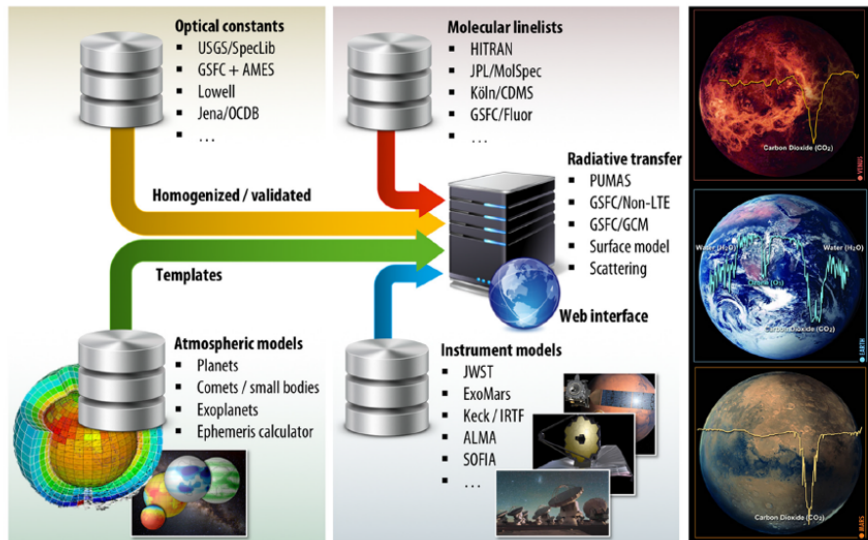
Figure 2.2: The Planetary Spectrum Generator structure. PSG combines radiative transfer models, instrument modelling and planetary databases in an integrated web-interface that generates high-resolution spectra. I will be using the HITRAN database and the PUMAS model (image credits: Villanueva et al. [69])

2.1.1 Object and Geometry

PSG is connected to a 3D orbital calculator for most bodies of the Solar System and confirmed exoplanets. The geometric parameters can influence the observed spectral fluxes, therefore they are pre-calculated in ephemeris tables that provide orbital information with a precision of 1 minute.

Some important geometric parameters are the orbital and spectroscopic velocities of the target (velocity of the target with respect to the star and with respect to the observer), the distance of the target to the observer, the type of host-star of the target, the sub-observer latitude and longitude, the solar longitude and the type of observational geometry. The observational geometry can be of several types: observatory, nadir, solar occultation, stellar occultation, limb, between others (see Fig. 2.3). For a complete description of the object and geometry parameters see Villanueva et al. [69].
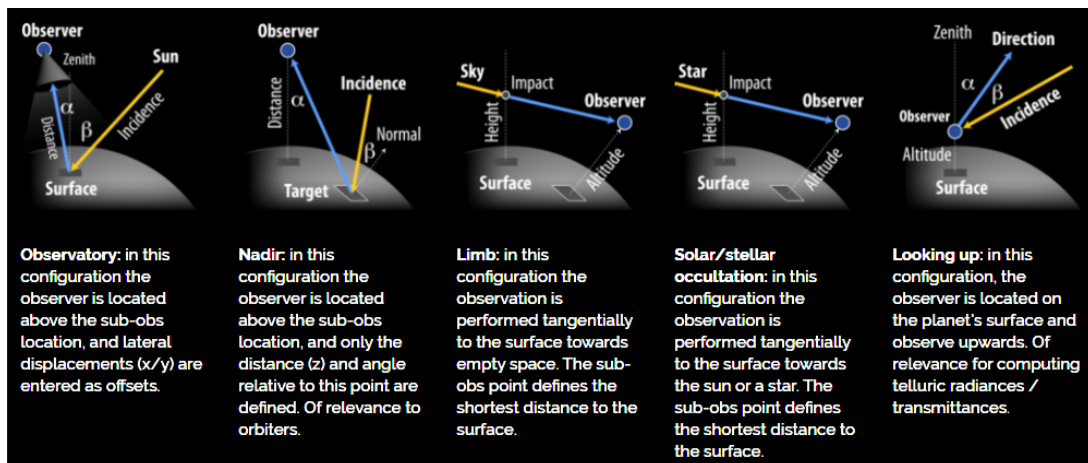
Figure 2.3: Description of some of the types of geometry in PSG (image credits: PSG website)

The accurate measurement of different velocities in high-resolution spectroscopy is very important, as these generates Doppler shifts in the observed spectrum, compared with the rest-spectrum. PSG considers three main velocity parameters: OBJECT-OBS-VELOCITY, OBJECT-STAR VELOCITY and GEOMETRY-ROTATION. A more detailed description of these parameters is in Table 2.1. For the case

of Venus, for which ground-based observations will be simulated in the IR (see Chapter 3), only one velocity component will be important, that is the relative velocity between Earth and Venus (<OBJECT-OBS-VELOCITY>) at the time of observations, with respect to the center of the Earth referential. The rotation velocity contribution from Venus is negligible, given the low rotation velocity of the planet. For Jupiter, for simulated observations in the IR, one velocity component has the greatest contribution, which the rotation velocity of Jupiter (<GEOMETRY-ROTATION>).

Parameter	Description
OBJECT-NAME	Object name
OBJECT-DIAMETER	Diameter of the target (km)
OBJECT-OBS-VELOCITY	Relative velocity between the observer and the target (km s^{-1})
OBJECT-STAR-TEMPERATURE	Temperature of the target host star (K)
GEOMETRY	type of observing geometry
	(Observatory, nadir, limb, stellar occultation, solar occultation, etc)
GEOMETRY-OBS-ANGLE	Angle between observer and planetary surface
GEOMETRY-PHASE	Phase angle between sun and observer
GEOMETRY-ROTATION	Indicates the rotational Doppler shift (km s^{-1})
	and spread of rotational velocities within the FOV

Table 2.1: Description of some object and geometry parameters used by PSG. Adapted from Appendix A of Villanueva et al. [69].
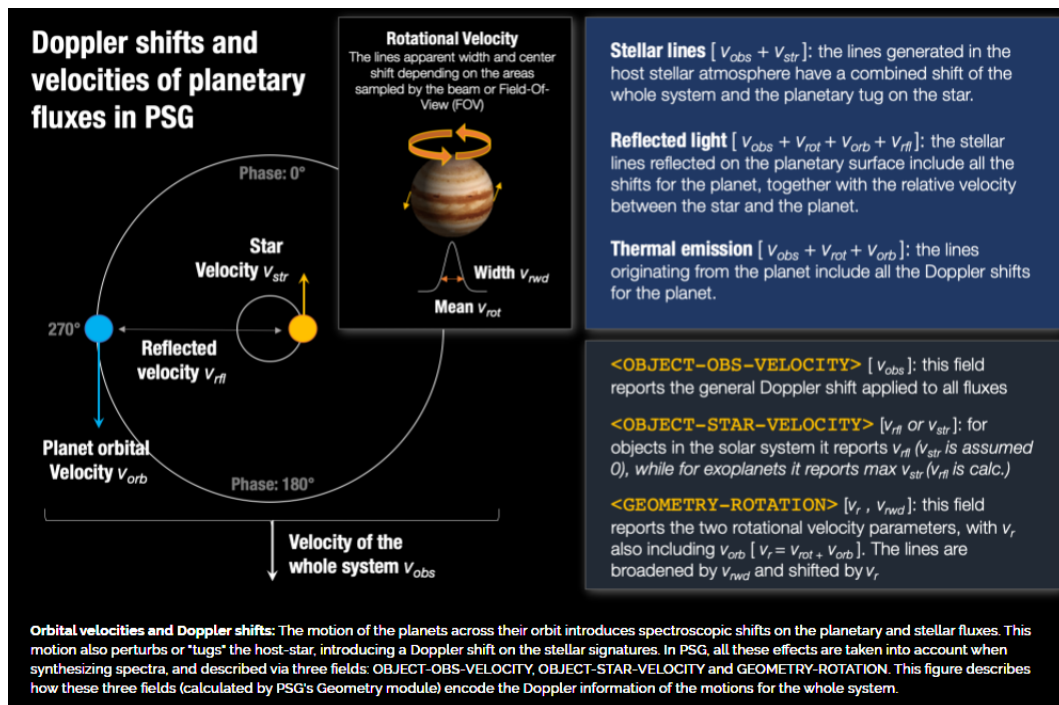
Figure 2.4: Detailed description of the Doppler shift parameters. Three velocity parameters need to be defined for each simulation: <OBJECT-OBS-VELOCITY>, <OBJECT-STAR-VELOCITY>, <GEOMETRY-ROTATION>. (image credits: PSG website)

2.1.2   Atmospheric Model

Once the geometry parameters are defined, the next step is to set as input to the code a certain atmospheric model for our target, which is divided in two main parts: the vertical thermal profile and the vertical mixing ratio of the components of the atmosphere. Several model templates, based on observations and Global Circulation Models, are available on PSG, but the user can also change these existing templates and define its own. For a more detailed description of the atmospheric input parameters see Villanueva et al. [69].

Some atmospheric parameters are described in Table 2.2

Parameter	Description
ATMOSPHERE-STRUCTURE	None/equilibrium: "hydrostatic equilibrium"
	Coma: "Cometary Expanding Coma"
ATMOSPHERE-PRESSURE	Surface pressure for equilibrium atmosphere
ATMOSPHERE-WEIGHT	Molecular weight of the atmosphere (g/mol)
ATMOSPHERE-GAS	Name of the gases to include in the simulation
	(e.g."H2O, CO2, CH4, H2...")
ATMOSPHERE-ABUN	Abundance of gases
ATMOSPHERE-LAYERS	Number of layers of the atmospheric vertical profile
ATMOSPHERE-LAYERS-MOLECULES	Molecules quantified by the vertical profile
ATMOSPHERE-LAYER	Values for the specific layer, Pressure (bar), Temperature (K),
	gases(mol/mol), aerosols(kg/kg)

Table 2.2: Description of some atmospheric parameters used by PSG. Adapted from Appendix A of Villanueva et al. [69].

2.1.3   Instrument modelling

The instrument capability and perfomance can be described by 13 parameters (see Fig.2.5). The main parameters that define the instrument are the mode of operation (e.g. : single telescope, interferometer, coronograph, AOTF+grating and LIDAR system), wavelength range, the spectral resolution, the desired flux unit and the noise characteristics. PSG has a broad database of instrument templates, both for ground-based and space-based instruments, for example, ARIEL, HST, JWST, ALMA, Keck, ExoMars and many more. However, the user may define its own instrument parameters.

For the purposes of this thesis I will be using the single telescope mode. In this mode, the instrument is defined by its collecting area and by its solid angle.

For the case of a ground based telescope, PSG can simulate the telluric absorption affecting the light of the target and the background noise (e.g. zodiacal light, detector, exogenic origin, etc..). The quality of the simulated telluric absorption is very important since the detection of minor species in the atmospheres asks for the modelling and removal of the telluric absorption.

PSG provides the user with a noise calculator for both quantum and thermal detectors.

The main noise components arise from: source photon shot noise, detector (read noise, dark current) noise, telescope noise and background noise.

In the visible ($\sim$ 380 nm-780 nm) and NIR/MIR ($\sim$ 780 nm-15 um), the photon shot noise follows Poisson statistics: photon noise $\sim \sqrt{S}$, where S is the number of photons.

The total signal to noise ratio can be calculated using:

$$SNR = \frac{S}{\sqrt{N_s^2 + N_b^2 + N_d^2 + N_{read}^2}} = \frac{S}{\sqrt{S + MS_b + MS_d + MR_n^2}} \tag{2.1}$$

Where S is the photon counts, S_b is the background counts, S_d is the dark current counts, R_n is the read noise counts and M is the number of pixels contained in the telescope FOV (Field of view).
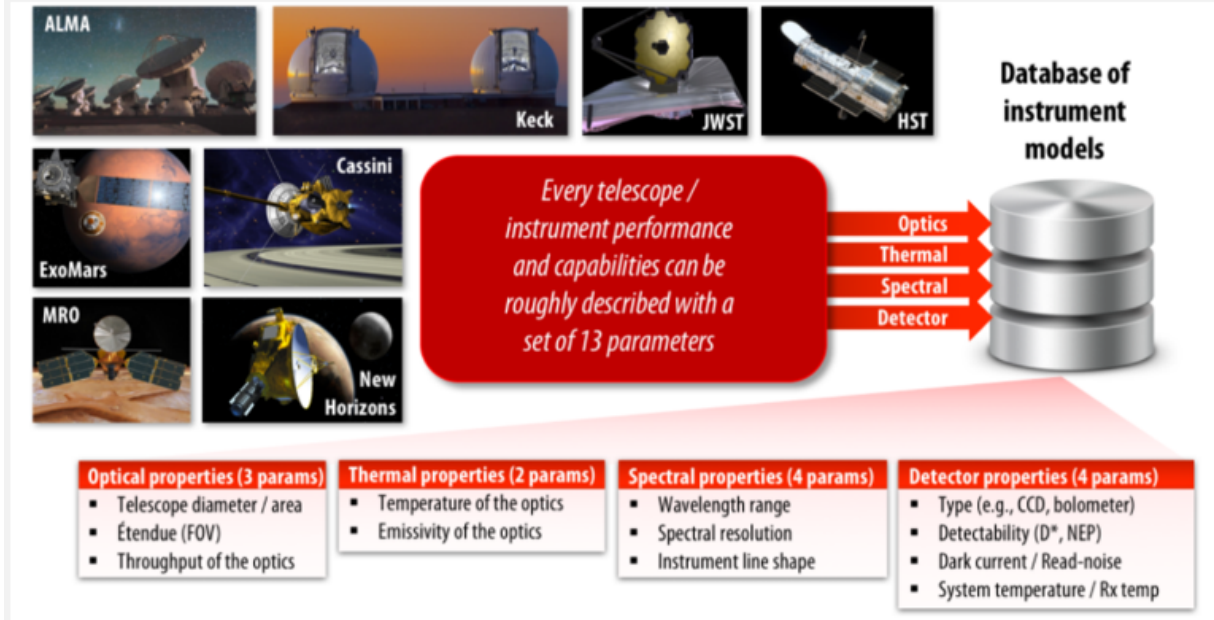
Figure 2.5: Some instrumental modelling parameters used by PSG. For some specific instruments, PSG has a template file with all the parameters already defined. (image credits: PSG website)

2.2 Radiative Transfer

The spectroscopic calculation is divided in three steps in PSG: (1) calculation of the surface reflectance/emissivity and solar spectra; (2) calculation of the atmospheric radiances and transmittances; (3) calculation of the observed fluxes as convolved with the instrument/telescope transfer function. For the second step, for the case of hydrostatic equilibrium atmospheres (e.g. Venus, Mars, Earth), PSG uses a layer-by-layer radiative transfer model named PUMAS (Planetary Universal Model of Atmospheric Scattering).The line-by-line calculations are based on the GENLN2 model (Edwards [14]).In the rest of this section, I describe the calculation of the radiance and transmittance of the simulated spectrum as in Edwards [14].

The specific intensity emitted by the atmosphere of a target object depends on the path the light has travelled until it reaches the observer, on the vertical thermal profile, on the vertical abundance gas profiles and on the transmittance of such atmosphere. A simplified solution to this problem arises from considerations of conservation of energy between the absorbed/scattered and emitted light. Assuming thermodynamical equilibrium, the specific intensity is determined by the Equation of Radiative Transfer (ERT):

$$I_\nu(z_{obs}) = I_\nu(z_s)T_\nu(z_s, z_{obs}) + \int_{z_s}^{z_{obs}} [B_\nu(T(z))k_\nu(z)\rho_a(z)dz]\,T_\nu(z, z_{obs}), \tag{2.2}$$

where $I_v(z_s)$ is the intensity of radiation leaving the planetary surface, $\rho_a(z)$ is the total column density (molecules/cm^2 or kg/cm^2) of the absorbing gas at altitude z, $B_v(T,z)$ is the Planck emission function at temperature T and altitude z, $k_v(z)$ is the total absorption coefficient of all the atmospheric gases at altitude z and $T_v(z_1, z_2)$ is the transmittance between layers z_1 and z_2. We can see that the vertical thermal structure will influence the blackbody emission in each atmospheric layer because $B_v(T(z))$ is a function of T(z). Moreover, the vertical abundance profile ρ_a will determine the amount of absorption/emission in each layer.

The first element of the right-hand side of Eq. 2.2 is the radiation from the surface that is transmitted to the upper part of the atmosphere and the second contribution is the radiation from the emission of all components from all layers that arrive at the cloud top, attenuated by the respective transmittance at each layer. The emission is that of a blackbody weighted by the abundance of the element and the corresponding absorption coefficient (for Local Thermodynamic Equilibrium conditions (LTE)).

The total absorption coefficient is the sum of the absorption coefficient of all the gases in the path, considering that each gas has several lines in the selected wavelength range. It can be calculated using:

$$k_v = \sum_{i,j=1}^{I,J} k_{v,ij} = \sum_{i,j=1}^{I,J} S_{ij} g(v, v_i)_j, \tag{2.3}$$

where S_{ij} represents the line strength (cm^{-1}/(molecules/cm^{-2})) of line i of gas j and $g(v, v_i)_j$ represents the line shape of line i of gas j.

The line shape can have a collisional/lorentzian (Eq. 2.5) or Doppler broadening (Eq.2.4) origin. The collisional broadening happens when the pressure is high and the temperature is low (low/middle atmosphere) and the Doppler broadening happens when the temperature is high and the pressure is low (high atmosphere):

$$k_v = \frac{S_i}{\sqrt{\pi}\gamma_D} exp\left[-\left(\frac{v - v_0}{\gamma_D}\right)^2\right] \tag{2.4}$$

where γ_D is the full width at half maximum of the line (FWHM) and v_0 is the line center

$$k_v = \frac{S_i \gamma_L}{\pi\left[(v - v_0)^2 + \gamma_L^2\right]}, \tag{2.5}$$

where γ_L is the full width at half maximum of the line (FWHM) and v_0 is the line center.

The total transmittance of a mixed path containing J single gas paths over several layers of the atmosphere is:

$$T_v = exp(-\tau_v) = exp\left(-\sum_{j=1}^{J} k_{v,j} u_j\right) \tag{2.6}$$

where τ_v is the optical depth and u_j is the gas amount per cross-sectional area (molecules/cm^{-2})

In the model, the atmosphere is divided in several layers and each layer has an associated temperature T_l. For a layer in LTE conditions, the layer thermal emission can be calculated as:

$$E_{v,l} = B_v(T_l) \sum_{j=1}^{J} k_{v,j} \rho_j \int_{z_{l-}}^{z_{l+}} T_v(z, z_{l+}) dz = B_v(T_l)[1 - T_v] \tag{2.7}$$

where $B_v(T_l)$ is the Planck emission function at wavenumber v and for temperature T_l, where T_l is

the temperature for layer l, where ρ_j is the total column density for gas j, k_v is the absorption coefficient for wavenumber v and gas j and $T_v(z_{zl-})$ is the transmittance between the bottom level of the layer, l-, and the upper level of the layer, l+.

Finally, the specific intensity emitted at the top of the atmosphere is given by iteration for all layers of the atmosphere of the following expression:

$$I_{v,l} = I_{v,l-1} T_{v,l} + E_{v,l} \tag{2.8}$$

where $I_v, l-1$ is the specific intensity at layer l-1, T_v, l is the transmittance at layer l and E_v, l is the thermal emission of layer l.

2.3 HITRAN

In a simulation, I am using the absorption coefficients of the molecular rotational-vibrational transitions given by the HITRAN database. This database can be used independently by accessing the HITRAN website (hitran.org). There, we can select one or more molecules, and some isotopologues if we want, in a specific wavenumber interval, in order to get as an output the list of the transition intensities for the selected molecules, in the selected wavenumber interval.

In Fig. 2.7 we can see some example plots of the transitions intensities for CO2 and PH3. From these type of plots we can identify the main molecular bands by identifying the regions with more transitions and stronger transitions.
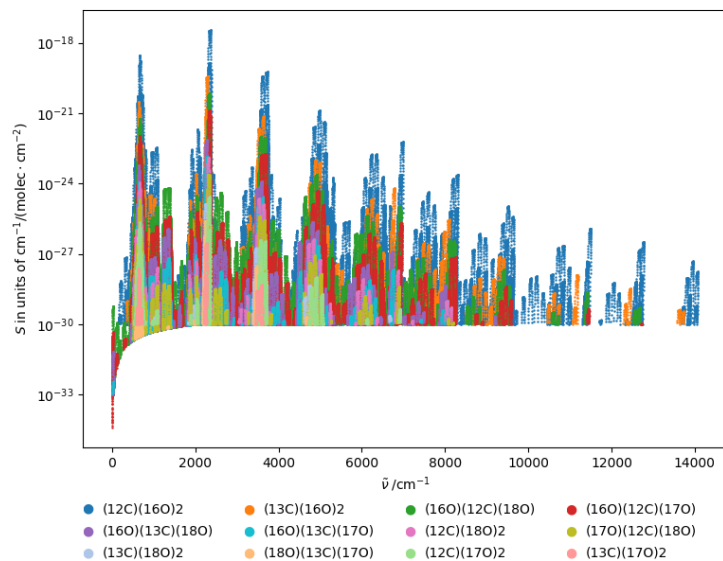
Figure 2.6: Example of HITRAN transition intensities for CO2, between 0 and 14000 cm^{-1},
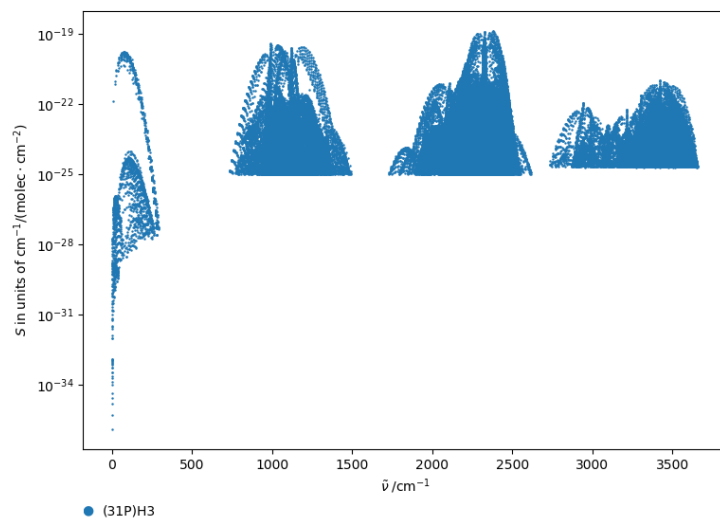
Figure 2.7: Example of HITRAN transition intensities for PH3, between 0 and 3500 cm^{-1}

Chapter 3

Results

3.1 Venus

I simulated observations for two case studies. For Case Study 1, the simulations try to reproduce the data from Encrenaz et al. [17], between 1350 cm^{-1} and 1350.8 cm^{-1} (7.403 μm-7.407 μm), to identify molecular signatures and determine the relative abundance of sulphur dioxide. For Case Study 2, the simulations try to reproduce the observations from Encrenaz et al. [20], to identify molecular features and estimate the relative abundance of phosphine, between 951 cm^{-1} and 956 cm^{-1} (10.467 μm-10.470 μm).

As input for PSG I used two different atmospheric models: VIRA-2 and LMD-VGCM, common both to Case Study 1 and 2, represented in Fig.3.1. The main parameters of the atmospheric models are in Table 3.1. The LMD-VGCM model stands for Laboratoire de Meteorologie Dynamic Venus Global Circulation Model (Gilli et al. [25] and Garate-Lopez and Lebonnois [24]). It is inspired by the GCMs developed for Earth and Mars. It is the only existing ground-to-thermosphere Venus GCM. The simulation of the atmosphere at 90-150 km includes processes such as IR heating by CO_2, IR CO_2 15 μm cooling, extreme UV heating, a photochemical model and others. The simulated thermal structure is consistent with VEx data. The VIRA-2 model stands for Venus International Reference Atmosphere (Zasova et al. [74]). VIRA is an empirical model that relies on data from several missions. From the 1970s and 1980s, such as Venera, Pioneer Venus Orbiter and Magellan probes and most recently Venus Express and Akatsuki.

Parameters	Value
Altitude range	**VIRA-2:** 0-195 km , **LMD-VGCM:** 0-152 km
Wavelength	**Case Study 1:** 7-9 μm, **Case Study 2:** 951-956 cm^{-1} (10.467-10.470 μm)
Molecules included	**VIRA-2:** $CO_2, N_2, CO, O_2, SO_2, H_2O, O_3, HDO, PH_3$ (uniform profile)
	LMD:VGCM: $CO_2, CO, SO_2, H_2O, O_2, O_3, HDO, PH_3$ (uniform profile)
Terrestrial transmittance	**Case Study 1:** applied; **Case Study 2:** applied
Geometry	Observatory, day-side
Observations to simulate	TEXES, IR; **Case Study 1:** Encrenaz et al. [17];
	Case Study 2: Encrenaz et al. [20]

Table 3.1: Description of some of the parameters of the Venus simulations. For more information on the parameters of the simulation, see Chapter 6

The next step was to search in HITRAN for the main molecular rotational-vibrational bands at 7-9
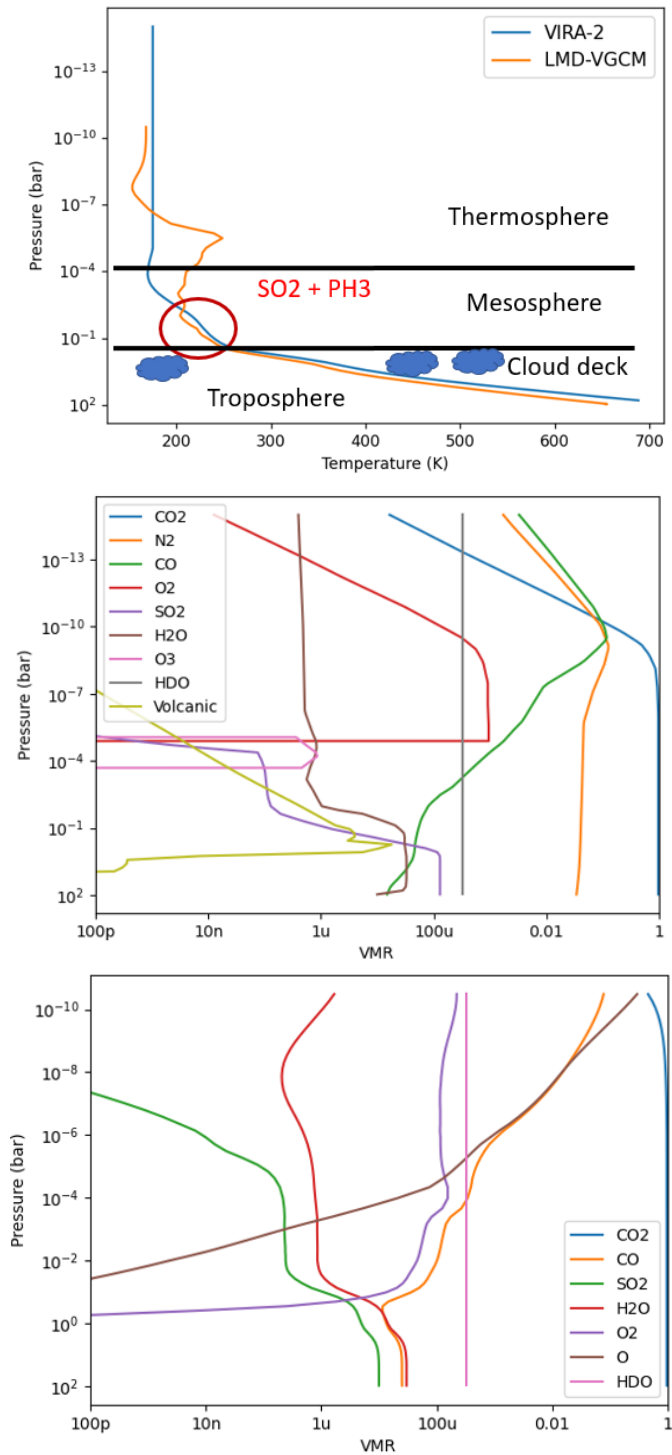
Figure 3.1: Top: Vertical thermal profiles used as input for the Venus simulations. Temperature (K) is in function of pressure (bar). The atmosphere is divided in 3 main layers: Troposphere (0-60 km); Mesosphere (60-100 km); Thermosphere (100km-). At 7-9 μm the region of the atmosphere sounded is around 60-80 km (Encrenaz et al. [17]). The red circle highlights the pressure range where differences in the temperature-pressure profiles will matter (see chapter 4). **Middle:** Vertical Mixing Ratios (molecule/molecule) corresponding to the VIRA-2 model ($CO_2, N_2, CO, O_2, SO_2, H_2O, O_3, PH_3$) as a function of pressure (bar). **Bottom:** Vertical Mixing Ratios (molecule/molecule) corresponding to the LMD-VGCM model ($CO_2, CO, SO_2, H_2O, O_2, O, PH_3$) as a function of pressure (bar). For PH_3, several uniform vertical profiles will be used in the simulations. A uniform 0.1 ppm HDO profile was defined for both models

μm for SO_2, CO_2 and H_2O. The main molecular bands are summarized in Table.6.1 and can be visualized in Fig. 6.1 (see Chapter 6).

I proceeded then to the search for the molecular bands in the simulations. These can be observed in Fig. 3.2.

Fixing all the parameters, I varied the abundance of SO_2, CO_2 and H_2O in order to identify the main absorption bands between 7-9 μm, fixing all other parameters of the model. With this qualitative approach I could identify the same bands as the ones of HITRAN (Table 6.1).

In the top panel of Fig. 3.2, from the blue line (reference spectrum) to the green line, the abundance of CO_2 is divided tenfold for each line in relation to a standard abundance used in the reference spectrum. The resulting effect is an increase in the resulting radiance. In other words, when the abundance of CO_2 is decreased in the model, the absorption of this species also decreases.

In the middle panel of Fig. 3.2, an increase of the abundance of water by 10 (orange line) and by 100 (green line), in relation to a standard abundance (blue line) does not produce a significant change in the simulated radiance. Therefore, I will neglect, in first approximation, the existence of water lines at 7-9 μm.

In the bottom panel of Fig. 3.2, I multiplied the abundance of SO_2 in the reference spectrum, in blue, by ten-fold (orange spectrum) and by one hundred-fold (green spectrum). I identified two main absorption bands, in agreement with the ones from HITRAN (Table 6.1).

3.1.1 Sulphur dioxide

To identify individual SO_2, CO_2 and HDO lines (Case Study 1), I increased the spectral resolution of the reference spectrum to R$\sim$80000 and did a zoom around 7.4 μm. Again, I varied the abundance of the latter species in the model to search for individual lines (see Fig. 3.3). The spectra are Doppler shifted by +0.045 cm^{-1}, corresponding to a relative velocity between Earth and Venus of about -10 km s^{-1}.

To check if the detected lines in the simulation were true detections, I did a comparison between the position of the center of the lines in the simulations, corrected for the Doppler shift due to the relative velocity between Earth and Venus, with the positions extracted from HITRAN (Table.3.2). The value of the relative velocity between the two bodies was, for the time of the observations, ΔV=-10.127 km s^{-1}. The negative value indicates Venus was approaching Earth, generating a blue-shift in the observed spectrum. The relation between the corrected and the non-corrected line center is given by:

$$\nu_0 = \nu \times (1 - \frac{\Delta V}{c}), \tag{3.1}$$

where ν_0 is the rest-frame corrected wavenumber, ν is the observed wavenumber and c is the speed of light, with c=299792458 m s^{-1}

The line identification is clear on Fig.3.4, together with the comparison of the two simulations with data.

The determination of the abundance of SO_2 was done using two methods, the retrieval and the line depth ratio. The line depth ratio method (ldr) consists in measuring the line depth ratio between a weak SO_2 line and a strong CO_2 line (highlighted in Fig.3.5), for various abundances of SO_2. If this variation is linear, then comparing with the SO_2/CO_2 line ratio of the observations we can infer the abundance of SO_2. The value of the SO_2/CO_2 ratio of the observations is about 0.25. Inserting this value in the relations derived in Fig. 3.6, we can infer the abundance of SO_2. The retrieval works through the use of a retrieval module included in PSG and it adjusts the entire SO_2 vertical profile to obtain a best match to observations.
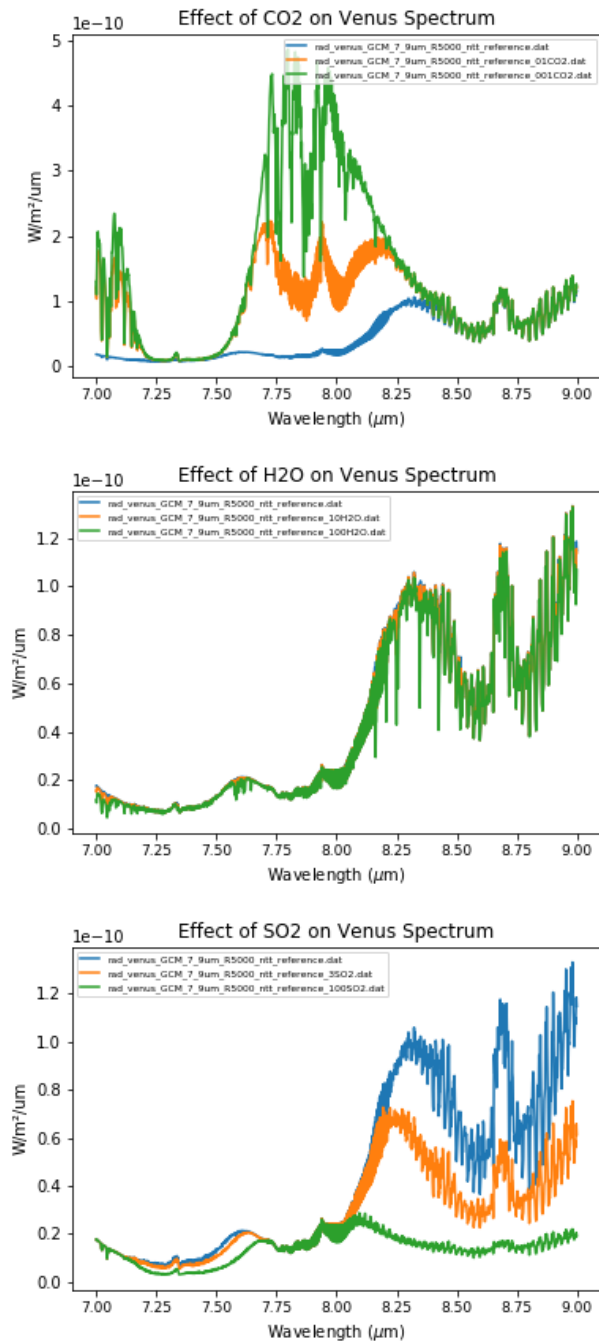
Figure 3.2: Exploration of the effect on the Venusian spectrum of the variation of the abundance of CO_2, H_2O and CO_2, for R=5000, between 7 μm and 9 μm. **Top plot:** Blue line (CO_2=1 (standard abundance, represented by a scalar)), Green line (CO_2=0.01), Orange line (CO_2=0.1). The abundance of CO_2 increases ten-fold, for each line, from the green line to the blue line, resulting in the decrease of the resulting radiance. This is due to CO_2 absorption. **Middle plot:** Three different lines represent different abundances of H_2O in the model: blue - H_2O = 1 (standard abundance); Orange - H_2O = 10; Green: H_2O = 100. No significant difference in the resulting radiation is noticeable at the current resolution. **Bottom plot:** The increase of the abundance of SO_2 in the model from the blue line to the green line decreases the resulting radiance, due to increased SO_2 absorption. Blue : SO_2 = 1 (standard abundance); Orange : SO_2= 10; Green: SO_2=100.
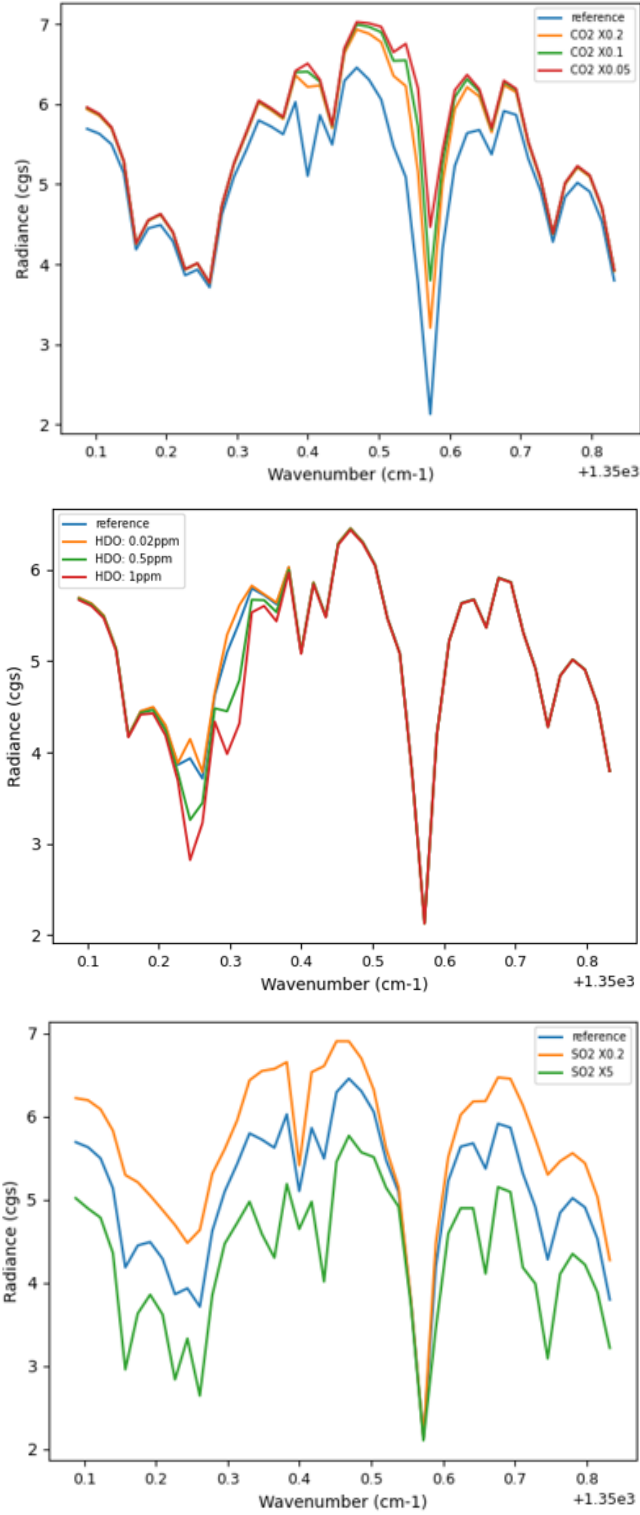
Figure 3.3: Exploration of the effect on the Venusian spectrum of the variation of the abundance of CO_2, HDO and SO_2 of the model, at 1350.0 and 1350.8 cm^{-1}, for R=80000. **Top plot:** A decrease in the abundance of CO_2 in the model results in a decrease of the resulting radiance; **Middle plot:** An increase in the abundance of HDO in the model results in an increase of the depth of two lines. This suggests these lines have a contribution from HDO absorption; **Bottom plot:** An increase in the abundance of SO_2 in the model results in the decrease of the resulting radiance and of the depth of some lines, which suggests those are SO_2 lines. See Table 3.2 for a list of the lines

37
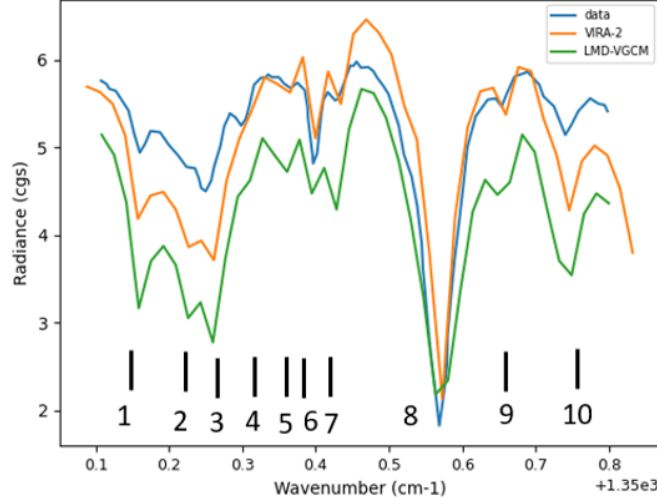
Figure 3.4: Comparison between simulations and TEXES SO_2 data (Encrenaz et al. [17]). Two simulations are compared to data. The VIRA-2 model has a higher radiance than the LMD-VGCM model simulation and weaker and less broad SO_2 lines compared with the LMD-VGCM model. The absorption lines have been numbered are can be consulted on the Table 3.2; cgs units= erg s^{-1} cm^{-2} sr^{-1} $(cm^{-1})^{-1}$; VIRA-2 model: Zasova et al. [74]; LMD-VGCM model: Gilli et al. [25] and Garate-Lopez and Lebonnois [24]

Line (cm^{-1})	PSG	PSG Doppler corrected	HITRAN
1	1350.159 ± 0.009	1350.113 ± 0.009	SO_2 - 1350.113
2	1350.226 ± 0.009	1350.180 ± 0.009	SO_2 - 1350.179
3	1350.260 ± 0.009	1350.214 ± 0.009	SO_2 - 1350.214
4	1350.310 ± 0.009	1350.264 ± 0.009	HDO - 1350.259
5	1350.361 ± 0.009	1350.315 ± 0.009	SO_2 - 1350.315
6	1350.395 ± 0.009	1350.349 ± 0.009	SO_2 - 1350.352 CO_2 - 1350.347
7	1350.429 ± 0.009	1350.383 ± 0.009	SO_2 - 1350.385
8	1350.564 ± 0.009	1350.518 ± 0.009	CO_2 - 1350.525 CO_2 - 1350.510
9	1350.648 ± 0.009	1350.602 ± 0.009	SO_2 - 1350.602
10	1350.732 ± 0.009	1350.686 ± 0.009	SO_2 - 1350.687

Table 3.2: Sulphur Dioxide on Venus - Line Identification: 1350-1350.8 cm^{-1}. In general, the position of the lines is in agreement with the values from HITRAN, except for line 6. For this cases, there is more than one correspondence. One possibility that is being evaluated is insufficient resolution to distinguish between the two possible lines. The uncertainty of the line positions derive from the resolution of the simulation (~ 0.017 cm^{-1})

The result of the retrieval is on Fig.3.7. The VIRA-2 model seems to present a better fit to data than the LMD-VGCM model, because it models better the depth and width of the strong CO_2 line, at 1350.6 cm^{-1}, and also of the SO_2 lines and telluric water absorption at 1350.1-1350.3 cm^{-1}. For the entire wavenumber interval, VIRA-2 model has $\chi^2(red) \sim 6$, while the LMD-VGCM model has $\chi^2(red) \sim 1$. However, when excluding wavenumbers >1350.7 cm^{-1}, the VIRA-2 model has the lower $\chi^2(red)$. The
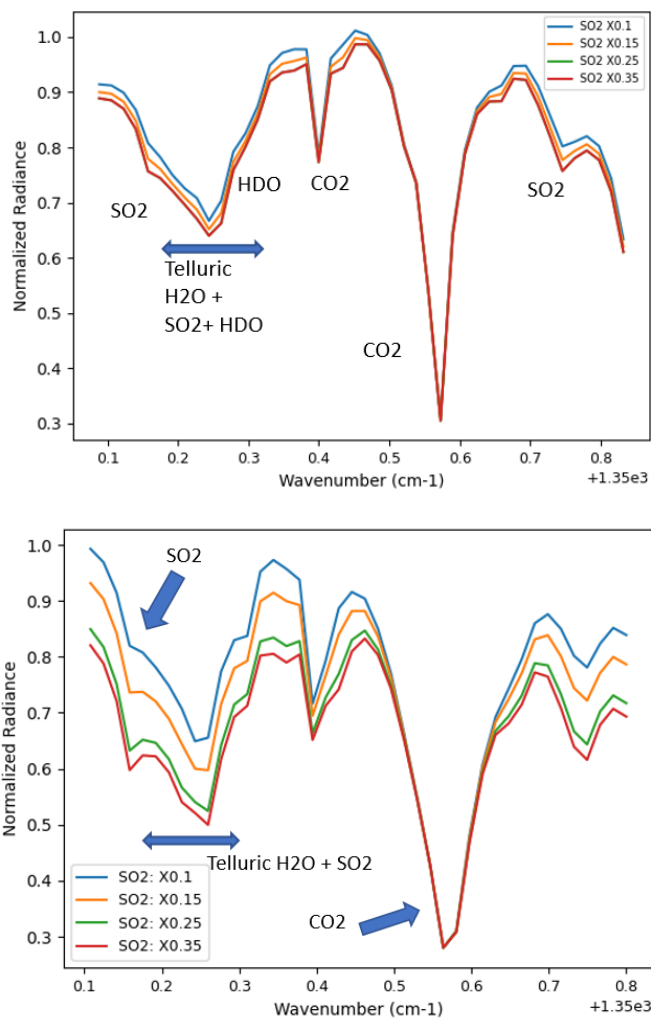
Figure 3.5: Effect of the variation of SO_2 abundance in the resulting radiance - ldr method on Venus. Small variations of the abundance of SO_2 were used, since the depth of the corresponding lines are sensitive to small variations **Top** VIRA-2 model. 4 different abundances of SO_2 were used, represented by a different scaling factor (For example, $SO_2 = \times 0.1$, corresponds to a model where the standard abundance of SO_2 in VIRA-2 was multiplied by 0.1), and a relation was established between the ldr(SO_2/CO_2) and the abundance of SO_2. **Bottom**: LMD-VGCM model. 4 different abundances of SO_2 were used and a relation was established between the ldr(SO_2/CO_2) and the abundance of SO_2. (see Fig. 3.6)

weak CO_2 line, at 1350.4 cm^{-1}, and adjacent SO_2 lines (1350.36 cm^{-1} and 1350.564 cm^{-1}) suggest that improvements in the model are needed (see Chapter 4 for further discussion).

The estimated abundances obtained for SO_2 are in the Table 3.3.

Model/Methods	ldr(SO_2/CO_2)	retrieval
VIRA-2	100-154 ppb	109-118 ppb
LMD-VGCM	20-43 ppb	83-100 ppb
Observations (Encrenaz et al. [17])	50-175 ppb	

Table 3.3: Estimated abundance of SO_2, for a combination of different models and methods. The lower value of the VIRA-2 model using the line depth ratio method corresponds to a situation where the abundance of SO_2 is derived without including telluric absorption in the simulation. The range of abundance of SO_2 derived from observations comes from spatial and temporal variability. For more details on the estimated abundances and sources of the errors, see Chapter 4.
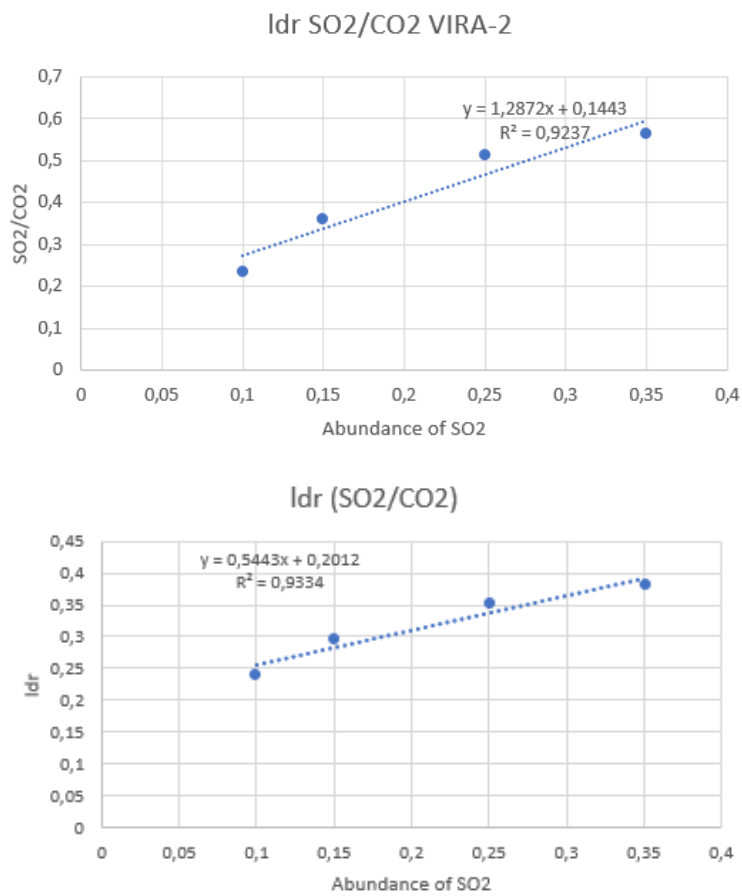
Figure 3.6: Demonstration of the linear relation between ldr(SO_2/CO_2) and the abundance of SO_2, represented by a scalar. In the paper, $SO_2/CO_2 \sim 0.25$. Inserting this value in the equations derives an estimation of the abundance of SO_2; **Top plot:** VIRA-2 simulation; **Bottom plot:** LMD-VGCM simulation
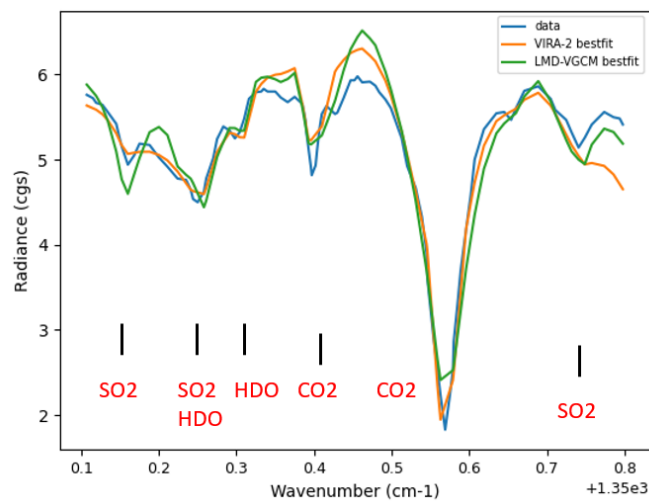
Figure 3.7: Bestfits obtained for TEXES data. The VIRA-2 model provides the simulation with the best match to data. The line positions identified corresponds to those of HITRAN (see Table. 3.2) and matches the identification made by Encrenaz et al. [17]

3.1.2 Phosphine

To identify PH_3 lines (Case Study 2), I did the simulations in Fig.3.8, with a resolution of R=80000, between 955.15 cm^{-1} and 955.4 cm^{-1}, in order to reproduce observations by Encrenaz et al. [20]. I applied telluric transmittance, in this case only due to telluric water lines. The spectrum is Doppler shifted by about +0.035 cm^{-1}, corresponding to a relative velocity between Venus and Earth at the time of the observations of about -11 km s^{-1}. I did simulations for different phosphine abundances: 5 ppb, 7 ppb and 10 ppb (see Fig.3.8). Its very difficult to spot the phosphine absorption line at 955.26 cm^{-1} due to a strong telluric water band at 955.2-955.3 cm^{-1}.
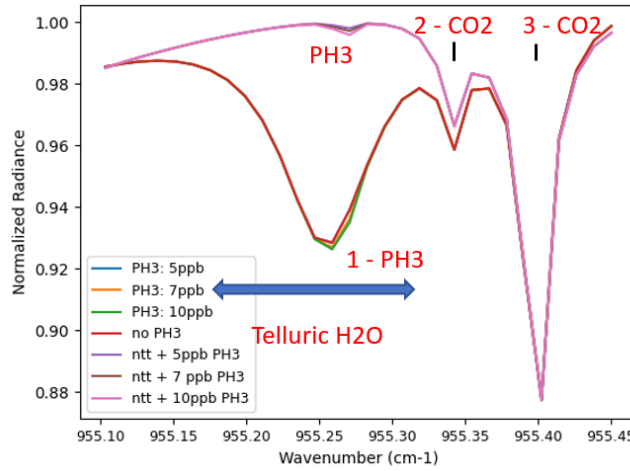
Figure 3.8: Exploration of the effect on the Venusian spectrum of the variation of the abundance of PH_3, between 955.15 cm^{-1} (10.467 μm) and 955.4 cm^{-1} (10.467 μm), for R=80000. The simulations were normalized by the maximum value of radiance in each simulation, as a first approximation (for more information, see Chapter 4). Telluric water absorption dominates the region of the spectrum were the phosphine absorption line should be present, namely at 955.15-955.35 cm^{-1}. The simulations include 3 different phosphine abundances: 5 ppb, 7 ppb and 10 ppb, for two different situations: including telluric absorption and removing telluric absorption (ntt). Without telluric absorption it is much easier to identify the phosphine absorption line than when including telluric absorption. Absorption lines are numbered (see Table 3.4)

Line (cm^{-1})	PSG	PSG Doppler corrected	HITRAN
1	955.271 ± 0.006	955.237 ± 0.006	PH_3 - 955.233
2	955.343 ± 0.006	955.308 ± 0.006	CO_2 - 955.307
3	955.403 ± 0.006	955.369 ± 0.006	CO_2 - 955.369

Table 3.4: Phosphine on Venus - Line Identification: 955.15-955.4 cm^{-1}. See Fig.3.8. Line 1 is a telluric water line. The position of the lines is in agreement with the positions reported in HITRAN (Gordon et al. [28]). The uncertainty of the line positions derive from the resolution of the simulation ($\sim 0.012 \ cm^{-1}$)

I identified the absorption lines in the spectrum and compared them with the transition positions from HITRAN (Table 3.4).

The next step was to do a calibration of the TEXES data from observations. The first step of this calibration was to plot a calibrated spectrum, with cgs units (erg $s^{-1} \ cm^{-2} \ sr^{-1} \ (cm^{-1})^{-1}$) and also with normalized units. This calibration dataset was plotted together with the TEXES uncalibrated data, such that a correspondence between TEXES normalized data and absolute units was done (see Fig. 6.2). The calibrated data points were selected using a dedicated software like Origin/Grapher and later an interpolation was done such that I could plot the calibrated data points.
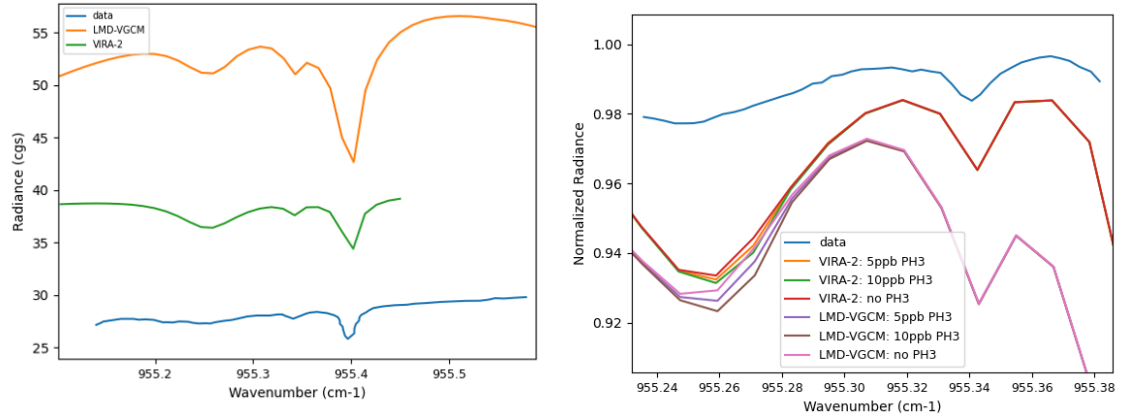
Figure 3.9: Left plot: Comparison between simulation and observations (blue) by Encrenaz et al. [20], using the VIRA-2 model (green) (Zasova et al. [74]) and the LMD-VGCM model (orange) (Gilli et al. [25] and Garate-Lopez and Lebonnois [24]) as inputs for PSG. The LMD-VGCM model presents the higher values of radiance. Moreover, it has deeper and broader CO_2 lines than the VIRA-2 model and data. Both simulations have broader and deeper CO_2 lines than the data, as well as stronger water absorption at around 955.2-955.3 cm^{-1}. These issues are addressed in Chapter 4. cgs units= erg s^{-1} cm^{-2} sr^{-1} $(cm^{-1})^{-1}$; **Right plot:** Zoom of the left plot at about 955.24-955.38 cm^{-1} in normalized radiance units. The effect of different abundances of phosphine, 5 ppb and 10 ppb, in the simulations are shown. The water absorption, at about 955.25 cm^{-1}, is about 4 % and 5 % deeper than the water absorption of the data for, respectively, the VIRA-2 model and the LMD-VGCM model.

In Fig. 3.9, there is a comparison between the simulations and data. There is s discrepancy of a maximum of a factor of 2 between data and simulations.

The best fit is achieved by the VIRA-2 model, with $\chi^2(red) \sim 0.1$, compared with $\chi^2(red) \sim 0.6$ for the LMD-VGCM model. The CO_2 lines have a good fit in general as well as the telluric transmission (see Fig.3.10). Possible improvements to these fits are described in Chapter 4.

The PH_3 absorption line cannot be detected either in the simulation or in the observations. This is due to the strong telluric water absorption. If we remove the telluric absorption, the PH_3 line can be detected.
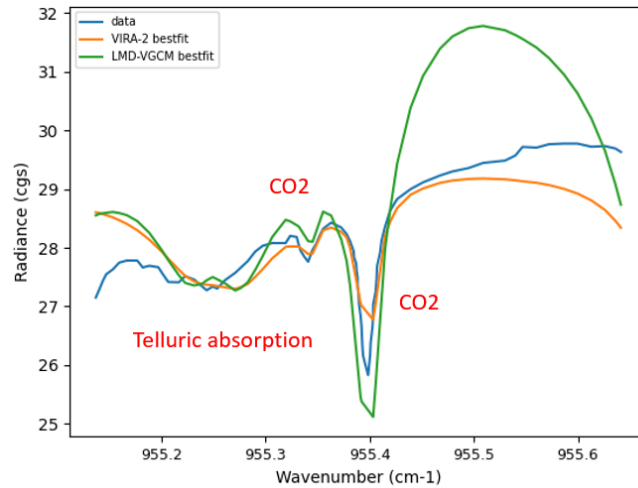
Figure 3.10: Bestfits between models and observations by Encrenaz et al. [17]. Green - LMD-VGCM fit; Orange - VIRA-2 fit. The main absorption features are identified. The CO_2 lines are best fitted by the VIRA-2 model, since the $\chi^2(red)$ is lower than for the LMD-VGCM model. Bellow 955.2 cm^{-1} and above 955.4 cm^{-1} the simulations deviate from the data. A discussion of these features can be found at Chapter 4.

3.1.3 Determination of the D/H ratio

I simulated observations from the Venus night-side from de Bergh et al. [7], at 2.34-2.43 μm (4115-4274 cm^{-1}), done with the Canada-Hawai-France Telescope (CHFT), with a resolution of about 0.23 cm^{-1}, with corrected terrestrial absorption (see Fig. 3.11). I used uniform HDO vertical profiles. The model used as input was the VIRA-2 model (Zasova et al. [74]).
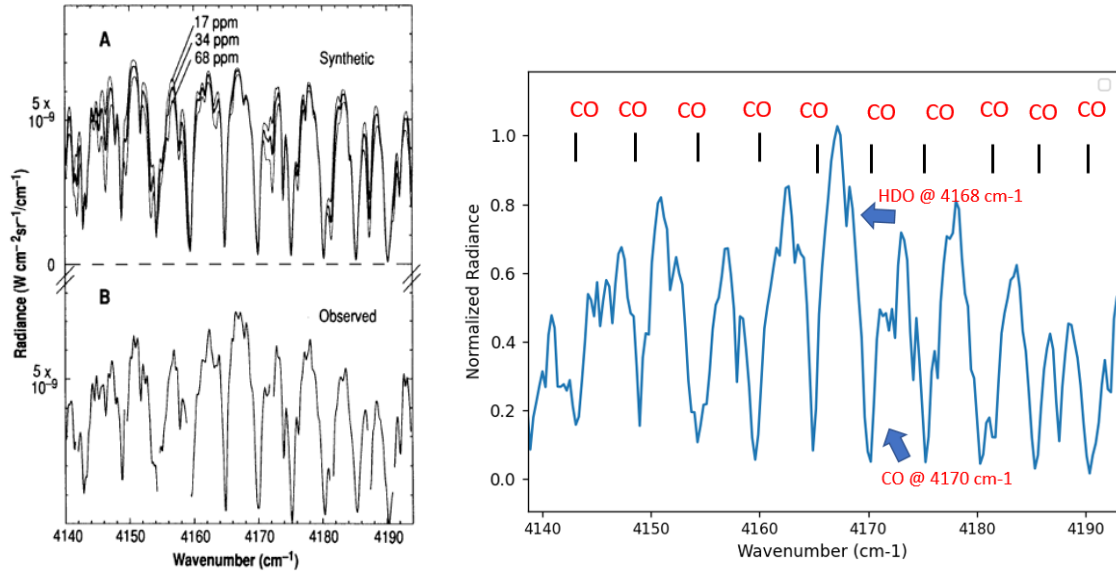
Figure 3.11: Comparison between simulation and data (de Bergh et al. [7]), at around 4140-4190 cm^{-1}. ($\sim 2.39 - 2.42\mu m$) - D/H ratio on Venus. **Left:** Observations by de Bergh et al. [7] in units of radiance. The top plot represents simulations with different abundances of H_2O to fit the observed data (bottom plot). **Right plot:** PSG simulation using the VIRA-2 model. CO dominates this region of the NIR spectrum of Venus. Several lines were identified. The position of the lines is in agreement with the ones from HITRAN. The lines used to estimate the D/H ratio are indicated by the blue arrows: HDO at around 4168 cm^{-1} and CO at aroud 4170 cm^{-1}.
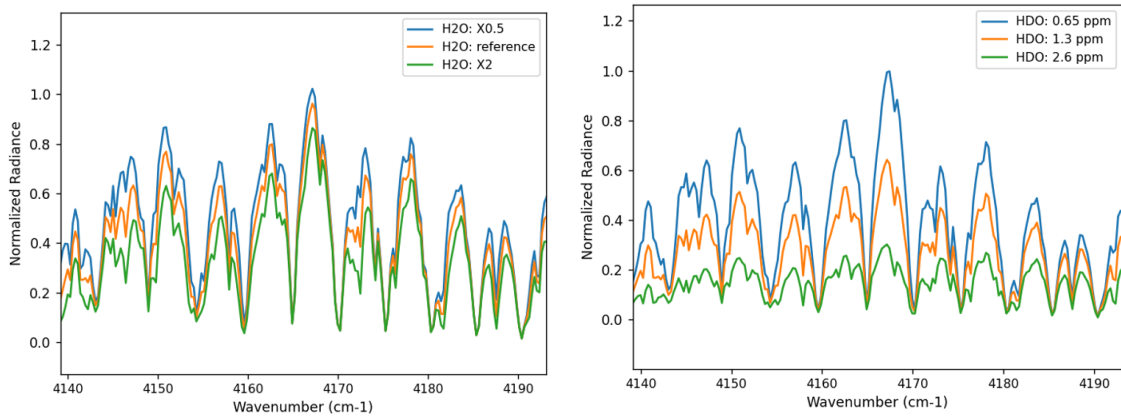
Figure 3.12: Identification of H_2O and HDO lines: Venus. **Left plot:** Effect of the variation of the abundance of H_2O in the resulting radiance, here presented in normalized units. The normalization factor used was the highest value of the radiance, that corresponds to a wavenumber of about 4170 cm^{-1}. Three different abundances of water were simulated: H_2O= 1 (reference standard abundance of the VIRA-2 model), $H_2O = \times 0.5$, H_2O= $\times$ 2. The depth of some lines increases with increasing abundance, suggesting that those may be water lines. **Right plot:** Effect of the abundance of HDO in the resulting normalized radiance. Three abundances of HDO were used: 0.65 ppm, 1.3 ppm and 2.6 ppm. The depth of some lines is very sensitive to variations of the abundance of HDO. This suggests those are HDO lines and are stronger than H_2O lines seen in the upper plot.

The strong lines correspond to CO lines, that dominate this part of the Venus spectrum. The weaker lines are mainly due to HDO absorption, since it can be seen that the depth of these lines increases faster for the same multiplicative factors as for the case of H_2O (see Fig.3.12). These weaker HDO lines will

nevertheless have a small contribution from H_2O absorption.

To determine the D/H ratio, I used the line depth ratio method (for more details see Section 3.1.1), applied for the HDO weak line at 4168 cm^{-1} and for the strong CO line at 4170 cm^{-1} to estimate the abundance of HDO (lines identified in Fig. 3.11). The abundance of H_2O was assumed to be that of the model (VIRA-2), since the corresponding abundance (33 ppm) is similar to the one derived from de Bergh et al. [7] (34 ppm). I could not identify a unique H_2O line which was not contaminated by a HDO line. Otherwise, I would have applied the same line depth ratio method to derive the H_2O abundance.

I then measured the depth of the HDO line, using 5 different abundances, namely 0.65 ppm, 1 ppm, 1.3 ppm, 2 ppm and 2.6 ppm (see Fig. 3.13).
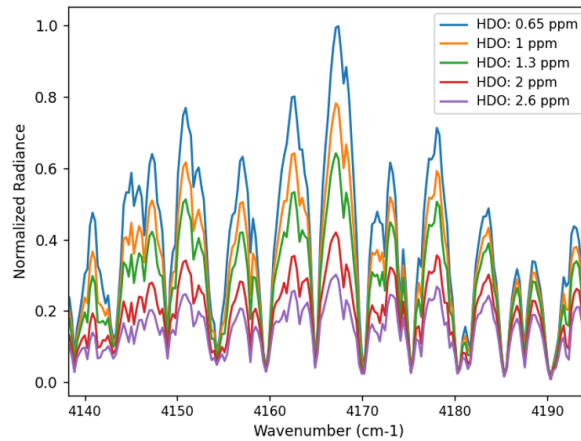
Figure 3.13: Effect of different HDO abundances on the depth of HDO lines: HDO=0.65 ppm (blue), 1 ppm (orange), 1.3 ppm (green), 2 ppm (red), 2.6 ppm (purple).

Next, the ldr(HDO/CO) was calculated and a linear relation was derived between the abundance of HDO and the ldr(HDO/CO).
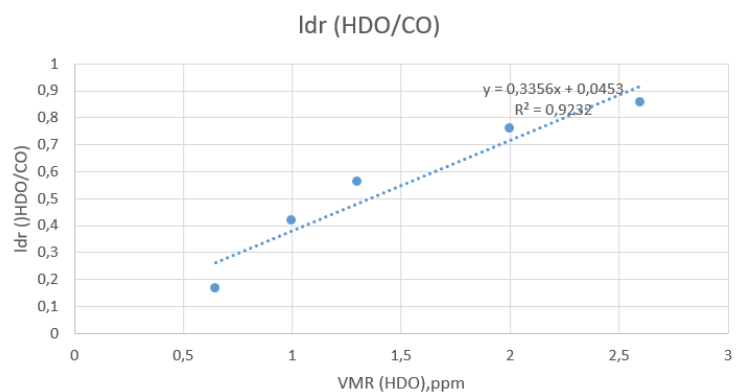
Figure 3.14: Relation between abundance of HDO and the ldr(HDO/CO). The relation can be represented by a linear equation. Five different abundances of HDO were used

Using the derived expression, I could estimated the HDO abundance given the ldr(HDO/CO) of the observations. The estimated abundance of HDO was 0.3 ppm.

Finally, I computed the D/H ratio, in the following manner: D/H = 0.5 $\frac{HDO}{H_2O}$ = 0.5 $\frac{0.3 \times 10^{-6}}{33 \times 10^{-6}}$ ∼ 4.6 $\times 10^{-3}$ ∼ 29 D/H (Earth) , to compare with D/H = 80-160 D/H (Earth) (de Bergh et al. [7]). Note that D/H (Earth) ∼ 1.56 $\times 10^{-4}$. There is a discrepancy between the estimated value and the one from the literature. This will be addressed in Chapter 4.

3.2 Mars

3.2.1 Methane

The goal is to simulate both a positive and negative detection of methane on Mars. The positive detection is the one done by the PFS instrument on Mars Express (MEx) (Giuranna et al. [26]). The negative detection follows from the ExoMars NOMAD/ACS TGO instruments (Korablev et al. [35]).

Parameters	Value
Altitude range	0-260 km
Surface Pressure	6.5 mbar
Surface Temperature	275 K
Wavelength	3.1-3.6 μm (2778-3226 cm^{-1})
Molecules included	$CO_2, N_2, O_2, CO, H_2O, O_3, CH_4$ (0-30 km, uniform profile), Dust, Water-ice
Terrestrial transmittance	removed
Geometry	Observatory, day-side, jan 2021
Observations to simulate	Planetary Fourier Spectrometer (PFS), Mars Express, IR Giuranna et al. [26]

Table 3.5: Atmospheric Parameters - Mars. Description of some of the parameters of the simulations
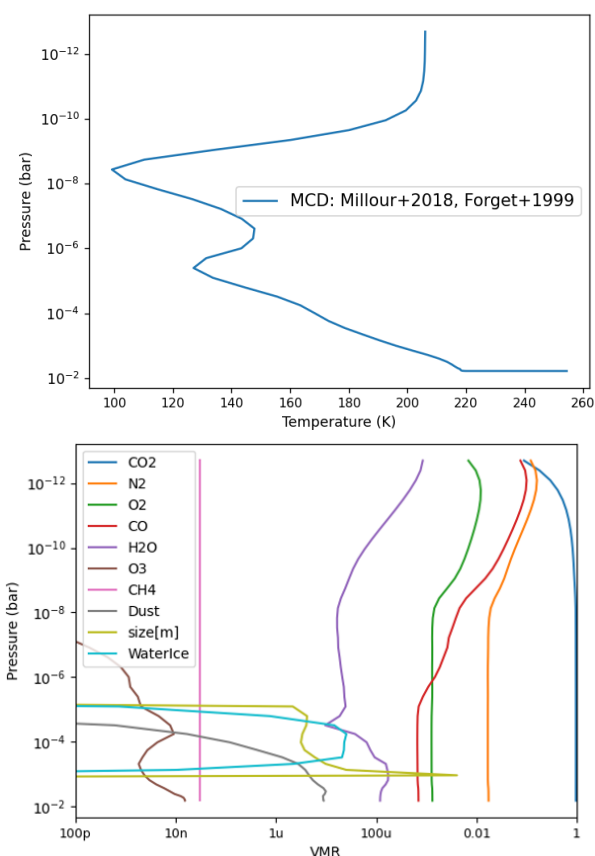
Figure 3.15: Top plot: Vertical thermal profile of the Martian atmosphere. Pressure (bar) as a function of temperature (K). **Bottom plot:** Vertical Mixing Ratio (molecule/molecule) of the main martian atmospheric components ($CO_2, N_2, O_2, CO, H_2O, O_3, CH_4$, Dust, waterice) as a function of pressure. Note that CH_4 was assumed to have an uniform profile of 18 ppb. From Millour et al. [46],Forget et al. [22].
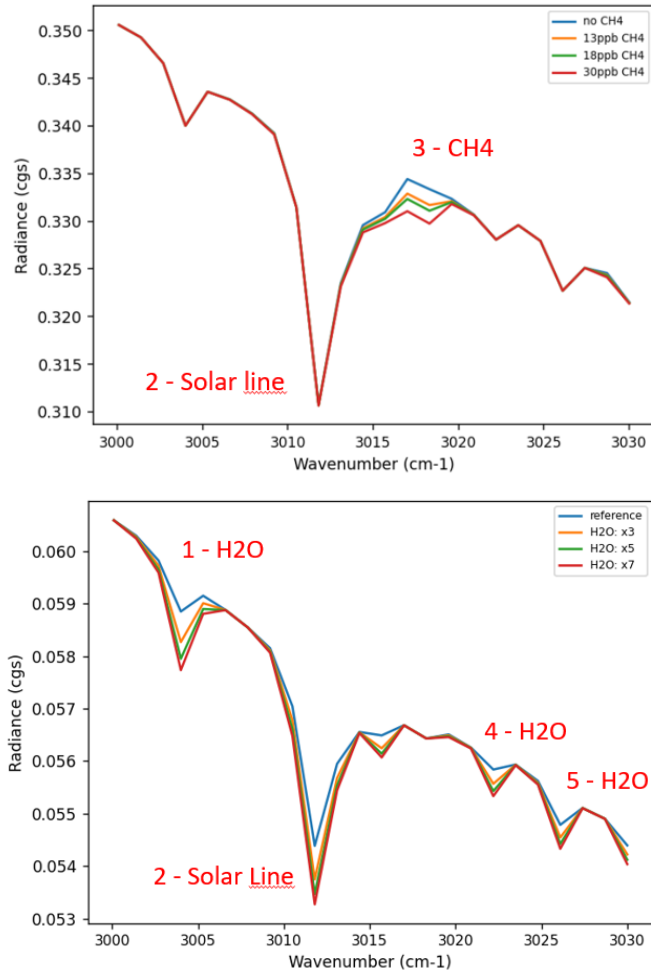
Figure 3.16: Identification of CH_4 and H_2O lines in MEx simulation - Mars. **Top plot:** Effect of the variation of methane abundance in the model in the resulting radiance, for CH_4= 0 ppb (blue), 13 ppb (orange), 18 ppb (green) and 30 ppb (red). A methane absorption line was identified. **Bottom plot:** Effect of the variation of H_2O in the model in the resulting radiance, for H_2O= 1 (blue, standard abundance of H_2O in the model), H_2O= 3 (orange), H_2O=5 (green) and H_2O=7 (red). Three H_2O absorption lines were identified. The position of the lines, in general, are in agreement with positions in HITRAN (see Table 3.6)

To simulate MEX and ExoMars observations I used as atmospheric input for PSG the Mars Climate Database (MCD) (Forget et al. [22], Millour et al. [46]) model, dedicated for Mars (see Fig. 3.15)

Following the same procedure as for the case of Venus (see Chapter 3, section 3.1), I varied the abundance of CH_4 and H_2O of the martian reference spectrum, fixing all other parameters of the simulation, in order to identify, as a first approximation, lines of these species (see Fig. 3.16, Table.3.6).

The spectra simulations for MEx are in Fig. 3.17 and ExoMars simulations are in Fig. 3.18.

The first step done in the fitting for MEx data was to fit the solar line at around 3012 cm^{-1}. The second step was to fit the water lines, by adjusting the abundance of water in the model. The abundance of water was estimated by about 30-300 ppm, compared with a value of 350 ppm from the literature. The fit is good, in general. The simulation with no methane (orange line), has a $\chi^2(red) \sim 4.8$ and the simulation with 18 ppb of methane has $\chi^2(red) \sim 5.4$. At around 3015-3025 cm^{-1}, a correction function might have to be applied to the data, due to the instrument line shape of the PFS (Giuranna et al. [26]), which until now could not be applied to the simulation. After this correction is done, I will be one step closer to the estimation of the abundance of methane (for more details see Chapter 4).

The first step of the fitting for ExoMars data was to adjust the level of the continuum of the simulation with the one from the observations. This was done by changing the abundance of dust and ice in the model,
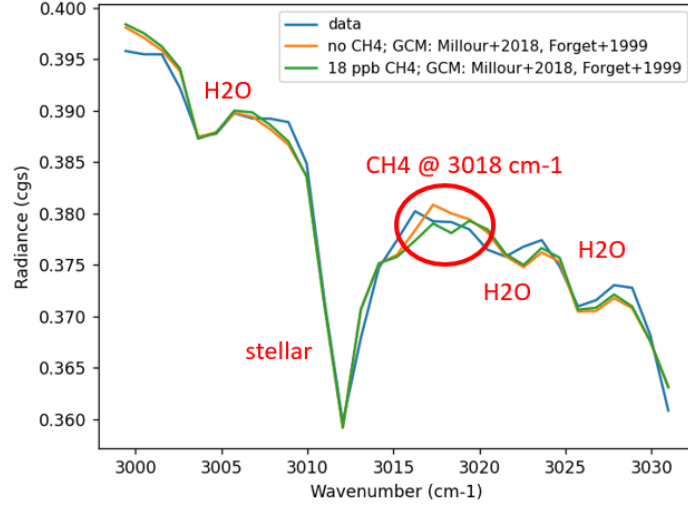
Figure 3.17: Comparison between bestfit simulations and data (Giuranna et al. [26]). Blue line : data; Orange line: MCD (Forget et al. [22], Millour et al. [46]) with no methane; Green line: MCD with 18 ppb of methane. The fit of both simulations is good in general. Highlighted in the red circle is the region where the methane absorption line is present, both in the data and in the orange line. The simulation with no methane has a $\chi^2(red) \sim 4.8$ and the simulation with 18 ppb of methane has $\chi^2(red) \sim 5.4$. One stellar line and several water lines are identified (see Table. 3.6 for position of the lines.)

Line (cm^{-1})	Simulation	HITRAN
1 - H_2O	3004.00 ± 0.7	H_2O - 3003.84
2 - Solar Line	3011.80 ± 0.7	—–
3 - CH_4	3018.30 ± 0.7	CH_4 - 3018.29
4 - H_2O	3022.20 ± 0.7	H_2O - 3021.53
5 - H_2O	3026.10 ± 0.7	H_2O - 3025.96

Table 3.6: Methane on Mars, MEx observations - Line Identification. The position of the lines is, in general, in agreement with the positions from HITRAN (Gordon et al. [28]). The quantification of the error associated with the measurement of the position of the lines is ongoing

by multiplying or dividing the vertical abundance profiles by a constant, and also by changing the altitude of the line of sight of the solar occultation in the model. Ice clouds were removed from the model, the dust abundance was set equal to the one of the MCD (Forget et al. [22], Millour et al. [46]) and the height of the occultation was set to 8.6 km, close to the altitude of the observations, 5.9-8.0 km.

Methane was not detected in the ExoMars data, around 3048 cm^{-1} and 3029 cm^{-1}. However, in the simulations, methane is easily identified for an abundance of 0.5 ppb.

A discussion of some possible reasons that may explain both positive and negative detections of methane is explored in Chapter 4.

3.2.2 Determination of the D/H ratio

Observations from Encrenaz et al. [18] were simulated, at 1388-1389.2 cm^{-1}, without terrestrial absorption applied in PSG. The atmospheric model used was the MCD (Forget et al. [22], Millour et al. [46]). The HDO vertical profile and the H_2O profile were assumed to be uniform.

The simulation is compared with data in the Fig. 3.19.

First, I measured the depth of the weak H_2O line at around 1388.6 cm^{-1}, the weak HDO line at 1388 cm^{-1} and of the weak CO_2 line at 1367.97 cm^{-1}. Then, considering a fixed abundance of 450
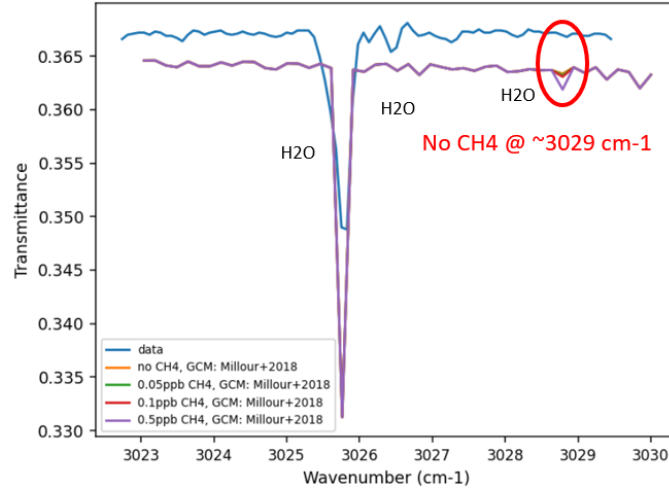
Figure 3.18: Comparison between simulation and ExoMars data (Webster et al. [72]), at 3023-3030 cm^{-1}. H_2O lines are identified. Several abundances of methane were tested, namely 0.05 ppb (green line), 0.1 ppb (red line) and 0.5 ppb (purple line). The upper limit derived by observations was 0.05 ppb. For an abundance of 0.5 ppb, the methane absorption line is easily identified in the simulation and not identified on the data. Near 3029 cm^{-1} there might exist lines of O3 that mix with methane lines, preventing the clear identification of methane, for low abundances, in the data.
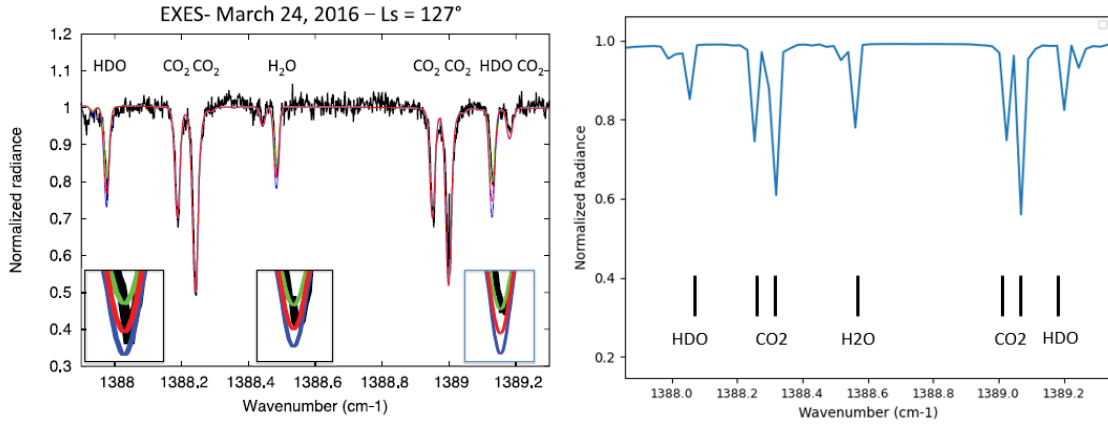
Figure 3.19: Comparison between simulation and EXES data, at 1388-1389.2 cm^{-1} (Encrenaz et al. [18]). **Left:** EXES data, at 1388-1389.2 cm^{-1}, with the corresponding line identification. The line identification is identical in both figures. **Right** Normalized radiance simulation, with the corresponding line identification. The depth of the H_2O and HDO lines in the simulation is different from the data. This means that the abundances of these species must be adjuste (see Chapter 4 for more details).

ppb of HDO, I tried different H_2O abundances, such as 100 ppm, 200 ppm, 300 ppm, 450 ppm and 500 ppm and performed the corresponding simulations. After this, I fixed the abundance of H_2O at 318 ppm, and performed simulations for the following abundances of HDO: 300 ppb, 350 ppb, 400 ppb, 500 ppb, 550 ppb and 600 ppb. For each of these combinations of abundances I measured two line depth ratios: HDO/CO_2 and H_2O/CO_2. I studied their variations for the different combinations of abundances. I obtained two linear equations of the type: ldr(HDO/CO_2)= a vmr (HDO) + b and ldr(H_2O/CO_2)= c vmr (H_2O) + d.

The following linear equations were obtained for the ldr:

$$ldr(HDO/CO_2) = 0.0055 vmr(HDO) + 0.9732$$

$$ldr(H_2O/CO_2) = 0.009 vmr(H_2O) + 0.3114$$

48

Finally, I substituted the value of ldr(HDO/CO_2) and ldr(H_2O/C2O) obtained in the latter expressions, to estimate the abundance of H_2O and HDO. For the data, we have ldr(HDO /CO_2) ∼ 4.17, ldr (H_2O/CO_2) ∼ 3.17.

The abundances of HDO and H_2O estimated were 581 ppb and 318 ppm, respectively. The values obtained by Encrenaz et al. [18] were H_2O= 253-307 ppm and HDO=303-397 ppb.

The calculation of the D/H ratio gives D/H ∼ 5.9 D/H (Earth), in comparison with D/H = 3.4-4.8 D/H (Earth) (Encrenaz et al. [18]) and D/H = 3.9-5.3 D/H (Earth), from Krasnopolsky [38].
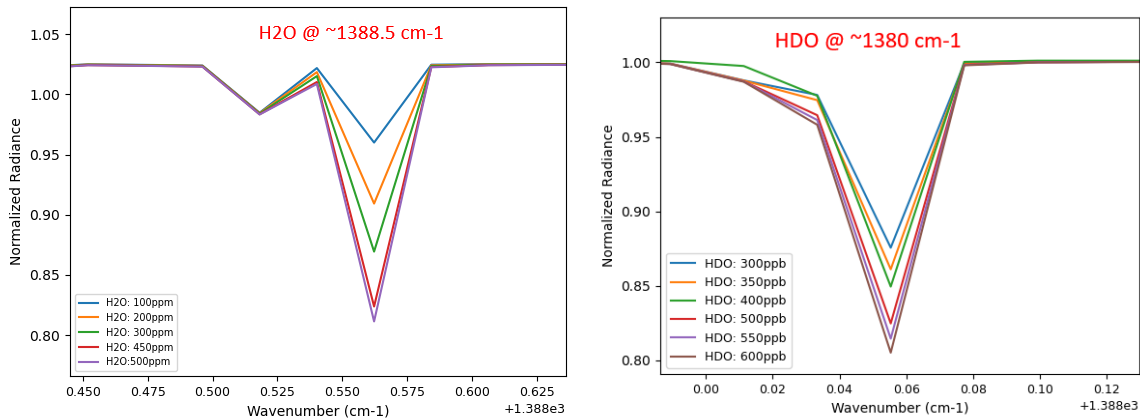
Figure 3.20: The effect of the variation of the abundances of HDO and H_2O in the simulations. The depth of the lines increases linearly with an increase in their abundances. **Left plot:** HDO=450 ppb for H_2O=100 ppm, 200ppm, 300ppm, 450ppm and 500 ppm; **Right plot:** H_2O=318 ppm, for HDO = 300 ppb, 350 ppb, 400 ppb, 450 ppb, 500 ppb, 550 ppb and 600 ppb

3.3 Jupiter

The goal of the simulations are: (1) to reproduce ISO observations from Encrenaz et al. [16], between 7 μm and 12 μm, in order to identify features and determine the abundances of phosphine (PH_3), ammonia (NH_3), deuterated methane (CH_3D) and methane (CH_4); (2) get an estimation of the D/H ratio from the ratio of abundances CH_3D/CH_4. Two different atmospheric models were used as input for PSG, one using the NEMESIS CIRS template and other using Moses et al. [49] model. On both models, a uniform CH_3D vertical profile was used, with an abundance of 0.1 ppm. It is important to notice that in PSG, isotopic ratios are set equal to those of Earth, therefore a correction factor must be applied before defining a uniform profile for CH_3D. This way, in Fig. 3.21 (middle and bottom plots), the VMR of CH_3D appears as 1.6×10^{-4}, taken into consideration the correction factor. The real value is 1.0×10^{-7}, the correction factor being $1/6.157510 \times 10^{-4} \sim 1624$. This correction factor was taken from HITRAN.

A brief description of the parameters of the simulations is in Table. 3.7 and the vertical composition profiles and thermal profile used are represented in Fig.3.21.

Using the method of the variation of abundances (see Fig. 3.22), I identified methane emission between 7 and 9 μm, NH_3 absorption between 9 μm and 12 μm, and PH_3 absorption between 8 μm and 11 μm. The molecular bands identification in the simulation is in agreement with the band identification in the ISO data (see Fig. 3.23). I choose to do this identification in the simulation using the NEMESIS CIRS template. The reason for this is highlighted in Chapter 4, Section 4.3

Next, I compared the data with the two simulations, as show in Fig 3.23. In the top plot, there is an agreement between the bands identification between simulation (blue line) and data (orange line). However, that does not happen in the bottom plot. Also in the top plot, it is evident that the simulation
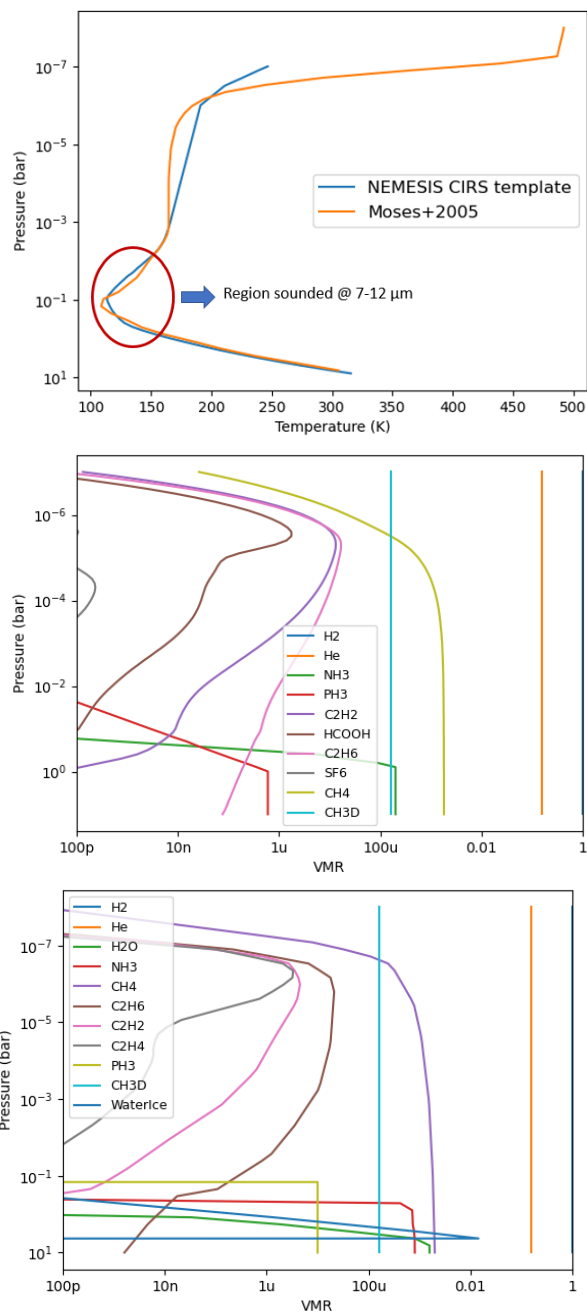
Figure 3.21: Top: Vertical thermal profile of the jovian atmosphere for two different models: Moses et al. [49] and NEMESIS CIRS template. Pressure (bar) as a function of Temperature (K). **Middle:** Vertical Mixing Ratio (molecule/molecule) of the jovian atmospheric components (H_2, He, NH_3, PH_3, C_2H_2, HCOOH, C_2H_6, SF_6,CH_4,CH_3D) as a function of pressure (bar), for the NEMESIS CIRS template. The CH_3D profile is based on Lellouch et al. [40]. **Bottom:** Vertical Mixing Ratio (molecule/molecule) of the jovian atmospheric components (H_2, He, H_2O, NH_3, CH_4, C_2H_6, C_2H_2, C_2H_4, PH_3, CH_4) as a function of pressure (bar), for the Moses et al. [49] model. The CH_3D profile is based on Lellouch et al. [40].
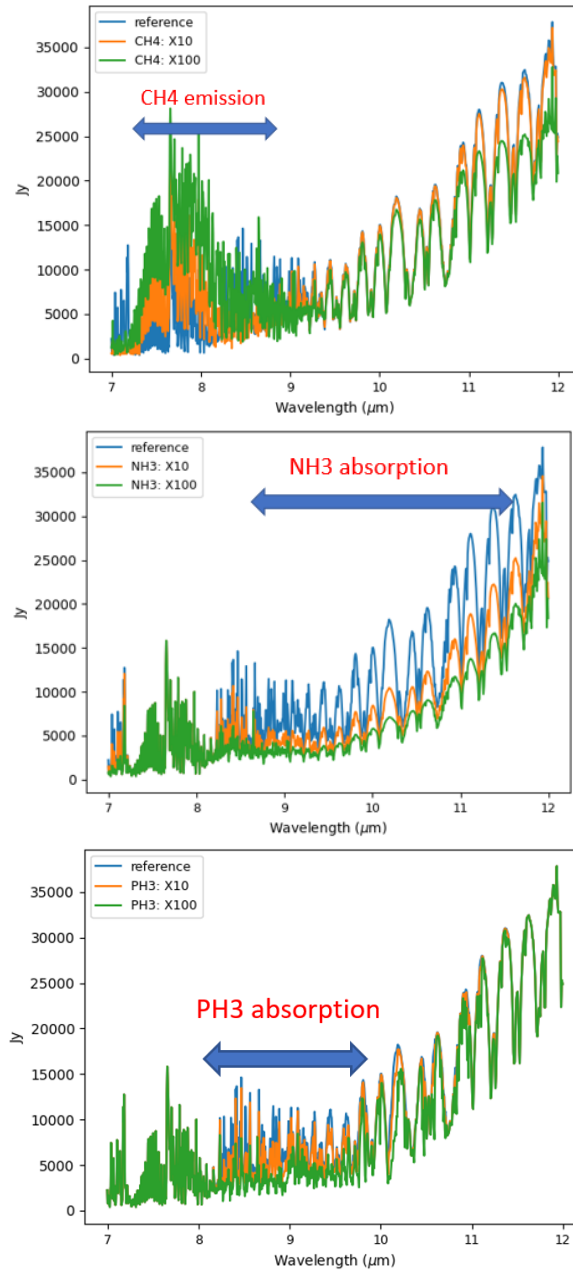
Figure 3.22: Exploration of the effect on the jovian spectrum of the variation of the abundance of CH_4, NH_3 and PH_3, for R=1500. A methane emission band was identified at 7-9 μm (**Top plot**), an absorption band due to NH_3 has been identified between 9-12 μm (**Middle plot**), and an absorption band due to PH_3 has been identified at 8-10 μm (**Bottom plot**)

Parameters	Value
Altitude range	NEMESIS CIRS template: 0-421 km (10^{-7}-10 bar)
	Moses et al. [49]: 0-573 km (10^{-8}-10 bar)
"Surface" Pressure	NEMESIS CIRS template: 10 bar; Moses et al. [49]: 10 bar
"Surface" Temperature	NEMESIS CIRS template: 338 K; Moses et al. [49]: 340 K
Tropopause	NEMESIS CIRS template: $\sim 0.1 bar, 114K$; Moses et al. [49]: $\sim 0.1 bar$, 110 K,
Wavelength	7-12 μm
Molecules included	NEMESIS CIRS template : H_2, He, NH_3, PH_3, C_2H_2, HCOOH, C_2H_6
	SF_6,CH_4,CH_3D
	Moses et al. [49] : H_2, He, H_2O, NH_3, CH_4, C_2H_6, C_2H_2, C_2H_4, PH_3, CH_4
Terrestrial transmittance	removed
Geometry	Nadir, day-side, April 1996
Observations to simulate	ISO observations, 7-12 μm, Encrenaz et al. [16]

Table 3.7: Atmospheric Parameters - Jupiter. Description of some of the parameters of the jovian simulations.

is over-predicting the data. At 7-9 μm, emission of CH_4 dominates the spectrum. This suggests that to fit the data, I should decrease the abundance of this species in the model. At 9-12 μm, NH_3 absorption dominates. This suggests that to fit the data, the abundance of NH_3 in the model should be increased. Moreover, looking at the bottom plot, for reasons that still need to be further studied, at 9-12 μm, in the simulation NH_3 is in emission (blue line) and not in absorption, as in the data (orange line). This issue is addressed in Chapter 4, Section 4.3.

As a result, I choose to proceed with the retrieval of the abundances of CH_4, CH_3D, NH_3 and PH_3 using the NEMESIS CIRS template model.

3.3.1 Phosphine, Ammonia and Methane

The fit between simulation and data to determine the abundances of CH_4, NH_3 and PH_3 is in Fig 3.24. The parameters of the retrieval and resulting abundances are on Table 3.8

In the top plot of Fig 3.24, from the fit it was not possible to estimate the abundance of CH_4 and CH_3D, since there is a large difference between simulation and data, with a $\chi^2(red) \sim 108$.

In the middle plot, the fit is good overall, with a $\chi^2(red) \sim 8$. An excellent fit is achieved when $\chi^2(red) \leq 1$.

In the bottom plot, it is presented the best fit of CH_4 emission and CH_3D absorption at 8.0-9.0 μm. This fit has a $\chi^2(red) \sim 60$. The abundances obtained for CH_4 and CH_3D are, respectively, 2.9×10^{-3} and 1.3×10^{-7}, comparable with $1.8 - 5.6 \times 10^{-3}$ and 1.6×10^{-7} (Encrenaz et al. [16], Lellouch et al. [40]). From these abundances, D/H (CH_4) = $\frac{1}{4}\frac{CH3D}{CH_4} \sim 1.1 \times 10^{-5}$, comparable with D/H ($CH_4$) = $1.5 - 2.9 \times 10^{-5}$ (Lellouch et al. [40]). Moreover, we know that f= $\frac{D/H(CH_4)}{D/H(H_2)}$. Using f=1.13-1.37 (Lellouch et al. [40]), derived from laboratory studies, we get D/H (H_2) = 8.7-9.7×10^{-6} comparable with D/H (H_2) = $1.9 - 2.6 \times 10^{-5}$ (Lellouch et al. [40]). For more details on the improvement of this result, see Chapter 4.
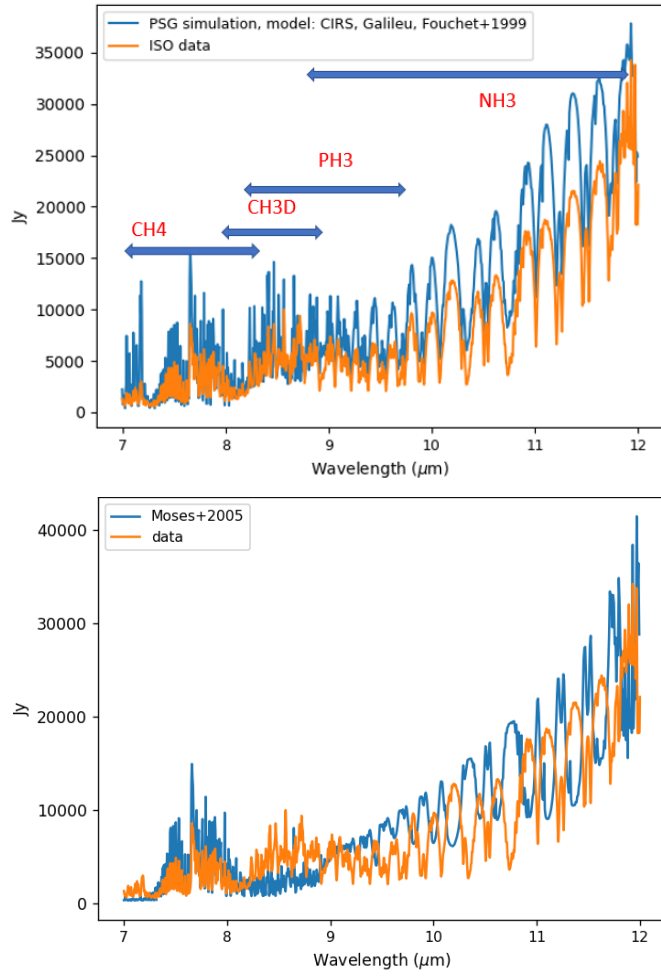
Figure 3.23: Left: Comparison between the simulated jovian spectrum, using as input the NEMESIS CIRS model and observational data from ISO (Encrenaz et al. [16]). Several molecular bands are identified in the figure. The simulation is over-predicting the data. To correct this, the vertical abundances profile of the molecules highlighted in the figure should be adjusted; **Right:** Comparison between the simulated jovian spectrum, using as input the Moses et al. [49] model and observational data from ISO (Encrenaz et al. [16]). At 9-12 μm NH_3 is in emission in the simulation, although in fact it should be in absorption as shown in the data

Parameter	Value
RCHISQ CH_4+CH_3D	60
RCHISQ NH_3+PH_3	8
VMR CH_4	$(2.8 - 3.0) \times 10^{-3}$
VMR CH_3D	$(1.23 - 1.37) \times 10^{-7}$
VMR NH_3	$6 \times$ reference profile
VMR PH_3	$5.8 \times$ reference profile

Table 3.8: Retrieval parameters for CH_4 and CH_3D at 8.2-9 μm and for NH_3 and PH_3 at 9-11 μm. RCHISQ=reduced chi-square = chisq/[npts-dof]; npts = number of spectral points; dof = degrees of freedom

53
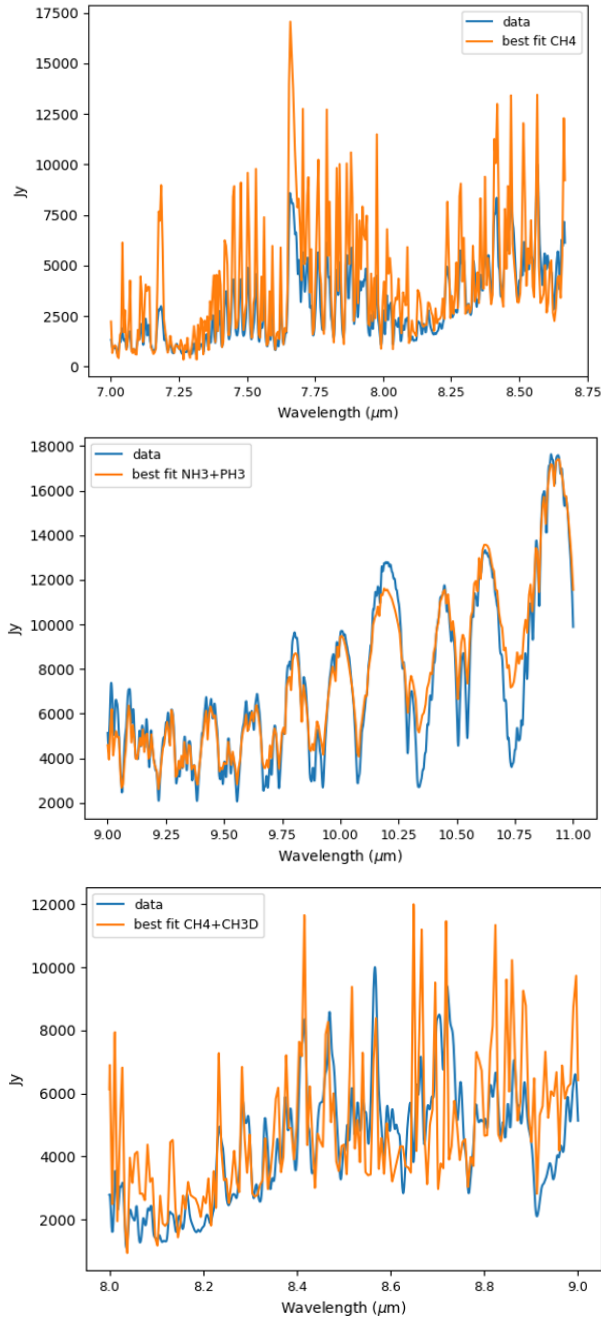
Figure 3.24: Top plot: Fit of the CH_4 emission at 7-9 μm; **Middle plot:** Fit of NH_3 and PH_3 absorption, between 9 μm and 11 μm. $\chi^2(red) \sim 8$; **Bottom:** Best fit of CH_4 emission and CH_3D absorption at 8-9 μm. $\chi^2(red) \sim 60$. See Chapter 4 to address ways to improve the fit

Chapter 4

Discussion

4.1 Venus

Different models were used as atmospheric input for PSG. There are differences in the temperature-pressure profile (see Fig.3.1)), in the sulphur dioxide vertical composition profile and in the water vertical composition profile (see Fig. 4.1) between the two models. The difference between the temperature-pressure profiles is about 5-10 K, around 0.1 bar. Bellow 0.1 bar, the SO_2 profiles differ up to about one order of magnitude in abundance. Moreover, above 0.1 bar, the difference can be up to about 3 orders of magnitude in abundance. The H_2O profiles differ up to about one order of magnitude in abundance, around 0.1 bar.
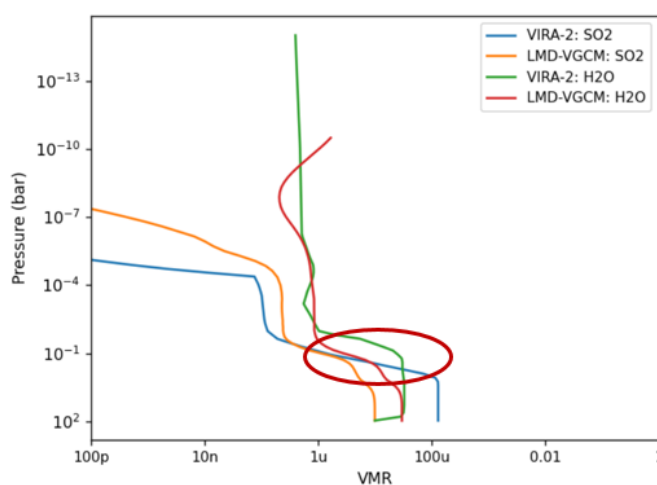
Figure 4.1: Detail on the different abundances of SO_2 and H_2O in the VIRA-2 and LMD-VGCM model. The highlighted region in the red circle corresponds to the pressure level where the SO_2 absorption is thought to originate from, ~ 0.1 bar

The VIRA-2 model produces simulations with a higher radiance that the LMD-VGCM model, up to about 31 % higher, as can be seen in Fig. 3.4. This can be due to the higher temperature in the pressure range responsible for the spectrum at 1350.1-1350.8 cm^{-1}. The VIRA-2 model has a similar SO_2 abundance as the LMD-VGCM model, at the pressure where the emission comes from, around 0.1 bar (highlighted in the red circle in Fig. 4.1). This suggests that changing the sulphur dioxide vertical profile may not affect the resulting radiance, in particular, may not affect the depth of the SO_2 lines.

I explored the effect of different temperature-pressure profiles on the resulting radiance, to understand the possible origin of different depths for the SO_2 lines and also different width according to the specific model used. I created two different temperature-pressure profiles intermediate between the VIRA-2 and

LMD-VGCM models (see Fig. 4.2, Fig. 4.3), named test1 and test2. Test1 and test2 were constructed as deviations from the VIRA-2 model. Test1 represents a situation where the temperature-pressure profile is explored around 0.1 bar, the region where the absorption of SO_2 is occurring (Encrenaz et al. [17]). Test2 represents a situation where the gap between the two models is explored around $10^{-4} - 10^{-7}$ bar.

For test1, a decrease in the temperature, up to 5 K in relation to the VIRA-2 temperature, produces a decrease in the resulting radiance, about 10 %. This decrease is approximately a constant in the entire wavenumber interval of the simulation. From Fig. 3.4, we see that the radiance of the dataset is at most about 25 % higher than the radiance of the VIRA-2 model and about 67 % higher at most than the radiance of the LMD-VGCM model (see Fig.3.4). This suggests an increase of the temperature in the models should produce a closer match of the simulated radiance to the data.

For test2, the resulting radiance difference in comparison with the VIRA-2 model is about 2-4 %, suggesting that in fact the absorption of SO_2 is coming from around 0.1 bar.

The effect of using different SO_2 profiles on the model is explored on Fig. 4.4. The difference is not significant. This does not mean that altering the SO_2 profile for sure does not produce alterations in the resulting radiance, such that work regarding the exploration of different SO_2 cutoff pressures (the pressure value corresponding to the start of a decrease in the abundance of SO_2) and gradients are undergoing to test their effect on the resulting radiance and confirm the previous result.
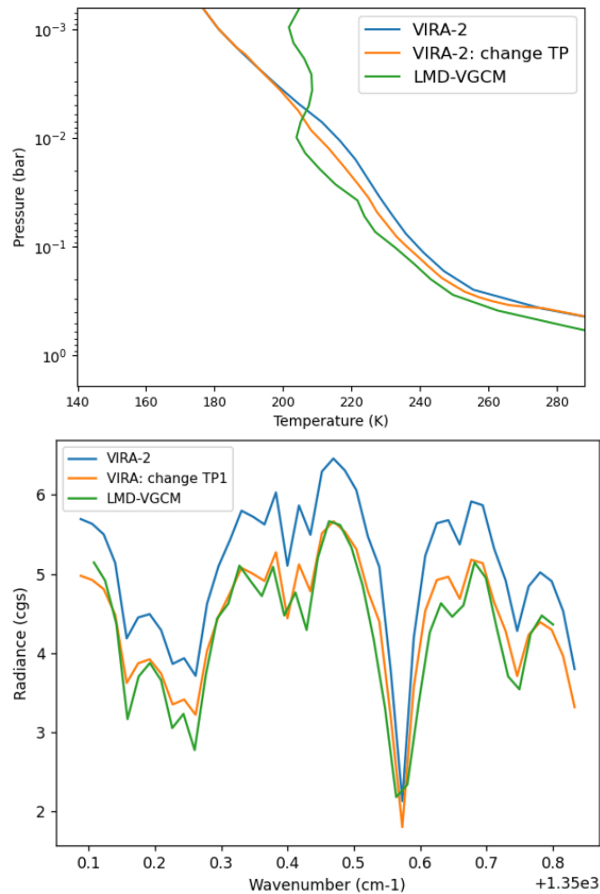
Figure 4.2: The effect of changing the temperature-pressure profile on Venus - Test1. In the top plot are presented three different temperature-pressure profiles and in the bottom plot the corresponding resulting radiances. When the temperature decreases (VIRA-change TP1=test1), the resulting flux also decreases, but the relative depth of the lines remains the same. The same applies for the width. **Bottom plot:** Blue: VIRA-2 simulation, Green: LMD-VGCM simulation, Orange: test1; LMD-VGCM model: Gilli et al. [25],Garate-Lopez and Lebonnois [24]; VIRA-2 model: Zasova et al. [74]
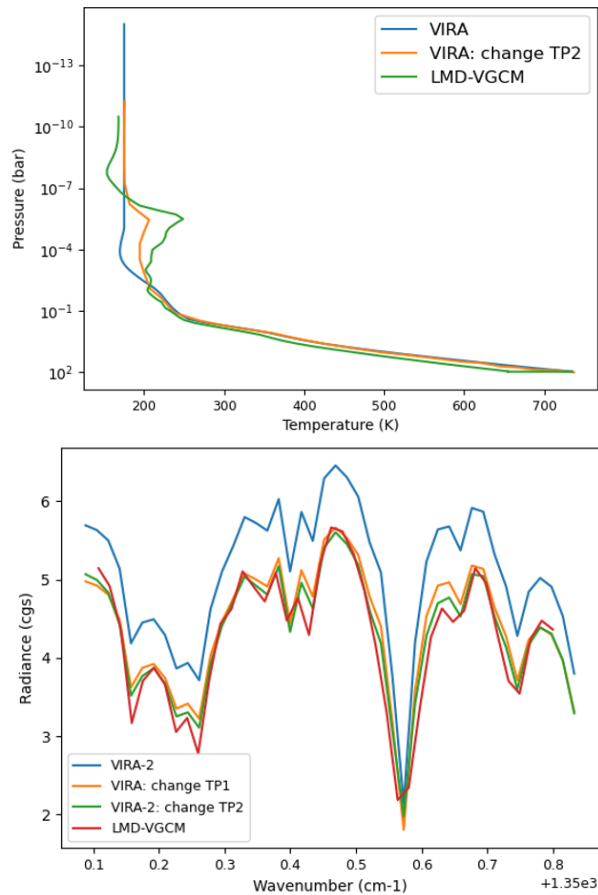
Figure 4.3: The effect of changing the temperature-pressure profile on Venus - Test2. In the top plot are presented three different temperature-pressure profiles and in the bottom plot the corresponding resulting radiances. In general, the temperature of test2 (VIRA: change TP2) is higher than in VIRA-2. This results in a decrease of the resulting radiance, which can be explained by the decrease in the temperature similar to test1 used for pressures around 0.1 bar. This suggests the absorption of SO_2 is coming from around 0.1 bar, as described in Encrenaz et al. [17]; **Bottom plot:** Blue: VIRA-2 simulation, Green: LMD-VGCM simulation, Orange: test1, Green: test2; LMD-VGCM model: Gilli et al. [25],Garate-Lopez and Lebonnois [24]; VIRA-2 model: Zasova et al. [74]
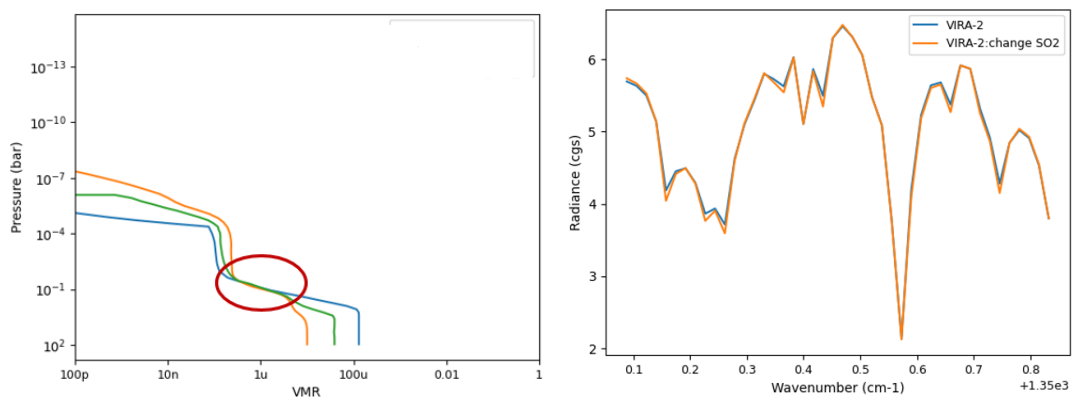
Figure 4.4: The effect of changing the SO_2 profile on Venus. In the right plot, there are three different SO_2 profiles. One from the VIRA-2 model (blue line), other from the LMD-VGCM model (orange line), and an intermediate SO_2 profile between the previous two (green line). In the bottom plot, there are two simulations, one corresponding to the VIRA-2 model (blue line) and other corresponding to the VIRA-2 model with changed SO_2 profile (orange line)

4.1.1 Sulphur Dioxide

The value estimated for the abundance of SO_2 using the line depth ratio method, in general, is in agreement with the literature (see Table 3.3).

The first step of the retrieval procedure was to fit the strong CO_2 line, at around 1350.6 cm^{-1}, the second was to fit the water absorption at 1350.2-1350.3 cm^{-1}, and finally to fit the SO_2 absorption lines.

The source of the error of the retrieval method is still being evaluated, but seems to depend on the uncertainty of the radiance measured in the observations, which was assumed to be 5 % by the PSG retrieval module, as a default.

The error in the line depth ratio method is mainly due to: (1) difficulties in the definition of the continuum, due to the modelling of the water absorption, which will introduce an uncertainty in the measurement of the depth of the SO_2 lines; (2) the atmospheric model used and, in particular, uncertainties in the model in the definition of the vertical SO_2 profile, since there is evidence in the literature for variations of a factor 5-10 in the abundance of this species (Encrenaz et al. [17]).

The error derived from the definition of the continuum can be estimated by performing simulations without including telluric transmitance and comparing with the ones that include telluric transmittance. The abundance obtained for SO_2 without including telluric transmittance is about 100 ppb using the line depth ratio method. Therefore, I conclude that the definition of the telluric transmission can induce a relative error of about 35 %, for the VIRA-2 model simulations (derived abundance of SO_2 of about 154 ppb, including telluric transmittance). The error accounting for possible variability might be represented by the difference in abundance between the two models. This error can be accounted for by joining the two intervals of abundance derived for SO_2 (100-154 ppb for the VIRA-2 model and 20-43 ppb for the LMD-VGCM model). However, the abundance of SO_2 derived from the LMD-VGCM model is bellow the interval estimated by Encrenaz et al. [17] (about 50-175 ppb). This discrepancy has not been understood so far.

Since the variation of the SO_2 profile does not produce a substantial difference in the resulting radiance (see Fig. 4.4), but a variation in the temperature-pressure profile does (see Fig.4.3), this suggests that to move forward in order to improve the estimation of the SO_2 abundances, a first step would be to adjust the temperature-pressure profile. It is not clear why the width of the SO_2 absorption lines differ from one model to another, since the variation of the temperature-pressure profile and SO_2 vertical profile do not seem to produce different widths for those lines (see Fig. 4.4, Fig. 4.3).

All the steps done to determine the abundance of SO_2 are of paramount importance to help in the search for phosphine on Venus, since telluric H_2O lines and SO_2 lines overlap with phosphine lines, throughout IR wavelengths.

4.1.2 Phosphine

Looking at Fig. 3.9, we can see that there is a discrepancy bellow a factor of 2 between data and simulations. In particular, the VIRA-2 model has a higher radiance than the data, up to about 36% (at 955.2 cm^{-1}), and a lower radiance with respect to the LMD-VGCM model, up to about 28 % lower (at 955.2 cm^{-1}). The LMD-VGCM model has a lower temperature than the VIRA-2 model in the pressure region of interest (see Fig. 3.1, highlighted red circle in the top plot). Therefore, it is not clear why it presents a higher simulated radiance than the VIRA-2 model (see Fig. 3.9). Moreover, let me stress that the CO_2 lines at around 955.4 cm^{-1} and 955.34 cm^{-1} of both models are broader than the ones from the data. For the line at 955.4 cm^{-1} the corresponding depths are, respectively, for the data, the VIRA-2 and the LMD-VGCM simulations, the following: ~ 0.13, ~ 0.11, ~ 0.24. In detail, we see that the VIRA-2 model has less broad CO_2 lines that the LMD-VGCM model. To correct the features highlighted above a correction to the temperature-pressure profile and the CO_2 profile is undergoing.

Regarding the telluric water absorption, in both models, it is broader and stronger than in the data.

This discrepancy in telluric water absorption was solved when doing the fit of telluric transmittance using the PSG module.

The depth of the phosphine line can be estimated based on the difference between the depth at the position of the line using simulations with phosphine included in the model and simulations without phosphine included in the model. For example, for 10 ppb of PH_3 the depth of the line is about 0.002, in comparison with 0.07 for the depth at the same wavenumber (around 955.26 cm^{-1}) without phosphine. Thus, the contribution of phosphine is about 3 % the contribution of the telluric absorption to the depth at 955.26 cm^{-1}. When the telluric transmission is removed, the phosphine absorption line appears clearly visible, however it is still very weak (see Fig. 3.9, right plot).

In Fig. 3.10, the VIRA-2 presents a better fit to the data than the LMD-VGCM model, with $\chi^2(red)$ (VIRA) = 0.1 and $\chi^2(red)$ (LMD-VGCM) = 0.6. The telluric water absorption at 955.2-955.3 cm^{-1} is reproduced by both models. However, its presence clearly precludes the identification of the phosphine absorption line at the predicted position of 955.26 cm^{-1}. Bellow 955.2 cm^{-1} and above 955.4 cm^{-1}, both models deviate from the data significantly. The reason for this deviation is not clear at present. One possibility to explore in the future is to understand the physical processes behind the different temperature-pressure profiles of VIRA-2 and LMD-VGCM models and explore intermediate profiles.

The negative detection of phosphine does not preclude the existence of phosphine on Venus. What it does mean is that further dedicated observations to look for phosphine on Venus should be done. The main phosphine absorption bands are located around 2.7-3.6 μm, 4-4.8 μm and 7.8-11 μm. All those spectral regions should be used to search for phosphine, specially at $4-4.8\mu$m, which is the strongest band. One also has to consider possible latitudinal, temporal and altitude variations in the abundance of phosphine. Considering these factors, the non-detection of phosphine at z~60 km, may indicate that phosphine is not present at the probed altitude in sufficient abundance to be clearly detected (Encrenaz et al. [20]).

To conclude, the detection of phosphine on Venus is extremely difficult due to the possible low abundance and overlapping of the phosphine absorption lines with sulphur dioxides absorption lines, present in much larger abundances, and telluric water absorption, when doing ground-based observations.

4.1.3 Determination of the D/H ratio

The estimated D/H ratio of Venus, D/H $\sim$ 29 D/H (Earth), is about a factor of three bellow the value determined by de Bergh et al. [7], D/H = 80-160 D/H (Earth).

This discrepancy can be explained by several factors: (1) correction of the HDO line (4168 cm^{-1}) depth due to blending with H_2O lines; (2) correction of the H_2O vertical profile for altitudes 30-40 km; (3) correction to the temperature-profile profile; (4) the definition of the continuum, in order to perform normalization and measure the depth of the lines. The quantitative uncertainty introduced by each of the latter factors is being evaluated. Nevertheless, I calculated that the Planck function, at a temperature of 450 K, varies by about 13 % between 4140 cm^{-1} and 4190 cm^{-1}. This suggests that the continuum changes by a similar amount and therefore the normalization factor depends on wavenumber. This will introduce an uncertainty in the measurement of the depth of the CO line (4170 cm^{-1}). However, this does not change the resulting D/H ratio significantly ($<$ 10 %).

First, I explored a possible correction to the HDO line depth. Due to limited resolution of the observations, HDO lines are blended with H_2O lines, although the HDO lines are stronger (see Fig.3.12). The HDO line was chosen such that this effect is minimized. However, a contribution from H_2O remains. Therefore, the depth of the HDO line measured is the sum between the real depth of the HDO line plus

a contribution from H_2O. This contribution was estimated to be about 0.1, Correcting for this gives an abundance of HDO of 0.6 ppm and D/H $\sim$ 58 D/H (Earth), comparable with D/H= 80-160 D/H (Earth) (de Bergh et al. [7]), corresponding to a relative error of about 52 %. This was estimated using the ratio between the line-to-continuum ratio with HDO + H_2O and the line-to-continuum ratio with only HDO in the model (see Fig.4.5). The line-to-continuum ratio results from the ratio between the spectrum with a certain species at reference abundance over the spectrum with the abundance of the same species set to 0. A line-to-continuum ratio less than 1 indicates absorption (this quantity can also be used to identify absorption lines).

Second, the H_2O abundance profile was adjusted. The H_2O abundance of the model is 33 ppm, comparable to 34 ppm, the abundance estimated by de Bergh et al. [7]. Therefore, adjusting the water profile in the altitude of interest, 32-42 km, should not produce a significant difference in the depth of the HDO line at 4168 cm^{-1}. This is true, as can been seen in Fig.4.5, bottom plot..

Finally, the temperature-pressure profile was adjusted at 30-40 km. First, the temperature was increased by 10 K at this altitude range, then it was decreased by 10 K (see Fig. 4.6). Increasing the temperature by 10 K improves the estimation of the D/H ratio. The new value is D/H $\sim$ 0.02 $\sim$ 107 D/H (Earth), comparable with D/H = 80-160 D/H (Earth), corresponding to a relative error of about 12 %. The reason for this improvement is still not well grounded, since an alteration of the temperature-pressure requires further study.

In conclusion, I was not successful in the determination of the D/H ratio on Venus, but I have indications of the improvements to be performed.

.

4.2 Mars

4.2.1 Methane

I successfully reproduced the MEx positive detection of methane.

Comparing ExoMars observations with simulations (see Fig. 3.18), the expected methane absorption line is clearly visible in the simulation, although it is not present in the data.

Future works includes improving the fitting of the water lines for both MEx and ExoMars observations, by adjusting its vertical abundance profile. In particular, for the ExoMars simulations the depth of the H_2O lines as well as the continuum level must be adjusted to match observations.

We can see that we have a case of positive detection and a case of negative detection of methane. This discrepancy might be explained by the possibility of the methane abundance in the martian atmosphere having a spatial and temporal variation. However, it is not clear why the martian atmosphere would allow such a differentiation according to the most recent photochemistry and global circulation models (Webster et al. [71]). On one hand, when integrating several spectra for different latitudes, as in the ExoMars data, the methane signal might be weakened. The Mars Express observations, on the other hand, are integrating several hundred spectra for a localized region in the martian globe, around Gale Crater, which might have the result of increasing the methane signal. The different observations also sounded different altitudes of the martian atmosphere. ExoMars observations sounded the atmosphere around 5.8-8 km while the Mars Express observations obtained a column integrated abundance of methane.

In conclusion, the negative detection does not mean that there is not methane on Mars, due to the possible spatial and temporal variability of methane abundance on Mars. Therefore, further dedicated observations are needed to search for and study methane on Mars.
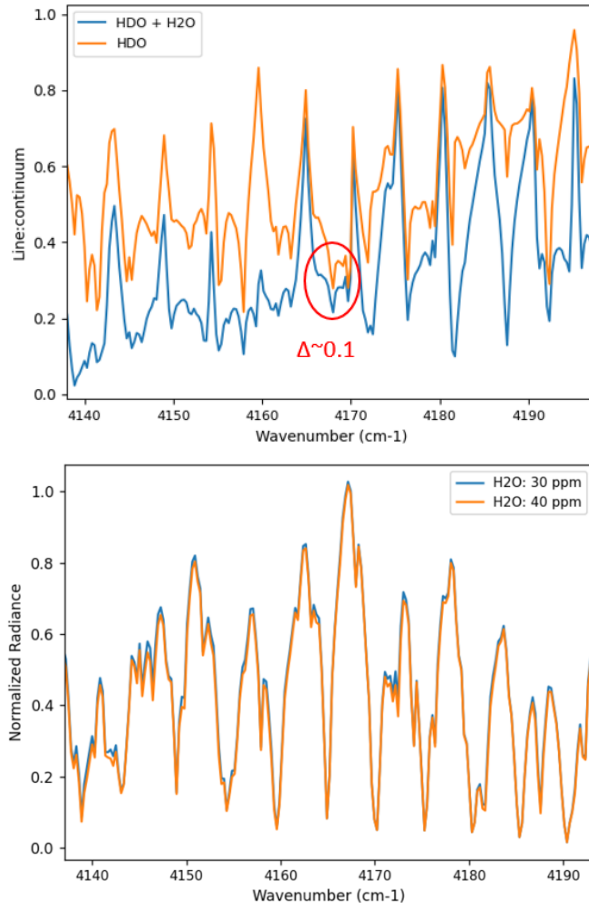
Figure 4.5: Effect of H_2O lines and effect of H2O vertical profile on the simulation - Determination of D/H ratio on Venus . **Top plot:** Line-to-continuum ratio (lc) for a model with H_2O+HDO (blue line) and a model with only HDO (orange line). This allows to distinguish the contributions of H_2O and HDO absorption in the observations. The lower the lc ratio the higher the absorption. Several absorption lines can be identified, corresponding to dips in the lc ratio. At around 4170 cm^{-1}, we see a small difference, about 0.1 between the lc ratio of the two lines. **Bottom plot:** Effect of the variation of the water abundance at around 30-40 km of altitude. 30 ppm H_2O - Blue line, 40 ppm of H_2O - orange line. The resulting radiance is similar.
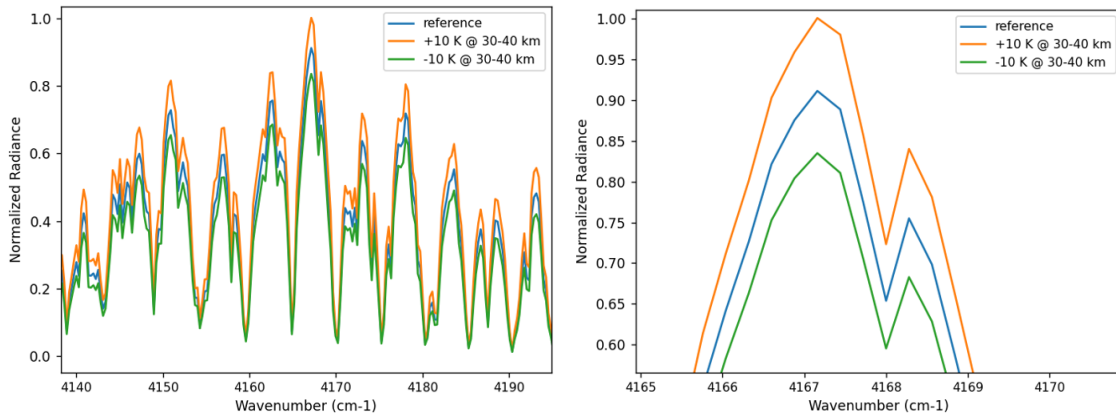
Figure 4.6: Variation of the temperature-pressure - Determination of the D/H ratio on Venus. **Left plot:** Effect of varying the temperature at around 30-40 km of altitude in the resulting radiance. Blue line: reference simulation; Orange line - temperature increased by 10 K at 30-40 km; Green line - temperature decreased by 10 K at 30-40 km; **Right plot:** Zoom of the top plot at around 4165-4170 cm^{-1}.

4.2.2   Determination of the D/H ratio

The value estimated for the D/H ratio is similar to the value obtained in the literature. The method used to estimate this value, the line depth ratio method, is validated by Encrenaz et al. [18].

The error associated with the estimation of the D/H ratio may have multiples sources such as: (1) the definition of the continuum level, and therefore, the measurement of the depth of the lines of H_2O, HDO and CO_2; (2) the presence of telluric absorption; (3) a possible deviation from linearity between the line depth rario and the abundances; (4) different pairs of H_2O/CO_2 and HDO/CO_2 lines may give different estimations of the abundances and therefore of the D/H ratio. I used one HDO line and one H_2O line to estimate the D/H ratio. To improve the estimate, one way forward would be to repeat this method for several H_2O and HDO line pairs, located around 1382-1391 cm^{-1} (7.2 μm). The quantitative contribution from each of these possible error sources is being evaluated. Also, these identified error sources do not preclude the existence of others as yet not identified. As an exercise, I calculated that a deviation of linearity of 10 % in the line depth ratio relation to abundance can produce a 10 % change in the resulting D/H ratio. Moreover, an error of 10^{-4} in the measurement of the continuum level can produce a change of 0.01 in the measured depth of a line. For example, for the HDO line at 1380 cm^{-1}, this can induce a change of more than 10 % in the estimated D/H ratio.

One could also argue that the depth of the CO_2 line used for the estimation of the D/H ratio, as well as from others, should be adjusted before adjusting the depth of the HDO and H_2O lines, to have the same depth as the lines from the observations.

4.3   Jupiter

The simulations produce fluxes which are dependent upon the geometry of the observations. The solid angle, angle of incidence and angle of emission, to name some parameters, were adjusted in PSG in order to minimize the difference between the data and simulations. This, of course, introduces a source of uncertainty, since I could not reproduce perfectly the values of flux of the observations (see Fig. 3.23). In order to see how the units of the output simulation might affect the comparison between data and simulation, I did a comparison between data and simulation using units of radiance (see Fig. 4.7, upper plot). There is a factor of 2-5 difference between simulation and observations. A similar comparison was done by Encrenaz et al. [16] (see Fig. 4.7, bottom plot). This difference is expected due to calibration effects, when performing observations. In future comparisons with data, the simulations will be performed using as output radiance units (nW cm^{-2} sr^{-1} cm^{-1}). The difference between the presented simulations and observations is solved when performing the fit with PSG through a correction factor.

I want to point out some differences between the Moses et al. [49] model and the NEMESIS CIRS template.

The Moses et al. [49] model includes two aerosol layers in the atmosphere (water ice clouds and ammonia ice clouds), but the NEMESIS CIRS template does not. Also, an H_2O profile is included in the Moses et al. [49] and not in the NEMESIS CIRS template. The same uniform CH_3D profile was used in both models, with an uniform vertical abundance of 0.1 ppm (see Fig. 3.21).

The thermal structure differs between the two models and should be taken into account when analysing the different resulting fluxes in the 7-12 μm region. The range of pressures where this difference is important is highlighted in the red circle Fig. 3.21, top plot. Moreover, the NEMESIS CIRS template has a lower abundance of ammonia and phosphine, in general, than the Moses et al. [49] model (see Fig. 3.21, middle and bottom plots). The CH_4 vertical profile is similar for both models (see Fig. 3.21, middle and bottom plots, cyan line).

Looking at the comparison between the Moses et al. [49] model and data (Fig. 3.23, bottom plot), we notice that the simulation has NH_3 in emission while it is in absorption in the data, at 9-12 μm. Also, the
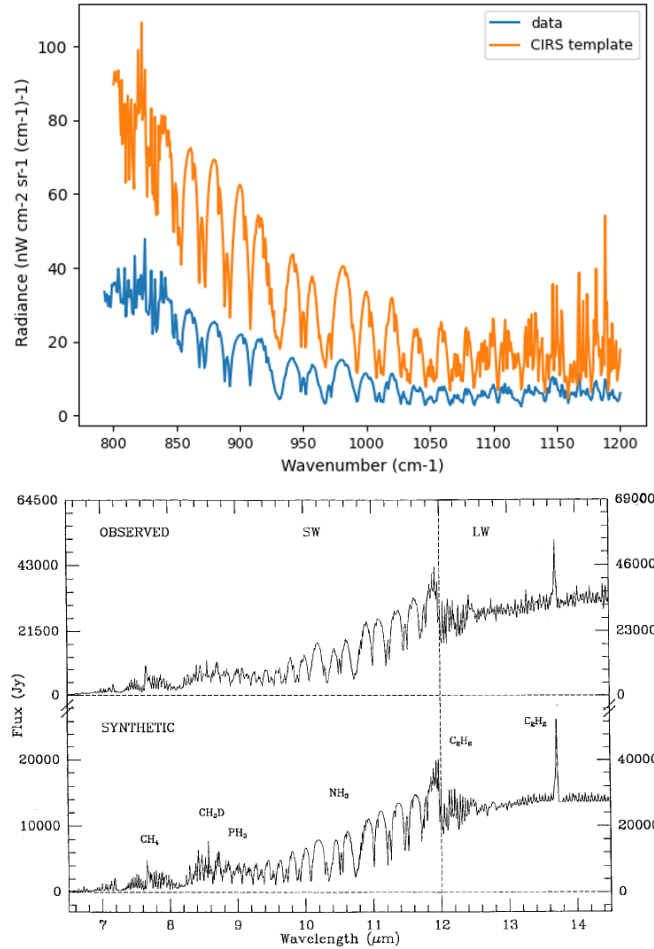
Figure 4.7: Comparison between ISO data and simulations in radiance. **Top plot:** Comparison between ISO data (blue line) and the resulting radiance from the NEMESIS CIRS template (orange line). The difference between the two varies by a factor between about 2, at 830 cm^{-1}, to about 5, at around 1190 cm^{-1}. **Bottom plot:** Comparison between data and simulation in Encrenaz et al. [16]. The difference is about a factor of 2. (bottom image credits: Encrenaz et al. [16])

simulation is under-predicting the data at 7-7.4 μm and at about 8-9 μm. This is the opposite situation of the CIRS template model (Fig. 3.23, top plot), which in general is over-predicting the data. The difference in the behaviour of ammonia (Fig. 3.23, bottom plot), highlighted above, might be explained by: (1) a flat ammonia profile slope for the Moses et al. [49] model compared to a more gradual decrease for the NEMESIS CIRS template; (2) the gradient of the temperature-pressure profile in the pressure region of interest is more pronounced in the Moses et al. [49] model than in the NEMESIS CIRS template; (3) the temperature is higher, in general, in the Moses et al. [49] model comparing with NEMESIS CIRS template, for pressures around 0.01-1 bar; (4) the ammonia and water ice layers included in the Moses et al. [49] model should be discarded. In fact they were not used in the simulations of the ISO data performed by Encrenaz et al. [16]. The presence of an ammonia ice cloud can explain certain spectral features around 3 μm (Brooke et al. [3]). However, in other parts of the spectrum there are included features which are not observed (Irwin [31]). The current best hypothesis is that the main cloud deck is mainly composed of contaminated ammonia ice particles, consistent with the lack of ice spectral features (Brooke et al. [3]). For this reason, I decided not to proceed to the retrieval and determination of D/H ratio using the Moses et al. [49] model, but instead I used the NEMESIS CIRS model. The quantitative contribution from these several possible factors to the differences between simulation and data is still not known, but work is ongoing to address this issue.

The next step was to explore the sensitivity of the resulting flux depending on variations of the

temperature-pressure profile, of the ammonia profile cutoff (the value of pressure where the abundance of ammonia starts to decrease with decreasing pressure) and of the ammonia profile gradient (change of decrease of the abundance of ammonia with decreasing pressure) (see Fig. 4.8, Fig. 4.9).

In sum, using an intermediate temperature-pressure profile between NEMESIS CIRS template and Moses et al. [49] model (up to 3 K difference bellow 0.1 bar and 5 K at about 0.1 bar) produces a higher flux, up to 13 % higher that the NEMESIS CIRS model, and therefore farther away from the data. This can be explained by the higher temperature that the intermediate profile has, in general, in comparison with the NEMESIS CIRS model. Hence, a profile with lower temperature compared with NEMESIS CIRS model should be explored in the future, to produce a radiance closer to data. As the pressure cutoff value for the ammonia profile decreases, the resulting flux decreases with respect to that of the NEMESIS CIRS model, up to about 25 % for a cutoff pressure of 0.5 bar, for $\lambda > 8.5$ μm, and gets closer to data. This can be explained by the increase in the abundance of ammonia when the cutoff value decreases, producing more absorption and therefore lower resulting flux. As the gradient of the ammonia profile decreases, the resulting flux increases in relation to the NEMESIS CIRS model, up to about 55 % (around 10 μm) for the case of the NH_3: +0.15 bar, getting farther away from the data. This can be explained by the decreases in the abundance of ammonia, for a given fixed pressure, when decreasing the ammonia gradient, meaning the absorption will decrease and therefore the resulting flux will be higher.

From this analysis, the conclusion is that to improve the fit of the simulation to the data several factors should be taken into account simultaneously : (1) Decrease of the temperature in the temperature-pressure profile, in relation to the NEMESIS CIRS model; (2) decrease the cutoff value for the ammonia profile; (3) maintain the gradient of the ammonia profile. These three factors I identified do not preclude the importance of others as yet unexplored.

Given the facts above, I can know discuss the results from the retrieval of methane, phosphine, ammonia and deuterated methane (see Fig. 3.24).

First, the fit of ammonia and phosphine absorption at 9-11 μm might be improved by adjusting the ammonia cutoff pressure and gradient, since changes in these factors alter the resulting flux at 9-12 μm (as indicated by Fig. 4.9, middle plot). Although the effect of variations of the phosphine profile on the resulting flux were not explored, they should be in future work.

Second, the fit of methane and deuterated methane at 8-9 μm produces a better fit than using the broader range of 7-9 μm. Ongoing work is exploring how the fit can be improved by adjusting the ammonia cutoff value and profile gradient, since the resulting flux in the 8-9 μm region is affected by variations of the former factors (see Fig.4.9, middle plot for cutoff effect; bottom plot for NH_3 gradient effect).

The value of the deuterium to hydrogen ratio obtained will be dependent of course on the quality of the fit at 8-9 μm. The uncertainty of the D/H ratio obtained is derived from the uncertainty of the fit. The final value obtained is consistent with the literature within a factor of 2: we get D/H (H_2) = (8.7-9.7) $\times 10^{-6}$ comparable with D/H (H_2) = (1.9-2.6) $\times 10^{-5}$ (Lellouch et al. [40]). To improve this estimation, I repeated the simulations and the retrieval at 8-9 μm changing the cutoff value of ammonia from 0.8 bar to 0.5 bar, for the reason explained above in this section. The new value estimated was D/H (H_2) = (1.8-2.4) $\times 10^{-5}$, with a $\chi^2(red) \sim 47$, which is in better agreement with the literature. However, the change in the ammonia profile performed that produced this better estimation is not fully supported as yet.
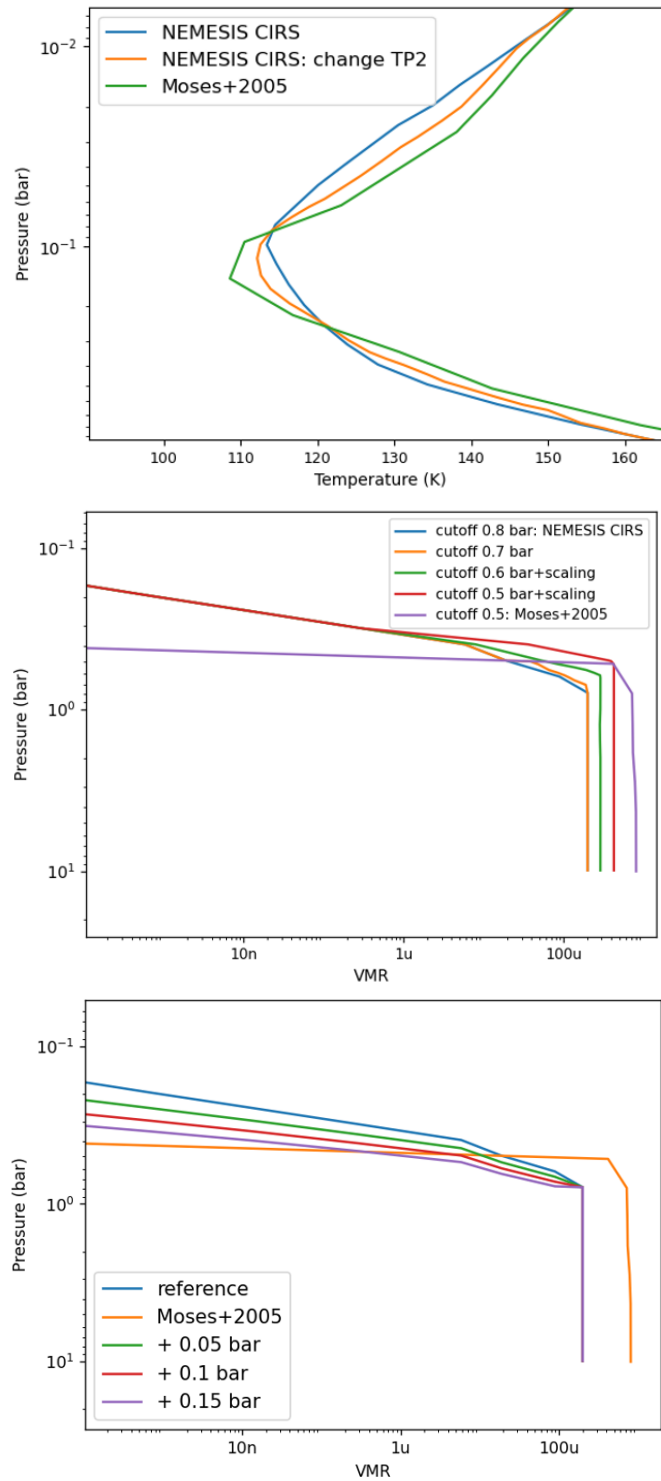
Figure 4.8: Variation of the temperature-pressure profile and ammonia profiles. **Top plot:** Three temperature-pressure profiles are plotted: the two initial models, NEMESIS CIRS (blue line) and Moses et al. [49] (green line), and a new intermediate mode (orange line). The goal of defining an intermediate temperature-pressure profile is to explore the effect on the resulting radiance. **Middle plot:** Plotted are two ammonia initial profiles, NEMESIS CIRS (blue line) and Moses et al. [49] (purple line), and several new ammonia profiles, similar to the NEMESIS CIRS, but with a decreasing ammonia cutoff value and increasing maximum value of abundance: 0.7 bar (orange), 0.6 bar (green) and 0.5 bar (red); **Bottom plot:** Different slopes for the ammonia profile are plotted. Starting from the NEMESIS CIRS model profile (blue), the value of pressure corresponding to a fixed value of abundance was increased by different constants, down to the cutoff value (around 100u): +0.05 bar (green), +0.1 bar (red) and +0.15 bar (purple).
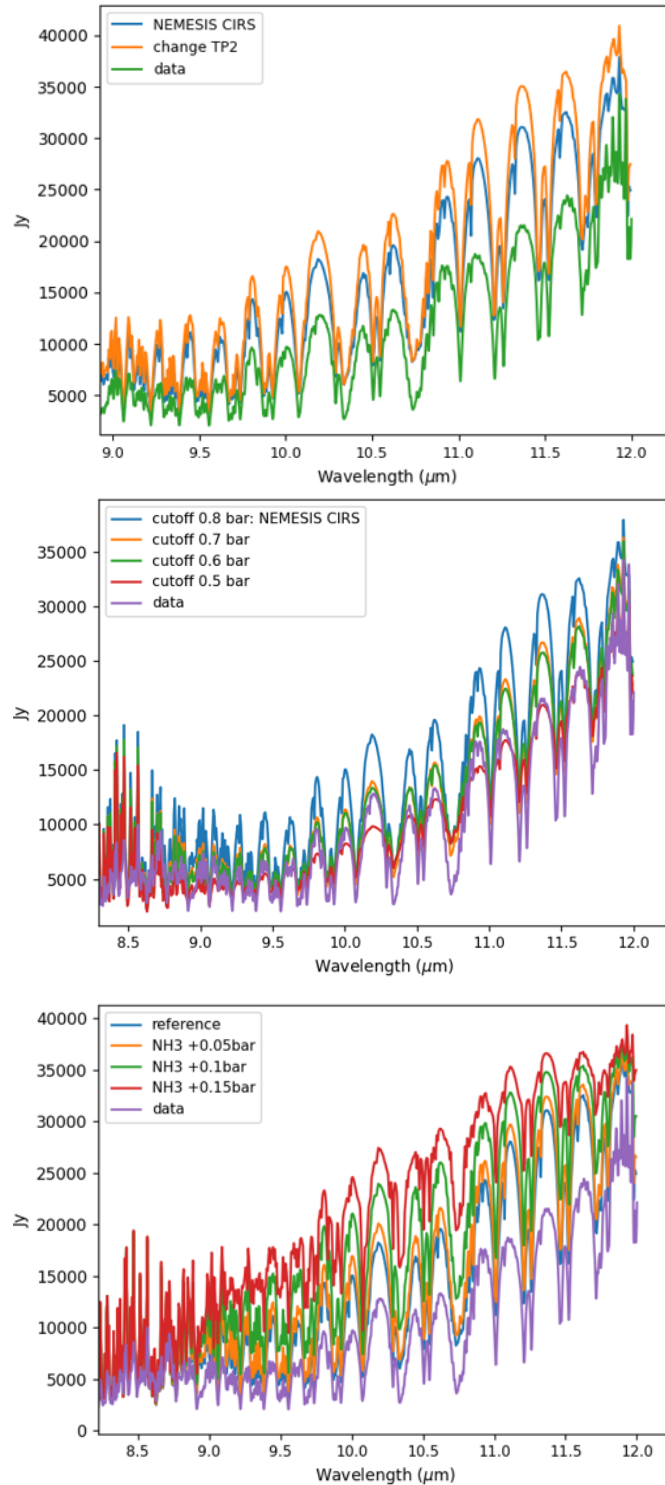
Figure 4.9: Sensitivity of the resulting flux to the temperature-pressure profiles and ammonia profiles. **Top plot:** Effect of intermediate temperature-pressure profile on the resulting flux. The temperature in this profile is higher than in the NEMESIS CIRS model, in general, resulting in a higher flux (orange) than the NEMESIS CIRS model (blue). Data: green **Middle:** Effect of different ammonia profile cutoffs on the resulting flux. Decreasing the cutoff pressure of ammonia acts to decrease the resulting flux: cutoff 0.8 bar (blue), cutoff 0.7 bar (orange), cutoff 0.6 bar (green), cutoff 0.5 bar (red), data (purple); **Bottom plot:** Effect of different ammonia profile gradients in the resulting flux. Decreasing the gradient has the effect of increasing the resulting flux. NEMESIS CIRS model (blue), $NH_3 + 0.05$ bar (orange), $NH_3 + 0.1$ bar (green), $NH_3 + 0.15$ bar (red), data=purple

Chapter 5

Conclusions

Sulphur dioxide was successfully detected around 7.4 μm and its abundance constrained. The mean abundance obtained using the VIRA-2 model (Zasova et al. [74]) was 120 ppb, comparing with 50-175 ppb (Encrenaz et al. [17]). Future comparisons with observations of TEXES of the 19 μm and the 8.7μm bands will be addressed. The next ESA mission to Venus, EnVision, aims to study the composition of the lower atmosphere in the night-side of Venus, to determine the origin and chemistry of this species in the lower atmosphere, around 0.86-1.18 μm. Therefore, simulations using PSG might be useful to prepare EnVision observations. Our group at IA is contributing to this groundbreaking mission.

Phosphine was not detected using TEXES observations around 10.5 μm (Encrenaz et al. [20]). The modelling of the telluric transmission at 955.2-955.3 cm^{-1} is an important obstacle to the search for phosphine. The non-detection of phosphine in this study does not mean there is not phosphine on Venus. However, it does mean that further dedicated observations should be performed to address this issue. The search for phosphine is extremmely difficult since there is an overlapping of telluric water lines and sulphur dioxide absorption lines with phosphine absorption lines, given possible low abundances of this molecule. Future work will include simulations in other phosphine absorptions bands, such as around 4-4.8 μm, 2.7-3.6 μm and 7.8-11 μm. Presently, our group at IA is analysing ground-based observations to search for phosphine on Venus in the IR.

The positive detection and negative detection of methane on Mars, respectively, by the Mars Express mission and the ExoMars mission were reproduced. One possible reason being addressed right now to explain this discrepancy is a possible variability with latitude, longitude, local hour, and altitude of the abundance of methane. The Mars Express positive detection reports to several hundred integrated spectra near Gale Crater, giving a column abundance of methane. The ExoMars observations report to a different altitude range, of about 5.8-8 km, through integration of several spectra for different latitudes. Therefore, both altitude and latitude variability might explain different results. Evidence for this explanation is still lacking and research is underway to address this issue. Searching for other methane absorption lines is a step that might provide some pieces to solve the puzzle, such as the detection of the methane absorption band centred around 7.6 μm.

Quantification of the detection limits of methane on Mars and phosphine on Venus, using the Planetary Spectrum Generator, is a future goal.

On Jupiter, the detection of the NH_3, PH_3 and CH_3D absorption and of the CH_4 emission was successful done. The estimation of the abundances of PH_3 and NH_3 was successful . However, further work is ongoing to better constrain the abundances of CH_4 and CH_3D and from there estimate the D/H ratio with more accuracy. A comparison of PSG results with preliminary results from our group at IA, through an independent analysis of the ISO data using the radiative transfer code NEMESIS is planned for the

future.

The determinations of the D/H ratio is extremely important to constrain the different atmospheric origins and evolutions of the terrestrial planets and giant planets. The ExoMars mission is measuring at present the D/H ratio on Mars to inform us about the processes that contributed and might still contribute to the atmospheric depletion on Mars. On Venus, future missions like the ESA'S EnVision might contribute to a better understanding of the atmospheric evolution of Venus, which seems to have lost most of its water to space.

On Mars, the determination of the D/H ratio is similar to the values of the literature. The value obtained was D/H $\sim$ 5.9 D/H (Earth), comparable with D/H = 3.4-4.8 D/H (Earth). (Encrenaz et al. [18]). On Venus and Jupiter, a first estimation of the D/H ratio was made which is in agreement with the literature. On Venus, the best estimated ratio was D/H $\sim$ 107 D/H(Earth), comparable with D/H= 80-160 D/H (Earth) (de Bergh et al. [7]). On Jupiter, the estimated ratio was D/H $(H_2) = (1.8\text{-}2.4) \times 10^{-5}$, comparable with D/H $(H_2) \sim (1.9 - 2.6) \times 10^{-5}$ (Lellouch et al. [40]).

To sum up, PSG proved to be an efficient tool when looking for minor chemical species in planetary atmospheres as well as compounds of astrobiological interest.

A crucial step before looking for compounds of potential biological origin, such as methane, phosphine and other minor chemical compounds, in the atmospheres of exoplanets, is to search and study them here in the Solar System. A future mission to study the atmospheres of exoplanets is the ARIEL (Atmospheric Remote-sensing Infrared Exoplanet Large-survey mission), from ESA, which will study the atmospheres of giant planets around M-dwarf stars. Our group at IA is contributing to this mission.

The next steps will be explored in a future PhD workplan regarding two main research lines: the study of water and methane on Mars, in the IR, using ExoMars data; the study of sulphur dioxide in the lower atmosphere of Venus in the context of the EnVision mission. I will also learn how to use the NEMESIS radiative transfer suite in order to check retrieval results with PSG.

Future observations will explore the use of SPIRou (SPectropolarimètre InfraROUge), at the Canada-Hawai-France Telescope (CHFT) , the Large Binocular Telescope Observatory, in Arizona, and the TEXES spectrograph, in order to observe Venus and Jupiter, in the IR, to constrain chemical composition. In particular, the study of the minor chemical species in Jupiter in the Solar System has synergies with the preparation of the ARIEL space-probe. The possibility to constrain the variability of methane on Mars using observations from the James Webb Space Telescope (JWST) will also be evaluated.

Bibliography

[1] Esa science technology - mars express science highlights: 6. estimation of the current rate of atmospheric escape. URL `https://sci.esa.int/web/mars-express/-/51826-6-estimation-of-the-current-rate-of-atmospheric-escape`.

[2] S. K. Atreya. *Atmospheres and ionospheres of the outer planets and their satellites*. Springer, 1986.

[3] T. Brooke, R. Knacke, T. Encrenaz, P. Drossart, D. Crisp, and H. Feuchtgruber. Models of the iso 3-μm reflection spectrum of jupiter. *Icarus*, 136(1):1–13, 1998. doi: 10.1006/icar.1998.6013.

[4] B. Bézard and C. D. Bergh. Composition of the atmosphere of venus below the clouds. *Journal of Geophysical Research*, 112(E4), 2007. doi: 10.1029/2006je002794.

[5] B. Bézard, C. de Bergh, D. Crisp, and J.-P. Maillard. The deep atmosphere of venus revealed by high-resolution nightside spectra. *Nature*, 345(6275):508–511, 1990. doi: 10.1038/345508a0.

[6] C. de Bergh. The d/h ratio and the evolution of water in the terrestrial planets. *Origins of life and evolution of the biosphere*, 23(1):11–21, 1993. doi: 10.1007/bf01581986.

[7] C. de Bergh, B. Bezard, T. Owen, D. Crisp, J.-P. Maillard, and B. L. Lutz. Deuterium on venus: Observations from earth. *Science*, 251(4993):547–549, 1991. doi: 10.1126/science.251.4993.547.

[8] C. de Bergh, B. Bézard, D. Crisp, J. Maillard, T. Owen, J. Pollack, and D. Grinspoon. Water in the deep atmosphere of venus from high-resolution spectra of the night side. *Advances in Space Research*, 15(4):79–88, 1995. doi: 10.1016/0273-1177(94)00067-b.

[9] T. Delahaye, R. Armante, N. Scott, N. Jacquinet-Husson, A. Chédin, L. Crépeau, C. Crevoisier, V. Douet, A. Perrin, A. Barbe, and et al. The 2020 edition of the geisa spectroscopic database. *Journal of Molecular Spectroscopy*, 380:111510, 2021. doi: 10.1016/j.jms.2021.111510.

[10] R. A. Dibiase, A. B. Limaye, J. S. Scheingross, W. W. Fischer, and M. P. Lamb. Deltaic deposits at aeolis dorsa: Sedimentary evidence for a standing body of water on the northern plains of mars. *Journal of Geophysical Research: Planets*, 118(6):1285–1302, 2013. doi: 10.1002/jgre.20100.

[11] T. M. Donahue and R. R. Hodges. Past and present water budget of venus. *Journal of Geophysical Research*, 97(E4):6083, 1992. doi: 10.1029/92je00343.

[12] T. M. Donahue and C. Russel. *The Venus atmosphere and ionosphere and their interaction with the solar wind: An overview, in Venus II–geology, geophysics, atmosphere, and solar wind environment*. edited by S. W. Baugher, D. M. Hunten, and R. J. Phillips, University of Arizona Press, 1997.

[13] F. E.A., W. Maier, and J. Mojzsis. The 'late veneer' on earth: Evidence from eoarchean ultramafic schists (metakomatiites). *Lunar Planet. Sci. Conf. 43rd, LPI Contribution No. 1659, id. 2890, Woodlands, Tex., 19–23 March*, 2012.

[14] D. Edwards. Genln2: A general line-by-line atmospheric transmittance and radiance model. version 3.0 description and users guide (no. ncar/tn-367+str). *University Corporation for Atmospheric Research*, 1992. doi: 10.5065/D6W37T86.

[15] T. Encrenaz. High-resolution imaging spectroscopy of planetary atmospheres. *Comptes Rendus Geoscience*, 347(3):145–152, 2015. doi: 10.1016/j.crte.2015.02.002.

[16] T. Encrenaz, P. Drossart, H. Feuchtgruber, E. Lellouch, B. Bézard, T. Fouchet, and S. Atreya. The atmospheric composition and structure of jupiter and saturn from iso observations: a preliminary review. *Planetary and Space Science*, 47(10-11):1225–1242, 1999. doi: 10.1016/s0032-0633(99)00046-x.

[17] T. Encrenaz, T. K. Greathouse, H. Roe, M. Richter, J. Lacy, B. Bézard, T. Fouchet, and T. Widemann. Hdo and so2 thermal mapping on venus: evidence for strong so2 variability. *Astronomy Astrophysics*, 543, 2012. doi: 10.1051/0004-6361/201219419.

[18] T. Encrenaz, C. Dewitt, M. J. Richter, T. K. Greathouse, T. Fouchet, F. Montmessin, F. Lefèvre, B. Bézard, S. K. Atreya, S. Aoki, and et al. New measurements of d/h on mars using exes aboard sofia. *Astronomy Astrophysics*, 612, 2018. doi: 10.1051/0004-6361/201732367.

[19] T. Encrenaz, T. K. Greathouse, E. Marcq, H. Sagawa, T. Widemann, B. Bézard, T. Fouchet, F. Lefèvre, S. Lebonnois, S. K. Atreya, and et al. Hdo and so2 thermal mapping on venus. *Astronomy Astrophysics*, 639, 2020. doi: 10.1051/0004-6361/202037741.

[20] T. Encrenaz, T. K. Greathouse, E. Marcq, T. Widemann, B. Bézard, T. Fouchet, R. Giles, H. Sagawa, J. Greaves, C. Sousa-Silva, and et al. A stringent upper limit of the ph3 abundance at the cloud top of venus. *Astronomy Astrophysics*, 643, 2020. doi: 10.1051/0004-6361/202039559.

[21] A. Fedorova, O. Korablev, A.-C. Vandaele, J.-L. Bertaux, D. Belyaev, A. Mahieux, E. Neefs, W. V. Wilquet, R. Drummond, F. Montmessin, and et al. Hdo and h2o vertical distributions and isotopic ratio in the venus mesosphere by solar occultation at infrared spectrometer on board venus express. *Journal of Geophysical Research*, 113, 2008. doi: 10.1029/2008je003146.

[22] F. Forget, F. Hourdin, R. Fournier, C. Hourdin, O. Talagrand, M. Collins, S. R. Lewis, P. L. Read, and J.-P. Huot. Improved general circulation models of the martian atmosphere from the surface to above 80 km. *Journal of Geophysical Research: Planets*, 104(E10):24155–24175, 1999. doi: 10.1029/1999je001025.

[23] T. Fouchet. Iso-sws observations of jupiter: Measurement of the ammonia tropospheric profile and of the 15n/14n isotopic ratio. *Icarus*, 143(2):223–243, 2000. doi: 10.1006/icar.1999.6255.

[24] I. Garate-Lopez and S. Lebonnois. Latitudinal variation of clouds' structure responsible for venus' cold collar. *Icarus*, 314:1–11, 2018. doi: 10.1016/j.icarus.2018.05.011.

[25] G. Gilli, S. Lebonnois, F. González-Galindo, M. López-Valverde, A. Stolzenbach, F. Lefèvre, J. Chaufray, and F. Lott. Thermal structure of the upper atmosphere of venus simulated by a ground-to-thermosphere gcm. *Icarus*, 281:55–72, 2017. doi: 10.1016/j.icarus.2016.09.016.

[26] M. Giuranna, S. Viscardy, F. Daerden, L. Neary, G. Etiope, D. Oehler, V. Formisano, A. Aron-ica, P. Wolkenberg, S. Aoki, and et al. Independent confirmation of a methane spike on mars and a source region east of gale crater. *Nature Geoscience*, 12(5):326–332, 2019. doi: 10.1038/s41561-019-0331-9.

[27] L. Glaze, J. B. Garvin, B. Robertson, N. M. Johnson, M. J. Amato, J. Thompson, C. Goodloe, and D. Everett. Davinci: Deep atmosphere venus investigation of noble gases, chemistry, and imaging. *Abstract for Lunar Planet. Sci. Conf. 47th*, 2016.

[28] I. Gordon, L. Rothman, C. Hill, R. Kochanov, Y. Tan, P. Bernath, M. Birk, V. Boudon, A. Campar-gue, K. Chance, and et al. The hitran2016 molecular spectroscopic database. *Journal of Quantitative Spectroscopy and Radiative Transfer*, Jul 2017.

[29] J. S. Greaves, A. M. S. Richards, W. Bains, P. B. Rimmer, H. Sagawa, D. L. Clements, S. Seager, J. J. Petkowski, C. Sousa-Silva, S. Ranjan, and et al. Phosphine gas in the cloud decks of venus. *Nature Astronomy*, 2020. doi: 10.1038/s41550-020-1174-4.

[30] K. Hamano, Y. Abe, and H. Genda. Emergence of two types of terrestrial planet on solidification of magma ocean. *Nature*, 497(7451):607–610, 2013. doi: 10.1038/nature12163.

[31] P. Irwin. The origin of belt/zone contrasts in the atmosphere of jupiter and their correlation with 5-µm opacity. *Icarus*, 149(2):397–415, 2001. doi: 10.1006/icar.2000.6542.

[32] P. Irwin. *Giant planets of our solar system: atmospheres, composition, and structure*. Springer, 2010.

[33] B. M. Jakosky, R. O. Pepin, R. E. Johnson, and J. Fox. Mars atmospheric loss and isotopic fraction-ation by solar-wind-induced sputtering and photochemical escape. *Icarus*, 111(2):271–288, 1994. doi: 10.1006/icar.1994.1145.

[34] J. F. Kasting. Runaway and moist greenhouse atmospheres and the evolution of earth and venus. *Icarus*, 74(3):472–494, 1988. doi: 10.1016/0019-1035(88)90116-9.

[35] O. Korablev, A. C. Vandaele, F. Montmessin, A. A. Fedorova, A. Trokhimovskiy, F. Forget, F. Lefèvre, F. Daerden, I. R. Thomas, L. Trompet, and et al. No detection of methane on mars from early exomars trace gas orbiter observations. *Nature*, 568(7753):517–520, 2019. doi: 10.1038/s41586-019-1096-4.

[36] V. A. Krasnopolsky. High-resolution spectroscopy of venus: Detection of ocs, upper limit to h2s, and latitudinal variations of co and hf in the upper cloud layer. *Icarus*, 197(2):377–385, 2008. doi: 10.1016/j.icarus.2008.05.020.

[37] V. A. Krasnopolsky. Spatially-resolved high-resolution spectroscopy of venus 2. variations of hdo, ocs, and so2 at the cloud tops. *Icarus*, 209(2):314–322, 2010. doi: 10.1016/j.icarus.2010.05.008.

[38] V. A. Krasnopolsky. Variations of the hdo/h2o ratio in the martian atmosphere and loss of water from mars. *Icarus*, 257:377–386, 2015. doi: 10.1016/j.icarus.2015.05.021.

[39] V. A. Krasnopolsky, J. P. Maillard, and T. C. Owen. Detection of methane in the martian atmosphere: evidence for life? *Icarus*, 172(2):537–547, 2004. doi: 10.1016/j.icarus.2004.07.004.

[40] E. Lellouch, B. Bézard, T. Fouchet, H. Feuchtgruber, T. Encrenaz, and T. D. Graauw. The deuterium abundance in jupiter and saturn from iso-sws observations. *Astronomy Astrophysics*, 370(2):610–622, 2001. doi: 10.1051/0004-6361:20010259.

[41] J. S. Lewis. *Physics and chemistry of the solar system*. Elsevier, 2004.

[42] P. M. Machado. *Dynamics of Venus's Atmosphere*. SCHOLARS PRESS, 2014.

[43] E. Marcq, B. Bezard, T. Encrenaz, and M. Birlan. Latitudinal variations of co and ocs in the lower atmosphere of venus from near-infrared nightside spectro-imaging. *Icarus*, 179(2):375–386, 2005. doi: 10.1016/j.icarus.2005.06.018.

[44] E. Marcq, T. Encrenaz, B. Bézard, and M. Birlan. Remote sensing of venus' lower atmosphere from ground-based ir spectroscopy: Latitudinal and vertical distribution of minor species. *Planetary and Space Science*, 54(13-14):1360–1370, 2006. doi: 10.1016/j.pss.2006.04.024.

[45] E. Marcq, D. Belyaev, F. Montmessin, A. Fedorova, J.-L. Bertaux, A. C. Vandaele, and E. Neefs. An investigation of the so2 content of the venusian mesosphere using spicav-uv in nadir mode. *Icarus*, 211(1):58–69, 2011. doi: 10.1016/j.icarus.2010.08.021.

[46] E. Millour, F. Forget, M. V. A. Spiga, V. Zakharov, L. Montabone, F. Lefèvre, F. Montmessin, J.-Y. Chaufray, M. A. López-Valverde, F. González-Galindo, S. R.Lewis, P. L. Read, M.-C. Desjean, F. Cipriani, and the MCD development team. The mars climate database (version 5.3). *Scientific Workshop: "From Mars Express to ExoMars"*, ESAC Madrid, Spain, fev 2018.

[47] F. Montmessin, J.-L. Bertaux, F. Lefèvre, E. Marcq, D. Belyaev, J.-C. Gérard, O. Korablev, A. Fedorova, V. Sarago, A. Vandaele, and et al. A layer of ozone detected in the nightside upper atmosphere of venus. *Icarus*, 216(1):82–85, 2011. doi: 10.1016/j.icarus.2011.08.010.

[48] F. Montmessin, O. Korablev, F. Lefèvre, J.-L. Bertaux, A. Fedorova, A. Trokhimovskiy, J. Chaufray, G. Lacombe, A. Reberac, L. Maltagliati, and et al. Spicam on mars express: A 10 year in-depth survey of the martian atmosphere. *Icarus*, 297:195–216, 2017. doi: 10.1016/j.icarus.2017.06.022.

[49] J. I. Moses, T. Fouchet, B. Bézard, G. R. Gladstone, E. Lellouch, and H. Feuchtgruber. Photochemistry and diffusion in jupiters stratosphere: Constraints from iso observations and comparisons with other giant planets. *Journal of Geophysical Research: Planets*, 110(E8), 2005. doi: 10.1029/2005je002411.

[50] M. J. Mumma, G. L. Villanueva, R. E. Novak, T. Hewagama, B. P. Bonev, M. A. Disanti, A. M. Mandell, and M. D. Smith. Strong release of methane on mars in northern summer 2003. *Science*, 323(5917):1041–1045, 2009. doi: 10.1126/science.1165243.

[51] R. Orosei, S. E. Lauro, E. Pettinelli, A. Cicchetti, M. Coradini, B. Cosciotti, F. D. Paolo, E. Flamini, E. Mattei, M. Pajola, and et al. Radar evidence of subglacial liquid water on mars. *Science*, 2018. doi: 10.1126/science.aar7268.

[52] T. Owen, J. P. Maillard, C. D. Bergh, and B. L. Lutz. Deuterium on mars: The abundance of hdo and the value of d/h. *Science*, 240(4860):1767–1767, 1988. doi: 10.1126/science.240.4860.1767.

[53] T. Owen, P. Mahaffy, H. B. Niemann, S. Atreya, T. Donahue, A. Bar-Nun, and I. D. Pater. A low-temperature origin for the planetesimals that formed jupiter. *Nature*, 402(6759):269–270, 1999. doi: 10.1038/46232.

[54] J. J. Plaut, G. Picardi, A. Safaeinili, A. B. Ivanov, S. M. Milkovich, A. Cicchetti, W. Kofman, M. Jérémie, W. M. Farrell, R. J. Phillips, and et al. Subsurface radar sounding of the south polar layered deposits of mars. *Science*, 316(5821):92–95, 2007. doi: 10.1126/science.1139672.

[55] J. B. Pollack, J. Dalton, D. Grinspoon, R. B. Wattson, R. Freedman, D. Crisp, D. A. Allen, B. Bezard, C. Debergh, L. P. Giver, and et al. Near-infrared light from venus nightside: A spectroscopic analysis. *Icarus*, 103(1):1–42, 1993. doi: 10.1006/icar.1993.1055.

[56] F. Poulet, J.-P. Bibring, J. F. Mustard, A. Gendrin, N. Mangold, Y. Langevin, R. E. Arvidson, B. Gondet, and C. Gomez. Phyllosilicates on mars and implications for early martian climate. *Nature*, 438(7068):623–627, 2005. doi: 10.1038/nature04274.

[57] R. Ramstad, S. Barabash, Y. Futaana, H. Nilsson, and M. Holmström. Ion escape from mars through time: An extrapolation of atmospheric loss based on 10 years of mars express measurements. *Journal of Geophysical Research: Planets*, 123(11):3051–3060, 2018. doi: 10.1029/2018je005727.

[58] A. Sanchez-Lavega. *An introduction to planetary atmospheres*. Taylor Francis, 2011.

[59] E. W. Schwieterman, N. Y. Kiang, M. N. Parenteau, C. E. Harman, S. Dassarma, T. M. Fisher, G. N. Arney, H. E. Hartnett, C. T. Reinhard, S. L. Olson, and et al. Exoplanet biosignatures: A review of remotely detectable signs of life. *Astrobiology*, 18(6):663–708, 2018. doi: 10.1089/ast.2017.1729.

[60] S. Seager, J. J. Petkowski, P. Gao, W. Bains, N. C. Bryan, S. Ranjan, and J. Greaves. The venusian lower atmosphere haze as a depot for desiccated microbial life: A proposed life cycle for persistence of the venusian aerial biosphere. *Astrobiology*, 21(10):1206–1223, 2021. doi: 10.1089/ast.2020. 2244.

[61] C. Sousa-Silva, S. Seager, S. Ranjan, J. J. Petkowski, Z. Zhan, R. Hu, and W. Bains. Phosphine as a biosignature gas in exoplanet atmospheres. *Astrobiology*, 20(2):235–268, 2020. doi: 10.1089/ast. 2018.1954.

[62] F. M. Stuart, D. F. Mark, P. Gandanger, and P. Mcconville. Earth-atmosphere evolution based on new determination of devonian atmosphere ar isotopic composition. *Earth and Planetary Science Letters*, 446:21–26, 2016. doi: 10.1016/j.epsl.2016.04.012.

[63] F. W. Taylor, H. Svedhem, and J. W. Head. Venus: The atmosphere, climate, surface, interior and near-space environment of an earth-like planet. *Space Science Reviews*, 214(1), 2018. doi: 10.1007/s11214-018-0467-8.

[64] J. Tennyson, S. N. Yurchenko, A. F. Al-Refaie, V. H. Clark, K. L. Chubb, E. K. Conway, A. Dewan, M. N. Gorman, C. Hill, A. Lynas-Gray, and et al. The 2020 release of the exomol database: Molecular line lists for exoplanet and other hot atmospheres. *Journal of Quantitative Spectroscopy and Radiative Transfer*, 255:107228, 2020. doi: 10.1016/j.jqsrt.2020.107228.

[65] E. Thérèse and S. Dunlop. *The solar system*. Springer, 2010.

[66] D. V. Titov, H. Svedhem, F. W. Taylor, S. Barabash, J. L. Bertaux, P. Drossart, V. Formisano, B. Häusler, O. Korablev, W. J. Markiewicz, and et al. Venus express: Highlights of the nominal mission. *Solar System Research*, 43(3):185–209, 2009. doi: 10.1134/s0038094609030010.

[67] J. L. Vago, F. Westall, A. J. Coates, R. Jaumann, O. Korablev, V. Ciarletti, I. Mitrofanov, J. L. Josset, M. C. De Sanctis, J. P. Bibring, F. Rull, F. Goesmann, H. Steininger, W. Goetz, W. Brinckerhoff, C. Szopa, F. Raulin, H. Edwards, L. G. Whyte, …, and C. Carreau. Habitability on early mars and the search for biosignatures with the exomars rover. *Astrobiology*, (17(6-7)):471–510, 2017.

[68] A. Vandaele, O. Korablev, D. Belyaev, S. Chamberlain, D. Evdokimova, T. Encrenaz, L. Esposito, K. Jessup, F. Lefèvre, S. Limaye, and et al. Sulfur dioxide in the venus atmosphere: I. vertical distribution and variability. *Icarus*, 295:16–33, 2017. doi: 10.1016/j.icarus.2017.05.003.

[69] G. Villanueva, M. Smith, S. Protopapa, S. Faggi, and A. Mandell. Planetary spectrum generator: An accurate online radiative transfer suite for atmospheres, comets, small bodies and exoplanets. *Journal of Quantitative Spectroscopy and Radiative Transfer*, 217:86–104, 2018. doi: 10.1016/j. jqsrt.2018.05.023.

[70] G. L. Villanueva, G. Liuzzi, M. M. J. Crismani, S. Aoki, A. C. Vandaele, F. Daerden, M. D. Smith, M. J. Mumma, E. W. Knutsen, L. Neary, and et al. Water heavily fractionated as it ascends on mars as revealed by exomars/nomad. *Science Advances*, 7(7), 2021. doi: 10.1126/sciadv.abc8843.

[71] C. R. Webster, P. R. Mahaffy, G. J. Flesch, P. B. Niles, J. H. Jones, L. A. Leshin, S. K. Atreya, J. C. Stern, L. E. Christensen, T. Owen, and et al. Isotope ratios of h, c, and o in co 2 and h 2 o of the martian atmosphere. *Science*, 341(6143):260–263, 2013. doi: 10.1126/science.1237961.

[72] C. R. Webster, P. R. Mahaffy, S. K. Atreya, J. E. Moores, G. J. Flesch, C. Malespin, C. P. Mckay, G. Martinez, C. L. Smith, J. Martin-Torres, and et al. Background levels of methane in mars' atmosphere show strong seasonal variations. *Science*, 360(6393):1093–1096, 2018. doi: 10.1126/ science.aaq0131.

[73] L. Zasova, V. Moroz, L. Esposito, and C. Na. So2 in the middle atmosphere of venus: Ir measurements from venera-15 and comparison to uv data. *Icarus*, 105(1):92–109, 1993. doi: 10.1006/icar.1993.1113.

[74] L. V. Zasova, V. I. Moroz, V. M. Linkin, I. V. Khatuntsev, and B. S. Maiorov. Structure of the venusian atmosphere from surface up to 100 km. *Cosmic Research*, 44(4):364–383, 2006. doi: 10.1134/s0010952506040095.

[75] X. Zhang, M.-C. Liang, F. Montmessin, J.-L. Bertaux, C. Parkinson, and Y. L. Yung. Photolysis of sulphuric acid as the source of sulphur oxides in the mesosphere of venus. *Nature Geoscience*, 3 (12):834–837, 2010. doi: 10.1038/ngeo989.

[76] X. Zhang, M. C. Liang, F. P. Mills, D. A. Belyaev, and Y. L. Yung. Sulfur chemistry in the middle atmosphere of venus. *Icarus*, 217(2):714–739, 2012. doi: 10.1016/j.icarus.2011.06.016.

Chapter 6

Appendix

6.1   Venus

Molecule	Bands
SO_2	7.1-7.6 μm, 8.3-9.0 μm
CO_2	7.7-8.3 μm, 7.1-7.6 μm
H_2O	no strong bands identified

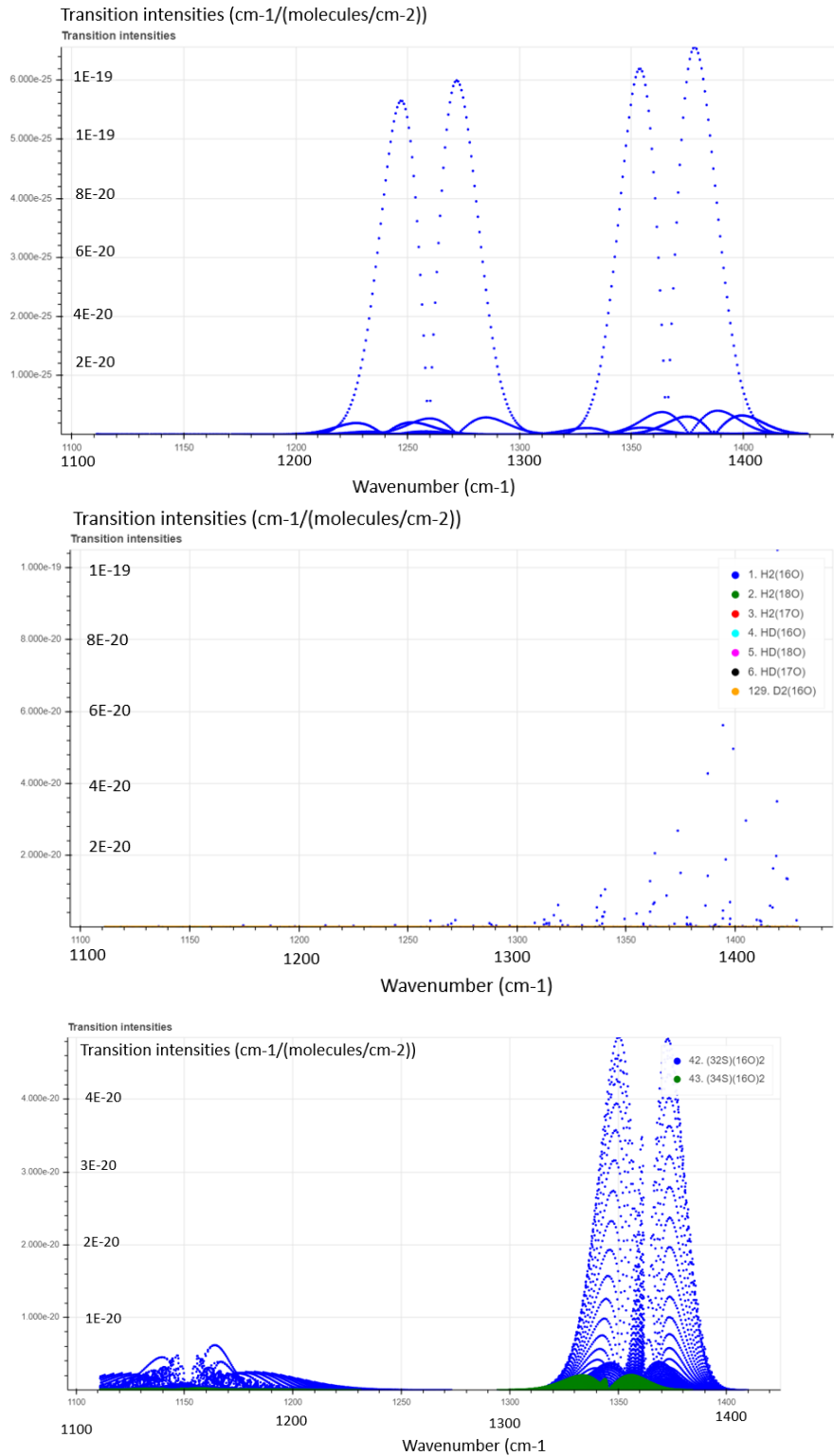**Table 6.1:** Main molecular bands identified in HITRAN for Case Study 1

Figure 6.1: HITRAN Plot of the intensities of the transitions of CO_2, H_2O and SO_2, between 7 μm (1429 cm^{-1}) and 9 μm (1111 cm^{-1}). For more information on HITRAN, see Gordon et al. [28]
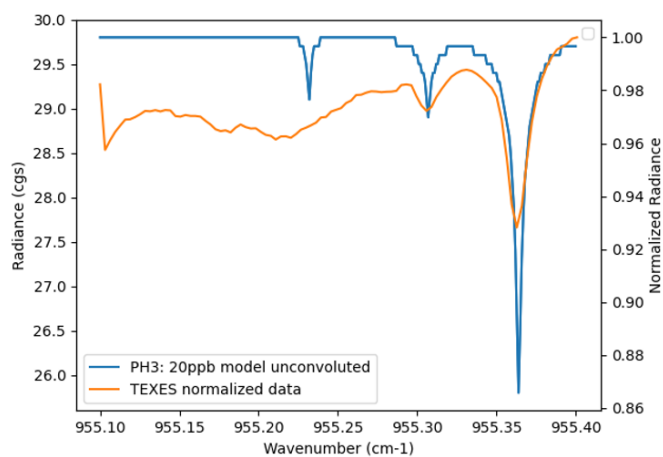
Figure 6.2: Calibration of phosphine observations. To calibrate the TEXES observations a referenced calibrated spectrum was used (blue line), in units of radiance and normalized radiance. A correspondence between normalized units and absolute units was done. The calibrated data points were selected using a dedicated software like Origin/Grapher and later an interpolation was done such that I could plot the calibrated data points. The absolute units obtained for the TEXES data are in agreement with a prediction by the calculation of the Planck function at approximately the temperature, pressure and wavenumber interval of the observations